

**Dual-Passive Mode Locking of
High Average Power, Solid-State Lasers**

BY
STEPHANIE SCHIEFFER
B.A., Johnston Center at the University of Redlands, Redlands, California
1994
B.S., University of Illinois at Chicago, Chicago, IL, 2004
M.S., University of Illinois at Chicago, Chicago, IL 2008

THESIS

Submitted as partial fulfillments of the requirements
for the degree of Doctor of Philosophy in Physics
in the Graduate College of the
University of Illinois at Chicago, 2011

Chicago, Illinois

Defense Committee:
W. Andreas Schroeder, Chair and Advisor
Juan Carlos Campuzano
Charles K. Rhodes
Sivalingam Sivananthan
Robert Gordon, Chemistry

ACKNOWLEDGEMENTS

Many people have provided me with assistance and support throughout my graduate career. First, I would like to thank my family for their unconditional love and support. I would like to thank my advisor, Professor Andreas Schroeder for his patient instruction. Professors John Marko and Serdar Ogut are two of the many outstanding professors I would like to thank who took extra time to assist in my academic development. I would like to thank my fellow students Kimberly Frey and Jeremy Callner for being my study partners through out much of my coursework and the qualifying exams. I would like to thank Nathan Rimington, Adrian Cornea, Michael Greco, Joel Berger, Ben Rickman, John Hogan, and Tuo Li as well as Professors James Longworth and Ved Nayyar for their invaluable help with this project. I would like to thank the people in the machine shop managed by Kevin Lynch for sharing their expertise with me. I would like to thank the physics department office staff for their unending support. Finally, I would like to thank my committee members, Professor Jun Carlos Campuzano, Professor Charles K. Rhodes, Professor Sivalingam Sivananthan, and Professor Robert K. Gordon, for their time, expertise and guidance at this exciting time in my career.

TABLE OF CONTENTS

<u>CHAPTER</u>		<u>PAGE</u>
1	INTRODUCTION.....	1
2	BACKGROUND INFORMATION	8
	2.1 Introduction.....	8
	2.2 Basic Laser Theory.....	9
	2.2.1 The Two-Level System.....	10
	2.2.2 The Four-Level System.....	14
	2.3 Nd ³⁺ Ion, Heat Management, and Crystal Geometry.....	17
	2.4 Gain Saturation.....	20
	2.5 Nonlinear Optical Effects.....	25
3	THERMAL-LENS-SHAPED Nd:GdVO ₄ LASER OSCILLATOR....	24
	3.1 Introduction.....	24
	3.2 Thermal Lens Shaping Theory.....	25
	3.3 Shaping of the Thermal Lens.....	33
	3.4 Laser Oscillator Characterization.....	36
	3.5 Modifications for Mode Locking.....	41
4	MODE LOCKING BASICS.....	45
	4.1 Introduction.....	45
	4.2 Qualitative Frequency Description Of Continuous Wave Mode Locking.....	47
	4.3 Active Mode Locking Analysis.....	50
	4.3.1 Time And Frequency Domain.....	51
	4.3.2 Mode Coupling Analysis.....	56
	4.4 Mode Locking With A Saturable Bragg Reflector.....	59
	4.4.1 Saturable Bragg Reflector Design.....	60
	4.4.2 Saturable Bragg Reflector Mode Locking.....	62
	4.5 Mode Locking With A Nonlinear Mirror.....	68

TABLE OF CONTENTES (continued)

5	NOVEL DUAL-PASSIVE MODE LOCKING.....	73
5.1	Introduction.....	73
5.2	Dual-Passive Mode Locking.....	75
5.3	Reduction Of Mode Locking Threshold.....	78
5.4	Pulse Shortening.....	83
5.5	Phase Mismatch.....	88
6	LASER INDUCED THERMAL EFFECTS IN SATURABLE BRAGG REFLECTORS.....	95
6.1	Introduction.....	95
6.2	The Three-Dimensional Heat Equation And Boundary Equations.....	96
6.3	Heat Per Unit Volume.....	100
6.4	Temperature.....	101
6.5	Thermal Deformation.....	107
6.6	Lensing And Aberrations.....	110
7	HIGH-RESOLUTION, LOW-ABERRATION SPECTROGRAPH.....	118
7.1	Introduction.....	118
7.2	Aberrations.....	120
7.3	Spectrograph Design.....	125
7.4	Alignment And Performance.....	132
7.5	Picosecond Laser Spectrum.....	141
8	SUMMARY.....	145
	APPENDIX.....	150
A.1	Finite Cosine Transformation of the z -Coordinate.....	150
A.2	Finite Cosine Transformation of $\frac{\partial^2 T}{\partial r^2} + \frac{1}{r} \frac{\partial T}{\partial r} + \frac{\partial^2 T}{\partial z^2}$	151
A.3	Finite Cosine Transformation of $\frac{\alpha}{\kappa_{th}} Q(r) \exp(-\alpha z)$	153

TABLE OF CONTENTES (continued)

A.4	Finite Hankel Transformation of the r -Coordinate.....	153
A.5	Finite Cosine Transformation of $\frac{1}{r} \frac{\partial}{\partial r} \left(r \frac{\partial}{\partial r} T(r, u) \right) - u^2 T(r, u)$	154
A.6	Hankel Transformation of $\beta_g \exp\left(-\frac{\gamma g r^2}{w^2}\right)$	155
B.1	Permission to Use Figures.....	159
CITED LITERATURE.....		161

LIST OF FIGURES

<u>FIGURE</u>	<u>PAGE</u>
1. Two-level energy diagram.....	10
2. Four-level energy diagram.....	15
3. Neodymium energy diagram.....	18
4. Brewster-cut gain medium.....	25
5. Temperature profile in gain medium.....	26
6. Nd:GdVO ₄ laser crystal.....	28
7. Thermal lens in gain media.....	29
8. Pumping scheme.....	34
9. Pump radiation ray tracing.....	35
10. Output power vs. pump power for different cavity lengths.....	37
11. Spot size and M ² vs diode current.....	40
12. Thermal focal length vs diode current.....	41
13. Stability curves.....	42
14. Output power vs diode current for extended cavity.....	44

15.	Axial modes inside laser cavity.....	46
16.	Saturable Bragg reflector.....	61
17.	Nonlinear mirror.....	71
18.	Extended oscillator cavity.....	76
19.	Pulse duration vs. output power.....	79
20.	Four autocorrelations.....	85
21.	Single pass phase locking.....	87
22.	Second harmonic generation vs. phase matching.....	90
23.	Idealized cylindrical saturable Bragg reflector.....	99
24.	Temperature distributions in saturable Bragg reflector.....	105
25.	Bowing vs. saturable Bragg reflector.....	108
26.	Radius of curvature and spherical aberrations vs. spot size.....	112
27.	Radius of curvature vs. F/F_{sat}	113
28.	Radius of curvature and spherical aberrations vs. thickness.....	116
29.	Autocorrelation schematic.....	119
30.	Aberrations.....	121
31.	Spectrometer designs.....	124

32.	Off-axis spectrometer schematic.....	126
33.	Piston error.....	128
34.	Mercury doublet image.....	134
35.	Smile error.....	136
36.	Image width vs. aperture width.....	137
37.	Argon spectrum.....	140
38.	Spectrum for Nd:GdVO ₄ and Nd:YAG.....	142
39.	Spectral output after self phase modulation.....	143

LIST OF ABBREVIATIONS

AM	Amplitude modulation
BBO	Beta barium borate
BiBO	Bismuth borate
CW	Continuous wave
DOC	Dichroic output coupler
DPSS	Diode pumped solid-state
FM	Frequency modulation
FROG	Frequency resolved optical gating
FWHM	Full-width half-max
GDD	Group Delay Dispersion
GdVO ₄	Gadolinium vanadate
GRIN	Gradient index
HWHM	Half-width half-max
LBO	Lithium triborate
LD	Laser diode
ML	Mode locked
NLM	Nonlinear mirror
OC	Output coupler
OPA	Optical parametric amplifier
OPO	Optical parametric oscillator
QML	Q-switched mode locked
QW	Quantum well
RTM	Ray transfer matrices
SBR	Saturable Bragg reflector

SESAM	Semiconductor saturable absorbing mirror
SHG	Second harmonic generator
SPM	Self-phase modulation
TEM	Transverse electro-magnetic
TLS	Thermal lens shaping
TPA	Two photon absorption
YAG	Yttrium aluminum garnet
YVO ₄	Yttrium orthovanadate

1. INTRODUCTION

Laser oscillators with average output powers on the order of multiple watts and pulse durations less than 100 picoseconds have many uses in research and industry. For instance, precise machining of metals takes advantage of the reduced thermal effects from laser pulses between 100 picoseconds and 10fs [1]. Biologists and chemists use lasers in time-resolved spectroscopy of biochemical reactions [2-4]. Ultrafast lasers are also used in chemistry, physics and material science to probe the electronic and vibrational states of various materials including semiconductors [5,6].

Such spectroscopic applications often require a specific photon color which may not be possible to generate directly from a solid-state oscillator. It may, however, be generated through nonlinear effects in optical parametric oscillators (OPO) and optical parametric amplifiers (OPA). These techniques typically require watt-level pump lasers which, in most instances, means that the output pulse from the low average power oscillator must be amplified before it can be used to pump the OPO/OPA [7-10]. However, if the oscillator generates pulses with enough average power, an OPO/OPA can be pumped directly. In some cases, the resulting pulse can be even shorter than that of the pump[11-15]; for example, Kurti, et.al. have generated 500 fs using a Nd:YAG laser producing 250mJ, 10 ps pulses[15].

The development of a high average power ultrafast laser requires addressing several major issues. First the laser oscillator must be designed. This requires designing and building a laser head and pumping scheme with the proper gain to loss ratio. Most of the optical elements in the oscillator cavity contribute to the overall losses while the gain is generated entirely in the laser crystal by ‘pumping’ the gain medium. Some portion of this pump energy results in the heating of the laser crystal. Even though the exact effects depend upon the details of the pump, cooling, and laser crystal geometry, the thermal effects must be managed to prevent, among other things, damaging the laser crystal. Chapter 2 presents an overview of basic laser physics, thermal management, and nonlinear optics.

Chapter 3 goes on to describe the thermal lens shaping (TLS) concept developed in our group and employed in the laser oscillator presented in this thesis. The basic idea of TLS is to actively shape and collimate the pump radiation from unlensed diode bars using cylindrical and spherical lenses such that the resulting thermal lens in the gain media, experienced by the laser resonator, is stigmatic. In this chapter, the thermal lens generated in the laser crystal is modeled using transfer matrices (RTM) representing two separate contributions: the bulk thermo-optic effect, the change in refractive index with temperature $\left(\frac{dn}{dT}\right)$, and the thermal expansion of the laser crystal.

Comparison of the thermal lens in the sagittal and tangential planes allows for the determination of the optimal pump beam ellipticity such that the laser

oscillator sees an astigmatism free thermal lens. In general, achieving high average output powers using this scheme requires a large mode area in the gain medium. The implementation of this design for a Nd:GdVO₄ laser crystal is detailed, and the characterization of the laser oscillator shows that it indeed has a high average power of 9.5W and a high quality ($M^2 < 1.2$) TEM₀₀ spatial mode.

Once the basic laser oscillator design has been developed, short pulses need to be generated. This is accomplished by establishing a well-defined phase relationship between the longitudinal oscillating modes in the cavity and is called mode locking. When this is achieved, a single pulse oscillates in the cavity. The basic theoretical groundwork of mode locking is presented in Chapter 4 as are several of the more frequently used methods for achieving a single, ultrasort pulse in the cavity. A good way to understand mode locking is by considering an optical element that has an intensity dependent loss. The feedback nature of a laser ensures the fields that experience more loss die out while the others are able to take more gain. When the gain dynamics in the laser crystal and the modulation of the signal are properly balanced, a single short pulse results.

In the past, lasers have been mode locked using a dye cell directly in front of a mirror [50]. More recently, semiconductor saturable absorbing mirrors (SESAMs) also known as saturable Bragg reflectors (SBRs) have become one of the most common laser resonator mode locking elements --

particularly for modern diode-pumped solid-state lasers operating near $1\mu\text{m}$ [18, 26-42]. For example, a 20W, 21ps Nd:YVO₄ laser [27], a 60W, 810 fs Yb:YAG laser [26], a 23.5W of 21.5 ps Nd:YVO₄ laser[28], a 3.5W, 250fs Yb:KGW laser [31] and a 6 W, 9.2 ps Nd:GdVO₄ laser [30] have all been mode locked with the aide of an SBR. The versatility of the SBR stems from the ability to tailor its optical response [43 -47] to the application. For instance, the central wavelength of the intensity dependent (i.e., saturable) reflectivity is determined by the characteristics of the quantum well(s) (QWs) grown into the SBR. Another important parameter, the saturable change in reflectivity, ΔR_{sat} , can be manipulated by QW engineering and the SBR structure. Finally, the quality of the crystal growth [19] as well as proton bombardment during the manufacturing [48, 49] allows a large amount of control over the recovery time of the SBR.

Generally speaking, mode locking a thermal lens shaped laser oscillator using a preferred ultrafast optical tool, the SBR [26-30], is challenging because the critical pulse energy threshold for obtaining CW mode locking with no Q-switching is high for laser systems with large mode areas in their gain medium [26]. Operating the oscillator above this threshold is important because Q-switching instabilities generate large pulse energies that can easily damage the SBR [17]. In order to avoid this undesired result, the novel dual-passive mode locking approach [18] presented in Chapter 5 was devised to lower the CW mode locking threshold for the Nd:GdVO₄ TLS laser oscillator presented in

Chapter 3 by more than a factor of two (from $0.8\mu\text{J}$ to $0.33\mu\text{J}$). This technique employs an SBR as an amplitude modulator and a phase mis-matched second harmonic crystal (SHG) to generate phase-locking. Furthermore, chapter 5 will show under the proper conditions, the SHG also does pulse shortening; i.e., shorter pulses can be obtained using this dual-passive (7.8 ps at 6W output power) method than with an SBR alone (15ps pulses at 8W output power).

Two characteristics of an SBR [19], which are detailed in Chapter 4, are saturable and nonsaturable absorption which are generally on the order of a few percent and which cause a thermal gradient in the SBR. This, of course, results in thermally-induced stress and strain, and consequently the SBR bows. Since the shape of the end mirror in a laser cavity must be well-matched to the wavefront to retain a high-quality spatial mode, the position of the SBR must be adjusted to match its thermally-induced radius of curvature to the oscillating mode. Chapter 6 investigates this bowing as a function of an SBR and laser parameters. The temperature profile that results from the saturable and nonsaturable absorption of the incident laser beam is analytically evaluated from the three-dimensional heat equation. This temperature distribution is then used to determine the resulting deformation in an SBR for a variety of incident laser spot sizes and SBR thickness. The results are shown to be consistent with experiment.

Many ultrafast applications, including OPO/OPAs, require a detailed characterization of the laser pulse. Frequency resolved optical gating (FROG)

measurements provide both amplitude and phase information and are thus very useful in the characterization of laser pulses [20-23]. FROGs obtain the temporal pulse information by monitoring the nonlinear interaction between two pulses the result of which is dispersed in a spectrometer of appropriate resolution to provide spectral information. While FROGs are standard technology for fs lasers, they are difficult to implement for ps laser pulses [24]. This is because the time-bandwidth product dictates that the longer a pulse is in time, the smaller its bandwidth; a transform limited 10 ps pulse has a total spectral bandwidth of ~ 0.1 nm. Resolving this spectrum requires a high-resolution spectrometer with minimal aberrations [24]. Gil and Simon [25] published a paper with a design for a high-resolution, aberration-corrected, flat-field, plane-grating spectrometer. This design uses off-axis parabolic collimating and camera mirrors to minimize astigmatism, coma, and field-curvature. The grating is placed so its dispersion plane is orthogonal to tangential plane of the off-axis parabolas. This produces a more flattened image by dispersing the Petzval field curvature and the image distortion resulting from the tilted grating along two orthogonal directions. Even though the design for this spectrometer was proposed in 1983, as far as I know, I am the first to build and characterize this spectrometer, the results which are presented in Chapter 7. In this chapter, the resolution of the violet Argon (I) doublet at 419.07 nm and 419.10 nm is shown as a demonstration of this

instruments characteristic $\frac{\lambda}{\Delta\lambda} = 2.5 \times 10^4$ resolving power. This resolving power is sufficient for use in ps FROG measurements.

2. BACKGROUND INFORMATION

2.1 Introduction

Some of the information presented in the following chapters assume a prior understanding of basic laser theory and nonlinear optics. This chapter will briefly present the background information and concepts necessary to understand the theory presented in the subsequent chapters. Specifically, section 2.2 will address basic laser theory topics such as population inversion and the relevant electronic structure of laser crystals. Section 2.3 will discuss thermal management issues inherent to Nd:GdVO₄ laser crystals. Section 2.4 defines concepts important to understanding gain saturation which, as is discussed in Chapter 4, plays an important role in mode locking dynamics . Finally, because this thesis deals with some non-linear optics, a brief overview of second harmonic generation and phase-matching will be presented in section 2.5. This chapter is not meant to be an overview of the fields of laser physics and nonlinear optics, for this I recommend Koechner ‘s “Solid State Laser Engineering” [51], Sieman’s “Lasers” [52], Shen’s “The Principles of Nonlinear Optics” [53], and Boyd’s “Nonlinear Optics” [54]. Rather, this chapter is intended to supply only the background information necessary to understand the rest of the thesis.

2.2 Basic Laser Theory

The word laser is an acronym corresponding to the phrase “light amplification by stimulated emission radiation”. Stimulated emission occurs when an incident photon of the appropriate energy enters a medium in which one or more atoms are in an excited electronic state causing an excited electron to transition to a lower state, which is generally called the ground state, thereby releasing a photon of the identical color (λ), phase, polarization, and propagation direction as the incident photon. Of course, if the electron is not in the excited state, but rather is in the ground state this same photon can be absorbed thereby promoting the electron to the appropriate excited state.

In order to achieve optical gain, it is necessary to generate a population inversion in the gain medium. That is, more electrons (per unit degeneracy) need to be in the desired excited state than are in the ground state. Of course, when the system is in thermal equilibrium at temperature T , the

Boltzmann distribution, $\frac{n_2}{n_1} = \frac{g_2}{g_1} e^{-\frac{E_2 - E_1}{k_B T}}$, describes the number of electrons in

the ground state (1), n_1 , which has degeneracy g_1 and energy E_1 compared to the number of electrons in the excited state (2), n_2 , which has degeneracy g_2 and energy E_2 (where $E_2 > E_1$ and $n_1 + n_2 = n_{total}$). Notice, that at room temperature the thermal energies, $k_B T \approx 0.01 - 0.1 eV$, where k_B is the

Boltzmann constant, the less energetic state is normally more heavily populated than the excited state. As a result, achieving population inversion

$\left(\frac{n_2}{n_1} > \frac{g_2}{g_1}\right)$ requires promoting the majority of the electrons from n_1 into n_2 .

This can be accomplished with a light source, such as a flash lamp, or it can be accomplished electronically in laser. Regardless of the specific method, the process of generating population inversion in a gain media is termed “pumping” the gain media.

2.2.1 The Two-Level System

It is instructional to consider first a two-level atomic system with an energy spacing corresponding to an optical frequency $\omega_{21} = (E_2 - E_1)/\hbar$ as shown in Figure 1.

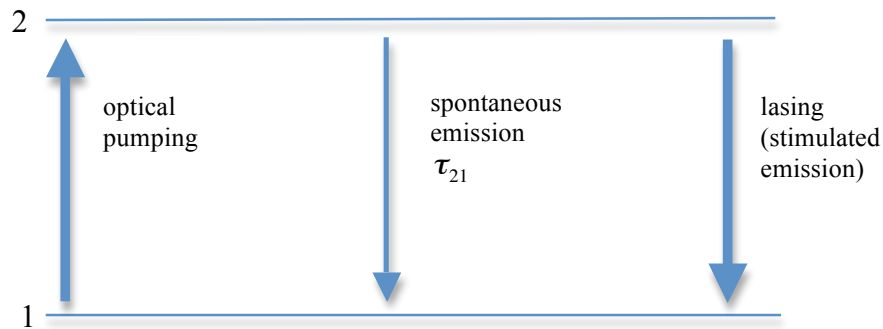


Figure 1. An energy-level diagram for a generic two-level system.

The differential equation describing the change in the population of level 1 due to absorption of energy as a function of time is given by

$$\frac{\partial n_1}{\partial t} = -B_{12}\rho(\omega)n_1 \quad (2.1)$$

where B_{12} is the Einstein B coefficient describing the “strength” of the atomic absorption and $\rho(\omega)$ is related to the pumping intensity or intra-cavity radiation. Thus, $B_{12}\rho(\omega)$ is the probability of absorption occurring as a function of frequency. The Einstein B coefficient is related to the absorption cross-section by $\sigma_{12}(\omega) = \frac{\hbar\omega_{21}}{c}B_{12}\ell(\omega)$ where $\ell(\omega)$ is the normalized lineshape function for the atomic transition $\left(\int_0^\infty \ell(\omega)d\omega = 1\right)$. Note that the cross-section’s dependence on frequency is not in the Einstein B coefficient, but is contained explicitly in the lineshape function. As a result, the peak value of $\sigma_{12}(\omega)$ may vary under the profile, but the area under the transition profile remains the same. This normalization of the lineshape allows $\sigma_{12}(\omega)$ for different media may be directly compared. The absorption cross-section, $\sigma_{12}(\omega)$, is related to the absorption coefficient, $\alpha_{12}(\omega)$, through $\alpha_{12}(\omega) = n_1\sigma_{12}(\omega)$.

For the case of a two-level system, there are two means by which the excited electron will return to the ground state. Firstly, an electron can be spontaneously emitted and return to the ground state while releasing a

photon of energy E_{21} . The rate equation corresponding to this spontaneous emission is described by

$$\frac{\partial n_2}{\partial t} = -A_{21}n_2 \quad (2.2)$$

where A_{21} is the Einstein A coefficient and is related to the radiative lifetime τ of the upper state and to the natural linewidth, $\Delta\nu$, of the atomic transition:

$$\begin{aligned} \Delta E \Delta t &\approx \hbar \\ \Rightarrow \Delta t \Delta \nu &\approx \frac{1}{2\pi}, \end{aligned} \quad (2.3)$$

since $\Delta t = \tau = \frac{1}{A_{21}}$, we obtain the relation $\Delta \nu = \frac{A_{21}}{2\pi}$.

Stimulated emission is the second possible method by which the excited electrons return to the ground state. In this case, an incident photon with a frequency corresponding to the energy difference of the electronic levels causes the transition of an electron from the excited state to the lower energy state. As a result of quantum mechanics, this transition causes a photon with the same wavelength, polarization, phase, and propagation direction as the incident photon to be emitted. This stimulated emission leads to a phase-coherent amplification of an applied signal, and a depletion of the excited state given by,

$$\frac{\partial n_2}{\partial t} = -B_{21}\rho(\omega)n_2, \quad (2.4)$$

where $B_{21}\rho(\omega)$ is the probability of stimulated emission occurring as a function of ω . In a similar manner to B_{12} , B_{21} is related to a cross-section σ_{21} , in this case for stimulated emission, via

$$\sigma_{21}(\omega) = \frac{\hbar\omega_{12}}{c} B_{21}\ell(\omega). \quad (2.5)$$

The Einstein-Milne relationships relate A_{21} , B_{12} , and B_{21} ,

$$g_1 B_{12} = g_2 B_{21}, \quad (2.5)$$

$$A_{21} = \frac{2\hbar\omega^3}{\pi c^3} B_{21}. \quad (2.6)$$

Combining the equations describing the change of population as the result of stimulated emission, absorption, and spontaneous emission gives the rate equation for a two-level electronic system

$$\frac{\partial n_1}{\partial t} = -\frac{\partial n_2}{\partial t} = B_{21}\rho(\omega)n_2 - B_{12}\rho(\omega)n_1 + A_{21}n_2. \quad (2.7)$$

In the steady-state, the number of electrons entering and exiting states 1 and 2 are the same, or $\frac{\partial n_1}{\partial t} = \frac{\partial n_2}{\partial t} = 0$ since $n_1 + n_2 = n_{tot}$. This implies the following:

$$B_{21}\rho(\omega)n_2 - A_{21}n_2 = B_{12}\rho(\omega)n_1 \quad (2.8)$$

$$\frac{n_2}{n_1} = \frac{B_{12}\rho(\omega)}{B_{21}\rho(\omega) - A_{21}} \approx \frac{B_{12}\rho(\omega)}{B_{21}\rho(\omega) \left[1 - \frac{2\hbar\omega^3}{\pi c^3 \rho(\omega)} + \dots \right]} \approx \frac{g_2}{g_1} \bigg|_{\rho(\omega) \rightarrow \infty}. \quad (2.9)$$

From equation 2.9 it can be seen that $\frac{n_2}{n_1}$ can at most be equal to, but never

greater than $\frac{g_2}{g_1}$ and thus, lasing with a two-level system is not possible; at

minimum, a three-level system is needed. In fact, the ruby laser is a good

example of a well-known three-level system. Because this thesis does not deal with three-level systems, they will not be considered here.

2.2.2 The Four-Level System

This thesis deals with Neodymium doped Gadolinium Vanadate (Nd:GVO₄), a four-level laser system. The specifics of Nd:GdVO₄'s energy levels are discussed in the following section (2.3). Here, I will present a generic four-level system in which the lasing occurs between levels (2) and (1) as shown in Figure 2.3. Pumping the laser crystal excites electrons from the ground state, level (0), to level (3). A rapid, radiationless transition, S_{32} , occurs transitioning the electrons from level (3) to the upper lasing level (2). The electrons transition between level (2) and (1) by either spontaneous or stimulated emission. Another rapid, radiationless transition, S_{10} , drains the electrons from the lower lasing level (1) back to the ground state (0). Because $S_{10} > A_{21} = 1/\tau_{21}$, a population inversion can be easily achieved because $n_1 \approx 0$.

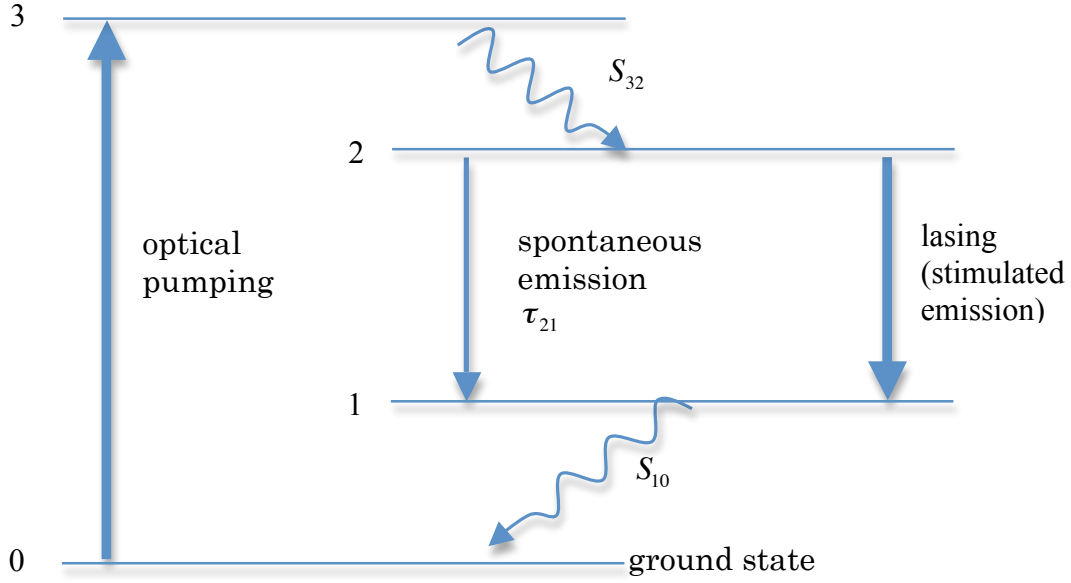


Figure 2.3 shows an energy-level diagram for a generic four-level system.

The rate equations for the major transitions of a four-level system when the radiationless S_{10} and S_{32} are large:

$$\frac{dn_0}{dt} = n_1 S_{10} - n_0 \rho_{03} B_{03} \quad (2.10a)$$

$$\frac{dn_1}{dt} = n_2 (A_{21} + \rho_{12} B_{21}) - n_1 (S_{10} + \rho_{12} B_{12}) \quad (2.10b)$$

$$\frac{dn_2}{dt} = n_3 S_{32} + n_1 \rho_{12} B_{12} - n_2 (A_{21} + \rho_{12} B_{21}) \quad (2.10c)$$

$$\frac{dn_3}{dt} = n_0 \rho_{03} B_{03} - n_3 S_{32} \quad (2.10d)$$

where I have used the standard “definitions”; i.e., $\rho_{ij}B_{ij}$ is the probability of an electron being absorbed for radiation at frequency $\omega_{ij} = \frac{E_i - E_j}{\hbar}$. In the steady-state, the same number of electrons are entering and leaving energy level 2, $\frac{dn_2}{dt} = 0$, which leads to $n_2 = \left(\frac{S_{10} + \rho_{12}B_{12}}{A_{21} + \rho_{12}B_{21}} \right) n_1$. As the condition for population inversion is $n_2 > \frac{g_2}{g_1} n_1$, this means that population inversion is achieved if the following condition is met:

$$\frac{S_{10} + \rho_{12}B_{12}}{A_{21} + \rho_{12}B_{21}} > \frac{g_2}{g_1} \quad (2.11a)$$

$$\Rightarrow S_{10} + \rho_{12}B_{12} > \frac{g_2}{g_1} (A_{21} + \rho_{12}B_{21}) \quad (2.11b)$$

using the relation $\frac{g_2}{g_1} B_{21} = B_{12}$, the condition to achieve population inversion in

a four-level system simplifies to $S_{10} > \frac{g_2}{g_1} A_{21}$. This implies that either i) the

transition from the lower lasing level (level1) to the ground state must be fast or ii) the excited laser level should be metastable – a large τ_{21} and therefore A_{21} is small. Conditions i) and ii) may also coexist. Four-level laser systems are widespread -- Nd:GdVO₄, Nd:YAG, Nd:YVO₄ are commonly used four-level laser systems, as are most semiconductor lasers, and the well-known HeNe and Ti:Al₂O₃ lasers are also four-level systems.

Clearly such four-level lasers require that the pump energy $\hbar\omega_{13}$ exceeds the emitted photon energy $\hbar\omega_{21}$. The excess energy is dissipated as

heat in the rapid, radiationless transitions that occur between energy levels 3 and 2 (S_{32}) and 1 and 0 (S_{10}). The energy difference between the pump energy level and the emission energy is commonly referred to as the Stokes shift or quantum defect for the laser gain media. The resultant heat deposited into a laser crystal generates thermal issues that must be managed.

2.3 Nd³⁺ Ion, Heat Management, and Crystal Geometry

Figure 2.4 [1] shows an energy diagram for a Nd:GdVO₄ gain media. At the top are two flash lamp absorption pump bands, one in the blue and the other in the green. Also shown as are two absorption lines at 808 nm and 879 nm. Most Nd³⁺-doped lasers are pumped at 808nm by solid-state laser diodes and emit at 1.063μm (Nd:GdVO₄) or 1.064μm (Nd:YAG and Nd:YVO₄). For this case, there is a 24% quantum defect. The resultant heat is deposited into the crystal and produces thermal lensing, thermal stress birefringence, and possibly catastrophic physical damage to the gain medium. The particular temperature distribution within any given crystal is the result of such details as the geometry of the crystal, the pumping, and the cooling. Efficient heat removal and minimization of thermal gradients particularly in the region of the crystal through which the laser passes avoids complications and is highly desirable for minimization of thermal effects.

A Brewster-angled slab laser crystal has many advantages. In this geometry a p-polarized laser will, of course, experience zero loss to reflection. This results in low insertion losses for the laser gain medium and eliminates the need for antireflection coatings. A Brewster crystal gain media can also be efficiently cooled through top and bottom surfaces thereby generating a predominantly one-dimensional temperature gradient. The issue with using a Brewster-angled slab geometry is that the pump-induced thermal lens is generally astigmatic; i.e., has different focal lengths for the tangential (x) and sagittal (y) directions. Chapter 3 describes how the effects of astigmatism in the Brewster-angled Nd:GdVO₄ laser crystal used in this work were abated.

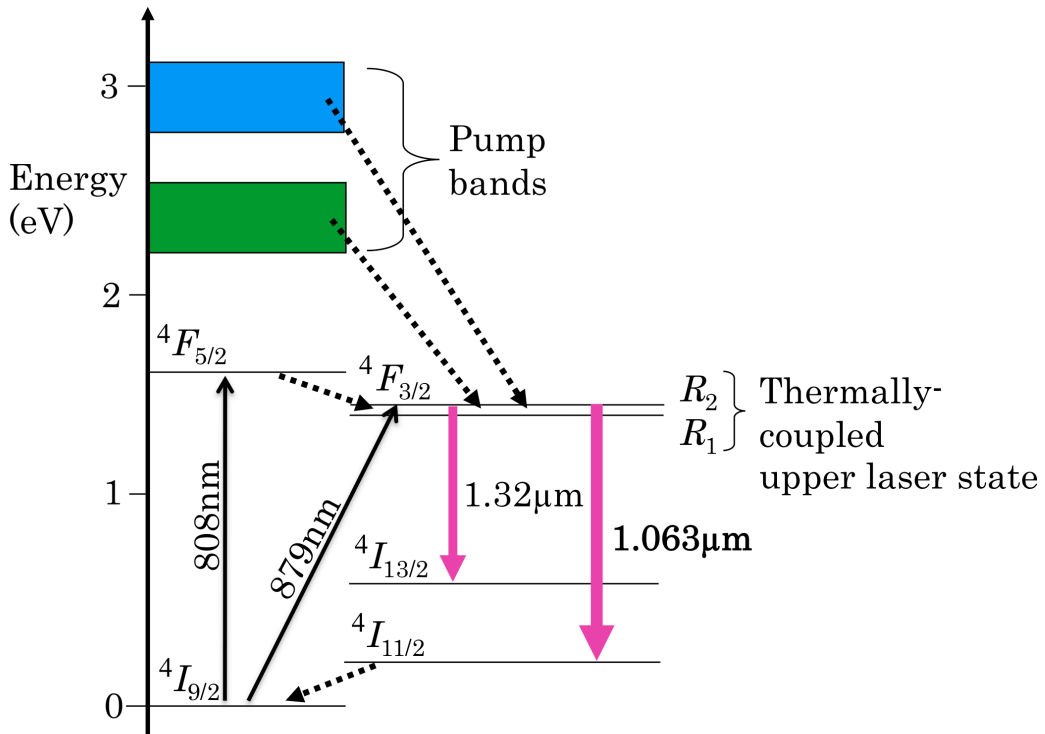


Figure 4. An energy diagram for Nd³⁺ ion [56].

A thermal gradient in a laser crystal results in a spatial variation of the temperature dependent refractive index. The strength of this effect is quantified by the thermo-optic coefficient, $\frac{dn}{dT}$. Additionally, if the heat is removed from the outside surfaces of the crystal, as is most often the case, the temperature at the center of the crystal will be higher than the external portions of the crystal. This situation leads to mechanical stress within the crystal which in turn result in changes of the refractive index through photo-elastic effects. The photo-elastic effect is described by a fourth order tensor comprised of elasto-optical coefficients that are material specific [2]. The refractive index of a material is specified by its indicatrix which usually forms an ellipsoid. Stresses cause a mutation of the indicatrix which results in birefringence (or a different refractive index for different polarizations) since, generally speaking, the stress in the direction parallel to the temperature gradient, $\vec{\nabla}T$, does not equal that in the orthogonal direction. The total change of refractive index is a result of both stress and temperature gradient. If $n(r)$ is the refractive index, $\Delta n(r)_T$ is the temperature dependent change in refractive index, and $\Delta n(r)_\varepsilon$ is the change in refractive index due to stress, then the refractive index can be written as

$$n(r) = n_o + \Delta n(r)_T + \Delta n(r)_\varepsilon. \quad (2.12)$$

For uniaxial laser crystals stress-birefringence is not zero ($\Delta n_e \neq 0$) but, this effect is much less than $\Delta n = n_e - n_o$, so it is inconsequential. However, for an isotropic crystal, such as Nd:YAG, Δn_e can have a significant effect unless the temperature gradient is parallel or perpendicular to the direction of laser propagation. The Brewster-angled slab Nd:GdVO₄ laser crystal used in this thesis is uniaxial and thus does not have stress-birefringence, so that only the first two terms of Equation 2.12 are relevant. Of course, heat deposited in a crystal will also result in an expansion of the material in an amount proportional to the appropriate thermal expansion coefficient, α_T . Thermal lensing is the cumulative optical distortion of the laser beam that results from temperature gradients, strain, and expansion [2].

2.4 Gain Saturation

A further important concept, particularly for mode locking is gain saturation. At laser threshold, which is characterized by the steady state condition $\frac{dn}{dt} = 0$, photon flux or stimulated emission can be taken to be zero [2]. The small signal gain is given by

$$g_0 = \sigma_{21} n_{tot} \frac{W_p \tau_f - (\gamma - 1)}{W_p \tau_f + 1} \quad (2.13)$$

where W_p is the pumping rate, $\tau_f = \tau_{21}$ for a four-level system, and $\gamma = 1 + \frac{g_2}{g_1}$ [2].

When lasing is permitted, the irradiance (idiomatically referred to as

intensity), I , in the cavity increases exponentially and the gain of the system is reduced according to

$$g = \frac{g_0}{1 + I/I_{sat}}$$

where $I_{sat} = \frac{h\nu}{\sigma_{21}\tau_f}$, for a four-level system. It may be helpful to note the small signal gain is a function of material parameters only while the saturated gain depends upon the power density, irradiance, in the cavity.

2.5 Nonlinear Optical Effects

Yet another important (and sometimes deleterious) subject in ultrafast laser physics is nonlinear optics. When a laser beam propagates through a material, its oscillating electric field exerts a force on the valence electrons and causes them to be perturbed from their normal orbits; dipoles are formed. On a macroscopic level, the material becomes polarized. This polarization, P_l can be expanded as [51]

$$P_l(\omega_1) = \chi_{lm}^{(1)} E_m(\omega_1) + \dots + \chi_{lmn}^{(2)} E_m(\omega_2) E_n(\omega_3) + \chi_{lmnp}^{(3)} E_m(\omega_2) E_n(\omega_3) E_p(\omega_4) + \dots \quad (2.14)$$

where P is a polarization vector, E is an electric field vector, and $\chi^{(1)}$ is a tensor of the second rank, $\chi^{(2)}$ is a vector of the third rank, and $\chi^{(3)}$. The frequency components are indexed by 1, 2, 3, and 4 while l , m , n , and p represent Cartesian coordinates.

Second harmonic generation is a special case of the $\chi^{(2)}$ effect given by

$$P_l(2\omega_2) = \chi_{lmn}^{(2)} E_m(\omega_2) E_n(\omega_2) . \quad (2.15)$$

This can be thought of as a two-step process. First, a polarization wave at $2\omega_2$ is produced. This has a phase velocity and a wavelength in the medium determined by the fundamental frequency. In the next step, energy is transferred from this polarization and reradiated at the second harmonic (with phase velocity and wavelength determined by the second harmonic). Clearly for efficient generation, these two waves need to remain in phase. This is called phase matching and it occurs when the phase mismatch, $\Delta k = 0$ where $\Delta k = \frac{4\pi}{\lambda_1}(n_1 - n_2) = 2k_\omega - k_{2\omega}$. Most often, when using a SHG, the end goal is to efficiently generate second harmonic and as a result it is desirable to operate as close to phase matching ($\Delta k = 0$) as possible. For the dual-passive mode locking scheme described in Chapter 5, it is actually desirable to operate with a phase mismatch.

Third-order effects are also important. While the $\text{Im}[\chi^{(3)}]$ leads to two photon absorption (TPA), the $\text{Re}[\chi^{(3)}]$ produces self-phase modulation. This effect results in an intensity-dependent index of refraction. In some cases, such as that of a pulse propagating through an optical fiber, the intensity is time dependent. As a result, the refractive index also has a time-dependence $n(\omega, I) = n_o(\omega) + n_2 I(t) = n_o(\omega) + \Delta n(t)$. This directly implies a time-dependent phase

change $\Delta\phi(t) = \frac{2\pi}{\lambda} n_2 I(t) l$ where l is the length of the fiber. The additional generated bandwidth is given by $\Delta\omega = \frac{\Delta\phi}{\Delta t}$.

3. THERMAL-LENS-SHAPED Nd:GdVO₄ LASER OSCILLATOR

3.1 Introduction

The solid-state pumped Nd:GdVO₄ oscillator utilized in this thesis employs a thermal lens shaped, Brewster-cut gain media laser head. As mentioned in section 2.3, the Brewster geometry has near-zero intra-cavity loss due to reflection from the gain media for linear p-polarization and, as a result, the laser head strongly favors oscillation of linear, p-polarized radiation. Additionally, the p-polarization optical damage threshold is high for the Brewster-cut gain crystal, in part because no anti-reflection dielectric coating is needed. One significant disadvantage to this laser head geometry is that the inherent astigmatism of the Brewster-cut geometry generally results in an elliptical spatial laser beam [62]. In the laser oscillator presented and used in this thesis, however, an astigmatism compensation scheme specific to axially laser diode pumped Brewster-cut gain media is employed. In this laser head design, the pump spot size spot size in the tangential and sagittal directions are manipulated until the thermal lens is be shaped such that the resonator sees an overall stigmatic lens associated with the gain medium [57].

3.2 Thermal Lens Shaping Theory

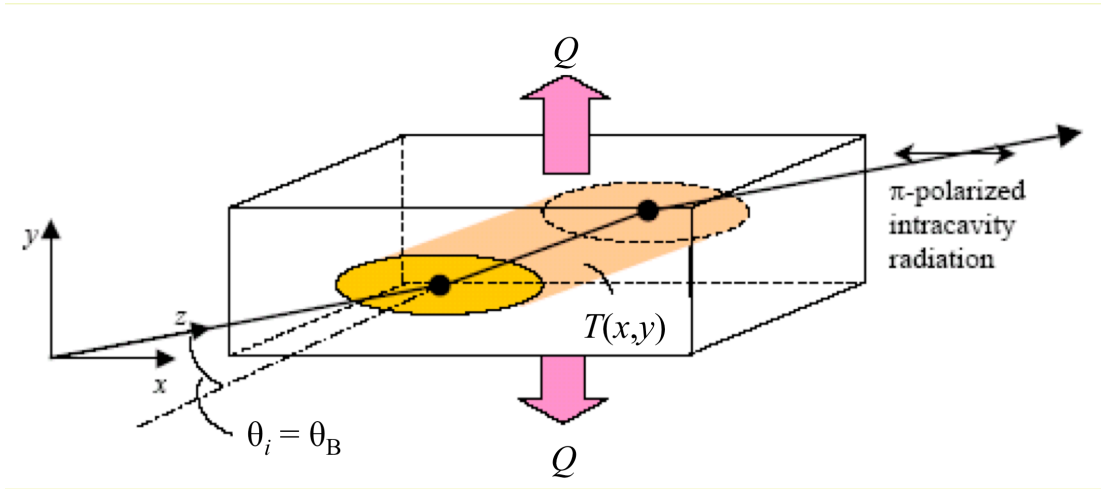


Figure 3.1 A schematic of a Brewster-cut slab laser crystal. The elliptical pump spot size is shown in yellow. The heat, Q , is removed from the top and bottom surfaces as indicated by the pink arrows. The intracavity laser beam is incident at Brewster's angle to the laser crystal thereby eliminating intracavity loss to the desired p-polarized laser beam. (reproduced with permission [67])

The Brewster-cut Nd:GdVO₄ gain media used in this laser head employs the slab geometry. The heat is conducted out of the large top and bottom faces of the 3x5x10mm crystal through large brass blocks which are water cooled and held at a constant temperature by a chiller. A highly thermally conductive paste [58] improves the thermal contact between the crystal and the brass blocks. As a result of this arrangement, the heat flow is nearly completely in one dimension [64, 65], so that the temperature profile in the x- and y- directions are decoupled thereby allowing the overall thermal lens to be manipulated by changing the aspect ratio of the pump spot size.

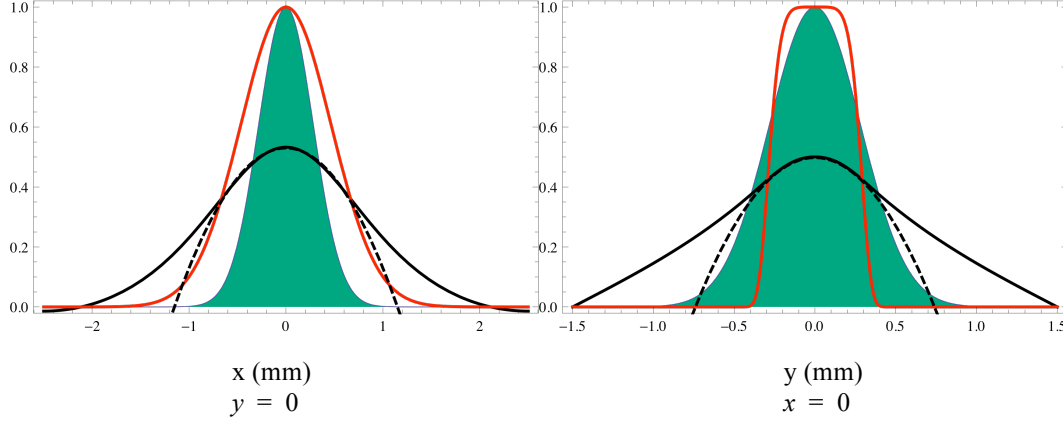


Figure 3.2 Solid black line indicates the temperature profile as a function of x (left) and y (right) that results from a pump laser heat source with a spatial profile shown by the red line. The dashed black line indicates the parabolic fit to the temperature profile while the green form is the profile of the incident laser beam.

The resulting temperature distribution, shown in Figure 3.2, in the gain media can be found by solving the two-dimensional heat equation

$$\kappa_{th} \left(\frac{\partial^2 T}{\partial x^2} + \frac{\partial^2 T}{\partial y^2} \right) = Q_0 \exp \left[-\frac{x^2}{w_{p,x}^2} - \left(\frac{y^2}{w_{p,y}^2} \right)^3 \right], \text{ where } \kappa_{th} \text{ is the thermal conductivity of}$$

Nd:GdVO_4 , Q_0 is the heat in W/m^3 , and $w_{p,x}$ and $w_{p,y}$ are the $HW \frac{1}{e}$ spot

sizes of the pump radiation incident on the laser crystal in the x and y -

directions, respectively. Notice the heat source term is Gaussian in the x -

direction and a super-Gaussian of order 3 in the y -direction. As will be

discussed shortly, this appropriately describes the pump profile of the diode

output in the laser crystal. A finite cosine transformation is performed to

solve the heat equation using the boundary conditions corresponding to a

temperature at the top and bottom of the gain media equal to the temperature of the chiller ($T(x, \pm 1.5 \text{ mm}) = T_{\text{chiller}}$) and that all of the heat conduction is in the y -direction ($\left. \frac{dT}{dx} \right|_{x=\pm 2.5 \text{ mm}} = 0$). Figure 3.2 shows the resulting temperature profile, indicated by the solid black line, is nicely approximated by a parabola (dashed black line) over the region of the laser pulse which is represented in green. Hence, to a good approximation, the asymmetrically longitudinally pumped, laser diode Brewster-cut geometry produces a temperature profile (in the paraxial approximation) of the form [51]

$$T(x, y) = T_o - \frac{1}{2}(A_r x^2 + B_r y^2). \quad (3.1)$$

The coordinates are defined such that $T_o = T(x = 0, y = 0)$ is the peak axial temperature. Pump beam absorption and possible thermal lens induced focusing [51] over the crystal length l generally results in the values of A_r and B_r being functions of the axial coordinate z . However, in this case, the counter-propagating pump beams have an absorption-length product $\alpha l \approx 2$ which allows A_r and B_r to be approximated as constants with values that depend primarily on the pump beam profile dimensions and the thermal conductivity of the laser crystal.

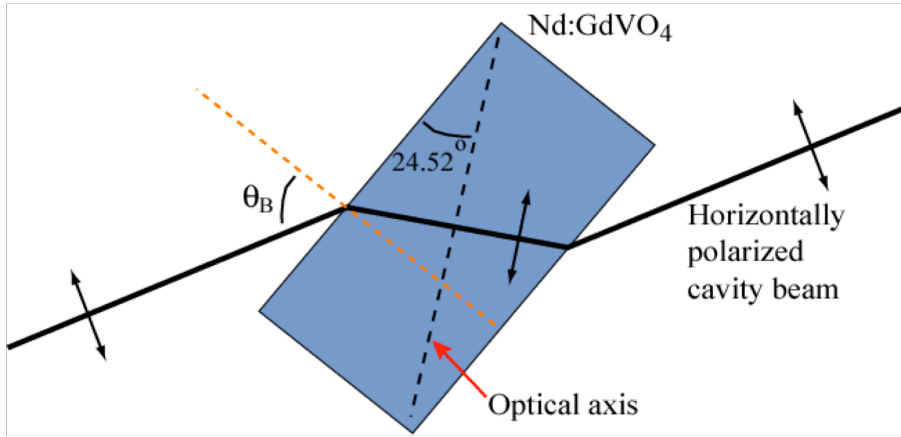


Figure 3.3 This figure shows the cut of the Nd:GdVO₄ laser crystal. The optical axis is shown as the dotted line while the path of the laser beam is shown by the solid black line. (reproduced with permission [67])

As discussed in Section 2.3, in general, there are three contributions to the overall thermal lens of the gain media which are generated by a given temperature profile. First, an astigmatic gradient index lens (GRIN) lens is formed through the bulk thermo-optic effect $\left(\frac{dn}{dT}\right)$. Second, a refractive lens results from the bowing of the two crystal faces due to thermal expansion. Third, a generally non-symmetric lens is produced by the stress-induced changes in the refractive index resulting from $\bar{\nabla}T$ (i.e., thermal conduction). In the particular case of the thermal lens shaped geometry, this last contribution is essentially eliminated because the polarization of the laser

beam is perpendicular to the temperature gradient. Furthermore, the Nd:GdVO₄ laser head presented in this case is uniaxial with the preferred emission (largest emission cross-section σ_{21}) parallel to the c-axis (Figure 3.3) which is oriented perpendicular to $\vec{\nabla}T$. Hence, Δn_e is generally much less than the natural crystal birefringence of Nd:GdVO₄, this contribution to the pump-induced thermal lens is insignificant.

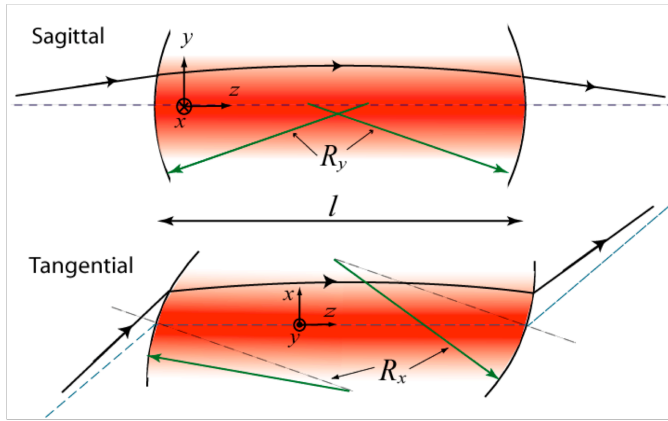


Figure 3.4 shows the thermal lens effect in the gain media is shown from the sagittal (or side) view and the tangential (or top) view. The arrows trace the laser beam path. (reproduced from [57])

The net GRIN lens that results from the thermal lens effects in the tangential (x) and sagittal (y) directions is shown by the shaded region in Figure 3.4. Ray transfer matrices (RTMs) can be used to represent the optical effects of both the GRIN lens and the bowing of the crystal ends [59]. The net RTM in the tangential plane is given by

$$\begin{pmatrix} A & B \\ C & D \end{pmatrix}_x = \begin{pmatrix} \frac{1}{n} & 0 \\ -\frac{\Delta_x}{R_x} & n \end{pmatrix} \begin{pmatrix} 1 & \frac{l}{n} \\ -n\gamma_x^2 l & 1 \end{pmatrix} \begin{pmatrix} \frac{n}{R_x} & 0 \\ -\frac{1}{n} & 1 \end{pmatrix} \quad (3.2a)$$

$$= \begin{pmatrix} 1 - \frac{\Delta_x l}{n^2 R_x} & \frac{l}{n^3} \\ \frac{\Delta_x^2 l}{n R_x^2} - \left[n^3 \gamma_x^2 l + \frac{2n\Delta_x}{R_x} \right] & 1 - \frac{\Delta_x l}{n R_x} \end{pmatrix} \quad (3.2b)$$

The RTM in the sagittal plane is given by

$$\begin{pmatrix} A & B \\ C & D \end{pmatrix}_y = \begin{pmatrix} \frac{1}{n} & 0 \\ -\frac{\Delta_y}{R_y} & n \end{pmatrix} \begin{pmatrix} 1 & \frac{l}{n} \\ -n\gamma_y^2 l & 1 \end{pmatrix} \begin{pmatrix} \frac{1}{R_y} & 0 \\ -\frac{\Delta_y}{n} & 1 \end{pmatrix} \quad (3.3a)$$

$$= \begin{pmatrix} 1 - \frac{\Delta_y l}{n R_y} & \frac{l}{n} \\ \frac{\Delta_y^2 l}{n R_y^2} - \left[\gamma_y^2 l + \frac{2\Delta_y}{R_y} \right] & 1 - \frac{\Delta_y l}{n R_y} \end{pmatrix} \quad (3.3b)$$

In the above equations, n is the refractive index and l is the Nd:GdVO₄ crystal length. GRIN lens coefficient γ_i and positive bowing radii of curvature R_i are assumed to be different in the tangential and sagittal directs as a result of the thermal spatial profile. The constants Δ_y and Δ_x are given by

$$\Delta_y = n \sin \theta_B - \cos \theta_B \quad (3.4a)$$

and

$$\Delta_x = \frac{\Delta_y}{\sin \theta_B \cos \theta_B} \quad (3.4b)$$

where $\theta_B = \tan^{-1}(n)$ is Brewster's angle. It can be seen from equations (3.3) that in the 'thin lens' approximation ($f_T \gg l$), which is valid in our circumstance, the terms in the square bracket will dominate the thermal lens. Furthermore, since for a thin optical system, the focal length is given by the ratio $-\left(\frac{A}{C}\right)$, the condition to obtain a stigmatic lens ($f_{Tx} = f_{Ty}$) from a Brewster-cut gain media is given by

$$n\gamma_y^2 l + \frac{2\Delta_y}{R_y} \approx n^3 \gamma_x^2 l + \frac{2n\Delta_x}{R_x}. \quad (3.5)$$

The gamma factors depend on the change in refractive index that results from the thermal gradient in the crystal. In section 2.3 it was shown that $\Delta n(x, y) = \frac{dn}{dT} \Delta T$. Assuming the elliptical parabolic temperature profile of equation (3.1) this becomes $\Delta n(x, y) = -\frac{1}{2} \frac{dn}{dT} (A_T x^2 + B_T y^2)$. As, the refractive index can be expanded as $n(x) = n_o - \frac{1}{2} n_2 x^2 = 1 - \frac{1}{2} \gamma^2 x^2$ where $\gamma^2 = \frac{n_2}{n_o}$, the condition for stigmatic lensing becomes

$$B_T \frac{dn}{dT} l + \frac{2\Delta_s}{R_y} \approx n^2 A_T \frac{dn}{dT} l + \frac{2n\Delta_t}{R_x}. \quad (3.6)$$

The thermal gradient in the gain media results in compression stresses in the center of the gain media while the surface is under tension stress [63]. The maximum stress occurs at the center and the ends of the gain media. That is to say, the entire length of the gain media does not contribute to the bowing of the edges; only a length, d_T , contributes. Koechner [51, 63] reports that this distance varies with the thermal properties of the gain medium and is roughly equal to the diameter of the gain media for Nd:glass and is half that for Nd:YAG. With this understanding, the radius of curvature due to bowing from a Gaussian temperature profile is given by

$$R_x = -\left(\frac{d^2}{dx^2}(\Delta l)\right)^{-1} = \left(\frac{d^2}{dx^2}(\alpha_T d_T \Delta T)\right)^{-1} = \left(\frac{1}{2} \alpha_T d_T A_T \frac{d^2}{dx^2}(x^2)\right)^{-1} \quad (3.7)$$

where α_T is the thermal expansion coefficient. To first order, the radii of curvature are then

$$R_x \approx \frac{1}{\alpha_T d_T A_T} \text{ and } R_y \approx \frac{1}{\alpha_T d_T B_T}. \quad (3.8)$$

The resulting required condition for a stigmatic thermal lens is that

$$B_T \left\{ \left(\frac{dn}{dT} \right) l + 2\Delta_y \alpha_T d_T \right\} = A_T \left\{ n^2 \left(\frac{dn}{dT} \right) l + 2n\Delta_x \alpha_T d_T \right\}. \quad (3.9)$$

3.3 Shaping of the Thermal Lens

As shown in Figure 3.5, the gain medium is end pumped through both polished sides by two 40W 808nm laser diode (LD) bars with output at 808nm. The LD radiation is partially collimated in the sagittal plane by a cylindrical lens ($f = 10\text{mm}$) and thereafter focused into the gain medium by a spherical lens ($f = 20\text{mm}$). Laser oscillation at Brewster's angle renders anti-reflection coatings unnecessary. Furthermore, good spatial separation of the pump and laser beams is allowed for by assuring the pump radiation is incident at $15\text{-}45^\circ$ to the crystal face. Such a large angle means that dichroic coatings, an additional loss for the pump and/or the laser, are not necessary. Inside the laser crystal the angular separation of the counter propagating pump beams and the laser is $\sim 15^\circ$. This is small enough to allow for efficient quasi-longitudinal pumping over the entire 5mm crystal length; the resulting 600-700 μm spatial walk-off is less than half of the $\sim 2\text{mm}$ tangential laser beam size inside the gain medium.

The position of the cylindrical lens (L2) with respect to the LD controls the aspect ratio of the pump beam's ellipticity. Specifically, the position of the cylindrical lens determines the width of the pump beam in the sagittal plane while the pump beam size in the tangential plane is held constant by the static spherical lens (L1). As a result, the ellipticity of the pump-induced

thermal lens can be manipulated to meet the condition for stigmatic lensing given in equation 3.9. The appropriate necessary constants for the Brewstser-cut Nd:GdVO₄ laser head presented in this thesis are $n = n_e = 2.198$ [63], $\frac{dn}{dT} = \frac{dn_e}{dT} \approx 4 \times 10^{-6} \text{K}^{-1}$ [52, 66], and $\alpha_T \approx 7.9 \times 10^{-6} \text{K}^{-1}$ [74]; so that equation (3.9) gives $A_T/B_T \approx 0.19$. That is, the thermal lens in the sagittal plane should be five times stronger than that of the tangential plane to present an overall stigmatic thermal lens to the laser cavity.

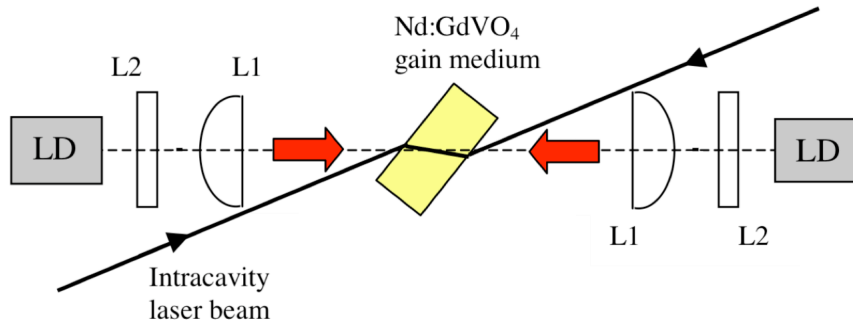


Figure 3.5 This figure shows the laser diodes (LD), the cylindrical (L2) and spherical (L1) lenses as well as the Nd:GdVO₄ gain medium and the intracavity laser beam. (reproduced from [57])

A detailed ray tracing with the appropriate divergence in the x and y directions is shown in Figure 3.6. A weighted average of the pump rays at the center of the gain crystal reveal that the pump profile has a Gaussian

shape in the x direction and is a superGaussian of order three in the y direction (as a result of spherical aberration). As mentioned in section 3.2,

the heat equation of form $\kappa_{th} \left(\frac{\partial^2 T}{\partial x^2} + \frac{\partial^2 T}{\partial y^2} \right) = Q_0 \exp \left[-\frac{x^2}{w_{p,x}^2} - \left(\frac{y^2}{w_{p,y}^2} \right)^3 \right]$ can then be

solved to determine the temperature profile inside the laser crystal. And it is

determined that achieving $\frac{A_T}{B_T} \approx 0.19$ requires a pump spot size ratio of

$$\frac{w_{px}}{w_{py}} \approx 3.$$

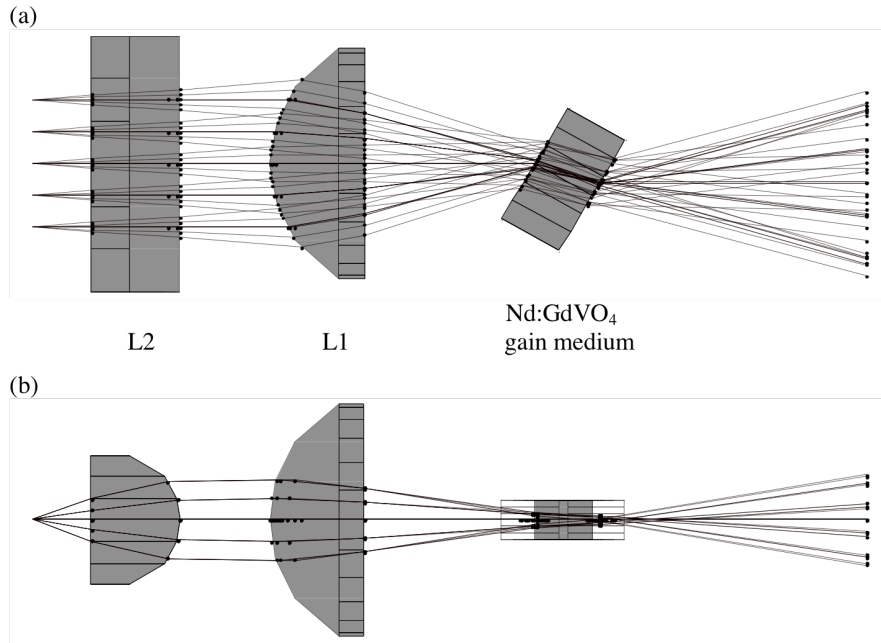


Figure 3.6 shows a ray tracing of the pump radiation through the a) horizontal and b) vertical planes of the gain media. (reproduced from [57])

3.4 Laser Oscillator Characterization

Plane-plane resonators of varying length and with the gain media positioned at the center of the cavity were used to assess the performance of this Brewster-cut NdGdVO₄ laser head [57]. Figure 3.7 shows laser output as a function of diode drive current for different symmetric resonator lengths all having a near optimum output coupling of 8%. [57] The shortest cavity of length 32cm gives 20W of output power at a laser diode current of 41A. This corresponds to an overall efficiency (given by the ratio of the output power to the pump power) of 32%, or, equivalently, a laser-output to absorbed-pump-power efficiency (i.e, the ratio of the output power to the amount of pump power absorbed by the gain medium after reflective losses resulting from for the incident pump radiation from the lenses and gain medium have been accounted for) of 41%. The initial optical-to-optical slope efficiency is common to all the resonators is 37(±2)%. This slope efficiency is comparable to conventional fiber-coupled LD end-pumped geometries which have values ranging from 35% - 50% [52, 60, 61, 68, 69]. It is also similar to some of the more efficient laser diode end pumped Nd:GdVO₄ slab lasers which have efficiencies that range from 35% -45%. [70-73]

As the cavity length is increased, Figure 3.8 shows a reduction in output power at high diode pump powers. This is because the stability threshold ($\frac{1}{f_T} < \frac{L}{4}$, where L is the cavity length) for symmetric cavities is

being approached and the pump/laser beam overlap is degraded. Moreover, the pump/laser beam overlap in the gain media is degraded due to larger spot sizes for longer cavities. That is to say, the laser mode in the gain medium begins to exceed the 1mm sagittal spot size of the diode pump radiation. The solid black line in Figure 3.8 indicates this boundary between stability regions I and II. There is very little power drift (less than 1% per hour) of the output when the laser is operating in stability region I. Operation in region II is less stable due primarily to fluctuations in the transverse mode.

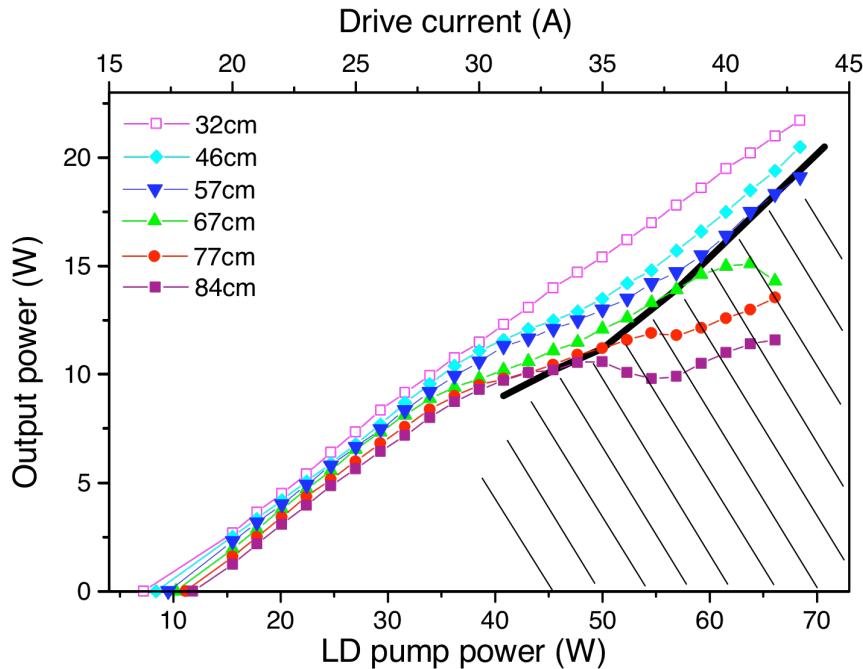


Figure 3.7 shows output power as a function of diode pump power for different symmetric resonator lengths. All curves are for 8% output coupling. The black line indicates the boundary between stability region I and stability region II. (reproduced from [57])

A radially symmetric (i.e., stigmatic) thermal lens was ensured in practice by adjusting the position of the cylindrical lens (L2) until the fundamental TEM₀₀ mode transitions smoothly into the donut mode (radial TEM₁₀) with an increase in diode current. If the position of the cylindrical lens is too far towards the gain medium, the mode will instead transition into a horizontal TEM₁₀ mode. If cylindrical lenses are not close enough to the gain medium, the cavity will prefer to oscillate in a vertical TEM₀₁ mode. It has been experimentally determined that for the condition of Equation (3.9) to be met, the cylindrical lenses must be positioned correctly to ± 1 mm.

The characteristics of the laser beam resulting from the 67cm cavity and 8% output coupler were analyzed to verify the temperature distribution of the gain media does produce an astigmatic lens and are shown in Figure 3.9. The M^2 and spot size of the embedded TEM₀₀ mode were obtained using the knife-edge technique [12]. The results displayed in Figure 3.9 show that the fundamental mode is indeed circular to within the $\pm 5\%$ error of the measurement technique. The trend towards decreasing spot size at the output coupler with increasing diode power is predicted by the RTM for a symmetric resonator. The smallest size of ~ 350 μm corresponds to the confocal cavity condition where $w_o = 337$ μm and represents the point beyond which the resonator becomes unstable.

The values of $M^2 = \sqrt{M_x^2 + M_y^2} < 1.1$ shown in Figure 3.8 indicate the laser produces a high quality TEM₀₀ mode from the threshold driving

current to output up to a driving current of 25A (6.5 W of output power).

Between 25 and 29A the beam quality in the y (or sagittal) plane remains high while the M_x^2 grows to about 1.8. This behavior is not unexpected as the pumped region of the gain medium provides gain for low-power higher-order horizontal mode oscillation outside the TEM₀₀ mode width. It is important to note, there are no mode-control apertures in the cavity to prevent higher-order modes from lasing. As the pump current increases past 29A, mismatch in the TEM₀₀ laser beam and pump spot size occurs. Even so, this resonator maintains an M^2 of less than 2 throughout the entire stability region I.

Increasing the flat-flat cavity length will result in a better M^2 beam quality, but reduced output power as a result of the larger TEM₀₀ size that needs to be supported at longer thermal focal lengths. In contrast, the higher power shorter resonators produce higher power output beams with lower beam quality; an $M^2 \sim 5$ is produced with 20W output power for the 32 cm cavity length.

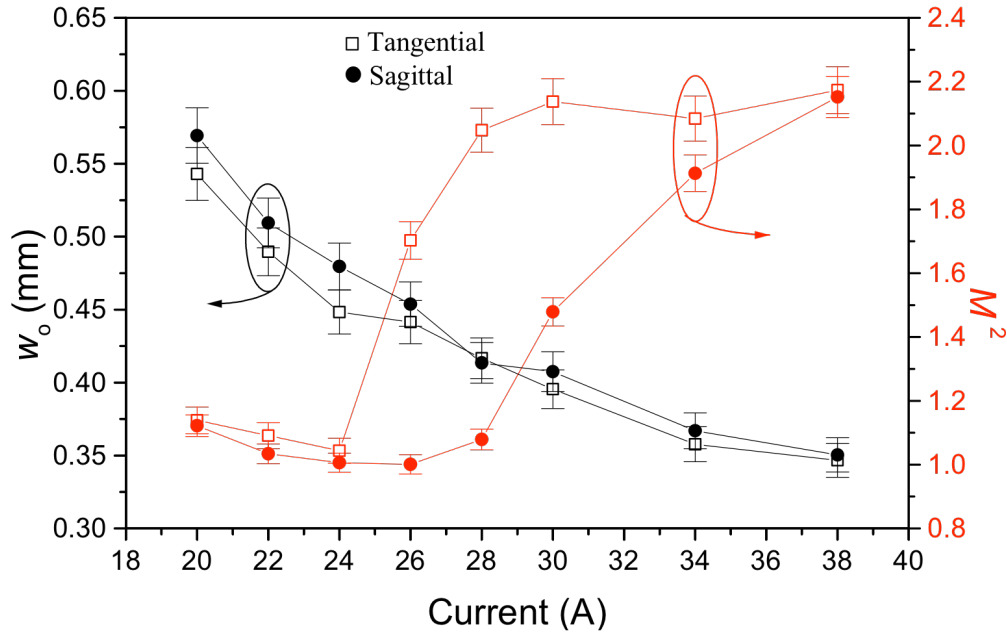


Figure 3.8 shows the spot size is shown along the left axis as a function of diode current. The M^2 as a function of current is shown along the right hand axis. (reproduced from [57])

The measured embedded TEM₀₀ spot sizes w_0 at the output coupler allow the power of the thermal lens in the diode-pumped Nd:GdVO₄ gain medium to be determined as a function of the diode current or pump power. The results of this calculation are shown in Figure 3.9. As expected, the thermal focal power ($1/f_T$) is a linear function of the pump power (i.e., LD drive current for the presented range), and zero focal power is consistent with the ~14A LD current threshold. This set of data is used to define the boundary (confocal condition) between the first and second stability regions for the symmetric resonators in Figure 3.7; that is, for each cavity length L ,

the drive current corresponding to the condition $f_T = L/2$ is found to allow the boundary (solid black line) to be plotted.

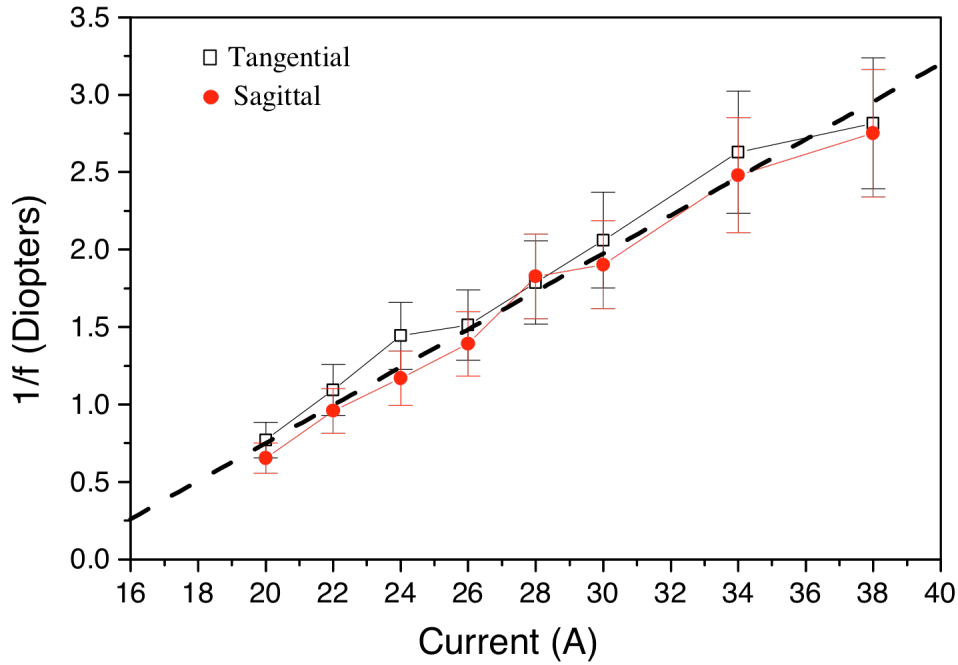


Figure 3.9 shows the power of the pump-induced thermal lens in the Brewster-cut Nd:GDVO₄ gain medium evaluated as a function of LD drive current for both the tangential (x) and sagittal (y) directions. (reproduced from [57])

3.5 Modifications for Mode Locking

Nearly all spectroscopic applications require a TEM₀₀ mode. Moreover, a single transverse mode (i.e., a TEM₀₀ mode) is preferred for mode locking (which will be discussed in detail in Chapter 4 and Chapter 5). It is thus

desirable to operate the laser in a regime where a TEM_{00} spot size in the gain medium is well-matched to the laser mode and remains relatively unchanged over a range of diode currents thereby allowing a TEM_{00} -mode to lase over a wide range of thermal focal lengths in the gain medium. Achieving this results in a range of output powers that are within a viable operating regime for the laser.

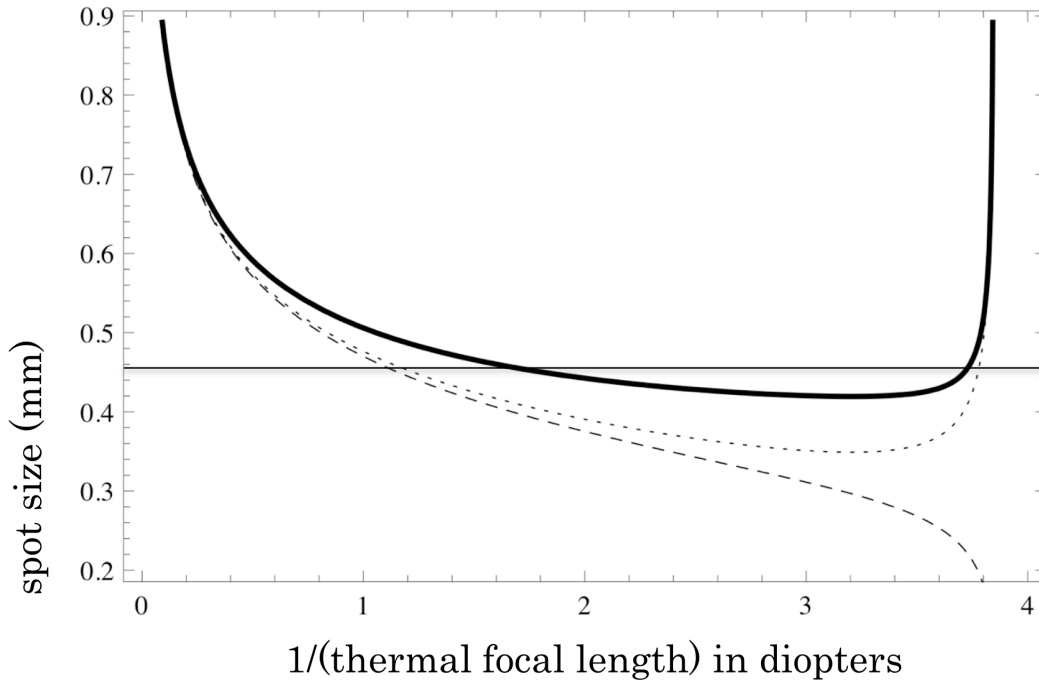


Figure 3.10 Stability curves for a 24 cm, 26 cm asymmetric cavity. The spot size (in mm) in the gain media is shown in the solid black line. The dashed (dotted) line indicates the spot size at the end of the longer (shorter) arm. The horizontal line at 450 microns indicates the mode size required to obtain TEM_{00} -mode output for a 1mm sagittal pump spotsize.

Specifically for the Nd:GdVO₄ laser oscillator which is pumped by two 40W diode lasers, an asymmetric cavity with arms of 24 cm and 26 cm is optimal. Figure 3.10 displays a stability curve showing the spotsize in the gain media with a solid black line as a function of $1/f_T$ (the focal power of the thermal lens). The dotted line indicates the spot size at the flat on the short end of the cavity while the dashed line indicates the spot size at the flat at the other end of the cavity. Notice the spot size at the end of the longer arm is smaller than that of the other side – as expected for operation in the first stability region. This feature will be useful for mode locking with a saturable Bragg reflector because this element, as will be discussed shortly, has an intensity dependent performance and thus small incident laser spot sizes are generally desirable.

Mode locking using an SBR also has pulse energy requirements (see Chapter 4); specifically, a saturation fluence for the SBR mode locking element. To allow the required intracavity pulse energy for mode locking with an SBR the cavity length may be increased, since the pulse energy is proportional to (repetition rate)⁻¹. A simple method of achieving this is to insert a telescope with a magnification of one. This extension does not change the spot size in the gain media or on any of the end mirrors and thereby allows for a increase in the pulse energy without changing other desirable cavity characteristics. Of course, the introduction of additional

optical elements can increase the cavity losses. However, this is minimal when high quality high reflectors are employed.

A power curve for the asymmetric laser resonator with 10% output coupling, corresponding to the stability curves in Figure 3.11 (with a telescopic extension making the total cavity length 2.0m) is shown in Figure 3.12. Clearly, this oscillator is capable of running nicely at ~6W of out power which corresponds to 80nJ output and 0.8 μ J inside the cavity. In Chapter 5, it will be demonstrated that this resonator meets all of the requirements for mode successful mode locking.

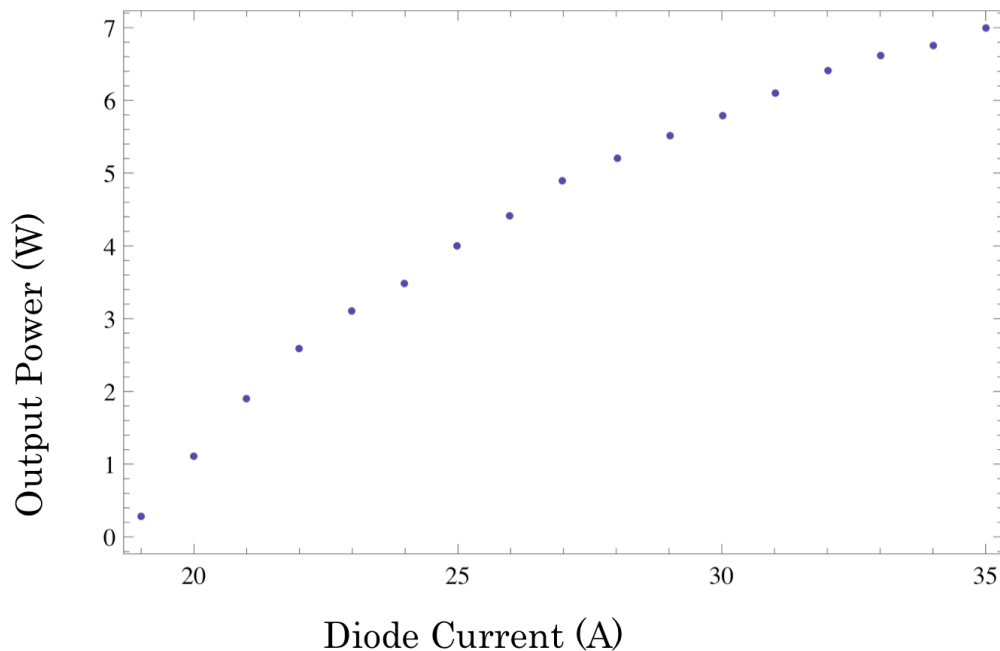


Figure 3.11 Output power (W) as a function of diode current.

4. MODE LOCKING BASICS

4.1 Introduction

In its most simple form, a laser consists of a gain medium and two mirrors. Population inversion, a prerequisite of stimulated emission, occurs in the gain media. One of the two mirrors is a high reflector with over 99% reflectivity while the other is only partially reflective to provide the output from the laser resonator. This simple laser cavity is often called a Fabry-Perot laser cavity. The two end mirrors act as nodes for the radiation within the cavity. While, the cavity can theoretically support infinitely many longitudinal modes having an integer number of half-waves, the reality is that each of these longitudinal modes has a specified frequency and only those frequencies that are also supported (i.e., above the loss line) by the gain medium bandwidth persist. The spacing between these surviving axial modes, an equivalent term for longitudinal mode, is given by $\frac{c}{2L}$ where L is the optical cavity length and c is the speed of light.

Generally speaking, these axial modes will have random phase relationships to one another and thus the intensity within the cavity, given by the square of the superposition of all the electric fields, has random fluctuations as illustrated at the top of Figure 4.1. If, however, an absolute phase relationship between these modes is created, the fields will

constructively interfere at a specific place (or time) and the result is a single pulse oscillating in the cavity as illustrated in bottom of Figure 4.1 -- the laser is then said to be continuous wave (CW) mode locked.

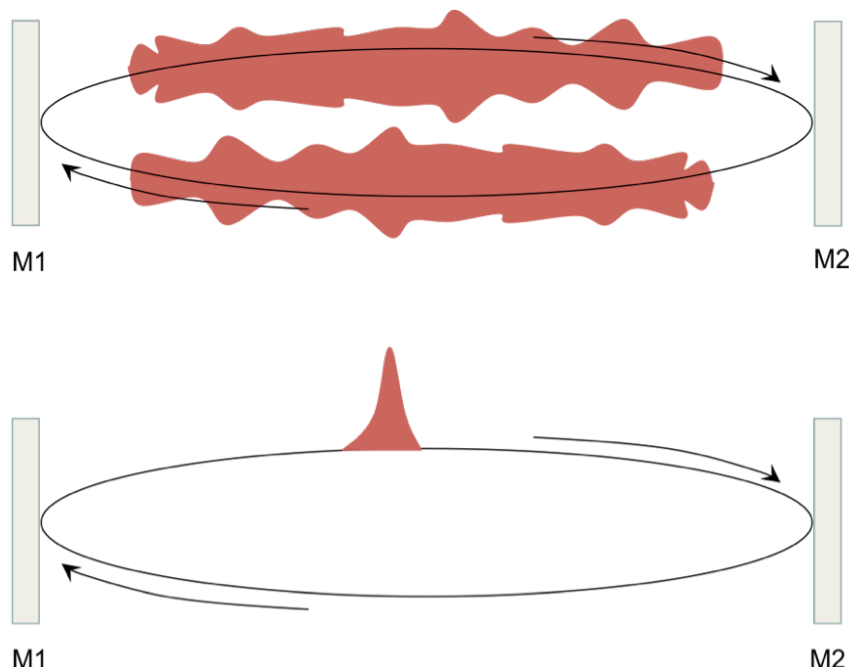


Figure 4.1: The top figure illustrates the sum of the randomly phased electric field within a laser. The bottom figure shows the pulse that results from creating an absolute phase relationship between the axial modes.

There are many methods of mode locking a laser and, for any given situation, the most appropriate one is determined by both the desired end-use of the laser system as well as the characteristics of the laser itself. This chapter contains a qualitative frequency description of CW mode locking in

section 4.2, followed by two quantitative treatments of active CW mode locking; section 4.3A describes mode locking from the time and frequency domain and section 4.3B describes the process from a mode coupling perspective. A particularly common method of mode locking ultrafast, solid-state lasers using a saturable Bragg reflector (SBR) will be described section 4.4 while section 4.5 discusses nonlinear mirror mode locking (NLM), the concepts of which are important to this thesis. This lays the groundwork for Chapter 5 where I describe a novel, dual-passive, technique for mode locking lasers. I will describe both the theory and the results of this technique and go on to show why it is particularly useful for high powered (>5W) laser oscillators.

4.2 Qualitative Frequency Description of Continuous Wave Mode Locking

Imagine a modulator is placed inside a cavity and driven at frequency ω_m which has one modulation zero per round-trip frequency of the laser pulse $\left(2\pi\left(\frac{c}{2L}\right)\right)$. The electric field inside the cavity will now experience losses and be weakened except for the one moment per cycle when the modulator is ‘off’. As a laser is an optical feedback system, the more intense the electric field, the more energy it extracts from the laser crystal and as a result it grows

even more intense. After many such roundtrips, a single pulse evolving in time is generated. An equivalent description given in the frequency domain says that the fundamental oscillating frequency with $\omega_q = 2\pi \frac{c}{2L}$ will acquire n modulation sidebands at $\omega_q \pm n\omega_m$. Since ω_m is chosen to be equal to ω_q , these modulation sidebands fall on top of the neighboring axial modes and the end result is that the modes are phase-locked and thus the laser is said to be ‘mode locked’. This type of mode locking where the pulses are formed by externally driving an amplitude modulator is called ‘active mode locking’.

Of course, the portion of the pulse that occurs at the peak of the modulation transmission experiences the highest gain and thus the pulse will continue to be shortened and to acquire sidebands until it becomes very short compared to the modulation period. This process is limited by the gain bandwidth; when the newly generated modulation sidebands fall outside of the net amplification bandwidth (gain minus loss) of the laser resonator, their oscillation cannot be supported. As a result, the pulse is not further shortened. This gain limiting effect occurs regardless of the specifics of the mode locking element.

Passive cavity elements, those for which the modulation is not externally driven, can also result in mode locking. Passive amplitude modulators often have an intensity or fluence dependent reflection or transmission such that more energy is absorbed from the cavity when the power is low. This absorption decreases and eventually saturates as the laser

intensity grows. In this situation, particular strong noise spikes experience less loss than lower intensity portions of the field and grow exponentially. Eventually a single spike will win, take all the gain, and a single pulse will be formed. In the case of passive mode locking, the modulation is of course always exactly timed to the round trip cavity time and occurs extremely fast compared to the round trip time of the pulse, T_R , (although it may be fast or slow compared to the recovery time of the absorber which is generally much shorter than T_R). As a result, the mode-locked pulse duration limit is shorter when using a passive modulation element than it is when using one that is active. A commonly used passive mode-locking mechanism is an intensity/fluence dependent mirror or SBR as will be discussed later in section 4.4. This method has been used to mode lock many laser oscillators including a 60W thin-disk Yb:YAG laser [26], a 20W side-pumped [27], a 23.5W end-pumped Yb:YAG laser [28], a multi-head 27W Nd:YAG laser [29], and a 5.4 W Nd:GdVO₄ laser [30].

Amplitude modulation is not the only mechanism by which a passive mode locking element can function. It is also possible for a passive element to lock together the phases of the modes within an oscillator by generating new frequencies which leads to each oscillating longitudinal mode acquiring sidebands at $\omega_q \pm \omega_{q+1}$. These sidebands overlap the other axial modes and result in the coupling of the axial modes or mode locking. Second harmonic generators used in nonlinear mirror (NLM) mode locking, which will be

discussed in section 4.5, function in this manner [74, 75]; over 5W has been generated from a NLM mode locked Nd:YVO₄ laser [76].

Even though certain mode locking elements function by primarily affecting the amplitude of the laser pulse while others generate additional frequencies, both the time and the frequency domain are equally valid domains from which to describe any mode locking process.

4.3 Active Mode Locking Analysis

Anthony Siegman has written the quintessential analytical description of active mode locking [6]. His descriptions are a culmination of decades of laser research. As a result, it is this analysis that is presented in sections 4.3.A and 4.3.B. Additionally, it is worth noting, the transient build-up period for a passively mode locked laser is very difficult to describe mathematically because of the inherent chaos involved. There has been no definitive description made in the literature. As such, this thesis will follow the example of many laser texts and only quantitatively describe the transient build-up for active mode locking. This description is still useful in guiding our intuition about passive mode locking and will have to suffice until a more pedagogical description is available.

4.3.1 Time and Frequency Domain

One mathematical description of mode locking from a time and frequency domain follows the signal field $E(t)$ through one round trip in the oscillator. Mode locking can be thought of as two distinct processes: 1) the transient build up of the pulse and 2) the steady-state form of the re-circulating pulse. For the moment, consider a pulse circulating in an actively mode locked laser resonator.

If the pulse is described by a Gaussian envelope,

$E(t) = E_0 \text{Exp}[-\Gamma t^2 + i\omega_o t]$, then it has a Gaussian frequency spectrum given by

$$E(\omega) = \text{Exp}\left[-\frac{(\omega - \omega_o)^2}{4\Gamma}\right] \text{ where } \Gamma = \alpha - i\beta \text{ and is termed the Gaussian pulse}$$

parameter. As the pulse passes through the gain medium, its spectrum is affected. To deal with this properly, it is necessary to transform from the time description to the frequency description $\tilde{E}(\omega) = \tilde{g}(\omega)\tilde{E}(\omega)$ where \tilde{g} is the transfer function that includes effects from all elements in the cavity. It is

$$\text{given by } \tilde{g}(\omega) = \text{Exp}\left[\frac{\alpha_m p_m}{1 + 2i \frac{(\omega - \omega_a)}{\Delta\omega_a}} - i \frac{\omega p}{c}\right] \text{ where } \alpha_m p_m \text{ is the roundtrip}$$

amplitude gain coefficient, $\Delta\omega_a$ is the gain linewidth with ω_a at its center, p

is the optical path length of the cavity, and $\frac{\omega p}{c}$ is the roundtrip phase shift of

the cavity. Since the mode locked frequencies can only be those that are both within the gain linewidth and also above the loss line, $\Delta\omega_a \gg \omega - \omega_a$ and the following Taylor series expansion is allowed :

$$\tilde{g}(\omega) \approx \text{Exp} \left[\alpha_m p_m \left(1 - 2i \frac{(\omega - \omega_a)}{\Delta\omega_a} - 4 \frac{(\omega - \omega_a)^2}{\Delta\omega_a^2} \right) - i \frac{\omega p}{c} \right]. \text{ The total linear phase}$$

shift in ω is expressed by the terms $\frac{\omega p}{c} + \frac{2\alpha_m p_m \omega}{\Delta\omega_a}$. Rewriting this using

$$\omega_{ax} = \frac{2\pi c}{p}, \text{ the axial mode spacing, results in } \frac{\omega p}{c} \left[1 + \frac{\omega_{ax}}{\Delta\omega_a} \frac{\alpha_m p_m}{\pi} \right]. \text{ A linear}$$

phase shift leads to a time delay in the time domain description $t - T = T'$, which is an increased roundtrip time or an increased roundtrip optical

distance. $\frac{T' - T}{T} \approx \frac{p' - p}{p} \approx \frac{\omega_{ax}}{\Delta\omega_a} \frac{\alpha_m p_m}{\pi}$. Note that this shift is very small. In

fact, for a typical diode pumped solid-state laser (DPSS) which may have 500-1000 axial modes and an $\alpha_m p_m = 0.2$, the frequency shift is 1 in 10,000. Thus, in the steady state, it is safe to assume a pulse circulating in the cavity will return to exactly the same position each successive trip.

Conveniently, multiplying the Gaussian pulse spectrum by the expansion of the gain function results in a new Gaussian pulse spectrum with new Gaussian parameter Γ' :

$$\text{Exp} \left[-\frac{(\omega - \omega_o)^2}{4\Gamma} \right] \text{Exp} \left[-\frac{4\alpha_m p_m}{\Delta\omega_a^2} (\omega - \omega_o)^2 \right] = \text{Exp} \left[-\frac{(\omega - \omega_o)^2}{4\Gamma'} \right] \quad (4.1)$$

This says that the change in the pulse after passing through the gain

medium is given by $\Gamma' - \Gamma \approx \frac{16\alpha_m p_m}{\Delta\omega_a^2} \Gamma^2$. In general, $\alpha_m p_m \ll 1$ and

$\omega - \omega_o \ll \Delta\omega_a$. Thus, spectral narrowing of the pulse occurs.

A pulse propagating through an amplitude modulator (AM) will have a net amplitude described by $E''(t) = \tilde{t}_m(t)E'(t)$ where $\tilde{t}_m(t)$, a time-varying transmission function, may be written as

$$\tilde{t}_m(t) = \text{Exp}\left[-\Delta_m(1 - \text{Cos}[\omega_m t])\right] \approx \text{Exp}\left[-\frac{\Delta_m \omega_m^2}{2} t^2\right]. \quad (4.2)$$

Here ω_m is the modulation frequency which is some integer multiple of the axial mode spacing, and $2\Delta_m$ is the peak-to-peak amplitude of the AM. The Gaussian pulse parameter Γ'' after passing through the modulator will be given by $\text{Exp}[-\Gamma t^2] \text{Exp}\left[-\frac{\Delta_m \omega_m^2}{2} t^2\right] = \text{Exp}[-\Gamma'' t^2]$ and $\Gamma'' - \Gamma \approx \frac{\Delta_m \omega_m^2}{2}$. Thus, pulse narrowing (or spectral broadening) occurs when a pulse transverses an AM.

A pulse propagating through a frequency modulator (FM) has a complex transmission function given by:

$$\tilde{t}_{FM}(t) = \text{Exp}[i\Delta_m \text{Cos}\omega_m t] \approx \text{Exp}\left[\pm i\Delta_m \left(1 - \frac{\Delta_m \omega_m^2}{2} t^2\right)\right]. \quad (4.3)$$

The static portion of the phase shift can be absorbed into a very small change in the length of the laser cavity while the quadratic portion generates a small

chirp on the pulse $\Gamma'' - \Gamma' \approx \pm i \frac{\Delta_m \omega_a^2}{2}$.

As the total change in the Gaussian parameter for a single cavity round trip is zero, the steady-state Gaussian parameter can be solved for.

$$\Gamma'' - \Gamma \approx \frac{16\alpha_m p_m}{\Delta\omega_a^2} \Gamma^2 + \left\{ \frac{1}{\pm i} \right\} \frac{\Delta_m \omega_m^2}{2} = 0 \quad (4.4a)$$

$$\Rightarrow \Gamma_{ss} = \left\{ \frac{1}{\pm i} \right\}^{\frac{1}{2}} \left(\frac{\Delta_m}{\alpha_m p_m} \right)^{\frac{1}{2}} \frac{\omega_m \Delta\omega_a}{4\sqrt{2}} \equiv \alpha_{ss} - i\beta_{ss} \quad (4.4b)$$

Since \sqrt{i} has a phase angle of 45° and a magnitude of $\frac{1}{\sqrt{2}}$, note that the only

difference between the AM and FM cases is that the steady state Gaussian

parameter is purely real for AM $\left(\alpha_{ss,AM} = \left(\frac{\Delta_m}{\alpha_m p_m} \right)^{\frac{1}{2}} \frac{\omega_m \omega_a}{4\sqrt{2}} \right)$ and is complex for

the FM case $\left(\beta_{ss,FM} = \frac{\alpha_{ss,AM}}{\sqrt{2}} \right)$.

The FWHM pulse in an AM mode locked laser is given by

$$\tau_p \approx \left(\frac{2\sqrt{2}\ln 2}{\pi^2} \right)^{1/2} \left(\frac{\alpha_m p_m}{\Delta_m} \right)^{1/4} \left(\frac{1}{f_m \Delta f_a} \right)^{1/2} \text{ where } f_m \text{ is the frequency modulation in}$$

hertz and $\frac{\Delta f_a}{2\pi}$ is the gain linewidth also in Hz. Since the saturated round

trip gain coefficient $(\alpha_m p_m)$ varies from 0.1 – 1.0 and Δ_m also varies from 0.1 –

1.0, the pulse duration has the strongest dependence on $\left(\frac{1}{f_m \Delta f_a} \right)^{\frac{1}{2}}$.

Furthermore, this predicts that an actively mode locked laser oscillating in

just a few axial modes will behave much differently than actively mode

locked lasers that oscillate more or less across the full range of possible

longitudinal modes. In this second case, the spectral narrowing that occurs from the pulse passing through the gain medium must be balanced by the spectral broadening produced by the pulse transversing the AM. Since the centermost axial modes see more gain and the wings see less, this balance is accomplished by a transferring of energy from the center modes to those in the wings by the AM.

The FM mode locked laser functions in the same manner as the AM case with the addition of a small frequency chirp that is equal in magnitude to the pulse width modulation. As a result, the time-bandwidth product will be increased by $\sqrt{2}$. Conceptually, this increase in pulse duration can be understood by considering modulating the end mirror back and forth with its position given by $x(t) = x_m \cos \omega_m t$. The moving mirror causes the pulse to experience a small doppler shift. All of these small shifts accumulate until the signal's frequency goes outside of the gain curve. This doesn't happen to the pulse when it strikes the mirror at either extrema of motion or at the turning points. In this case there will be no Doppler effect on the pulse, just a small frequency chirp which actually broadens the spectrum. The steady state mode locking occurs when the frequency chirp balances the Doppler shift.

4.3.2 Mode Coupling Analysis

While the time-domain analysis of mode locking tracks the electric field through cavity round trips, the frequency-domain analysis deals with the coupling between the axial modes. This analysis is more formal than that of the time-domain and is capable of handling more complex situations. In fact, much of the current mode-locking literature begins with this analysis [16, 41 42, 47, 74, 75, 77, 78, 79, 80].

The electric field inside a laser cavity can be expressed as a sum of the axial modes $E(r,t) = \sum_n \tilde{E}_n(t) e^{i\omega_n t} u_n(r)$ where $\tilde{E}_n(t)$ is the complex phasor of the n^{th} axial mode in the slowly varying envelope approximation (the temporal and spatial variations of the pulse envelope are small compared to those of the wavelength) and the frequencies, ω_n , are carefully defined and do not take into account any dispersive effects which will be added later. The axial modes are labeled by the number q where q_0 is the frequency of the center line; $\omega_q = \omega_{q_0} + q\omega_{axial}$. These ω_q 's are not the actual modes oscillating in an actively mode-coupled laser with a modulator being run at ω_m , but rather are the cavity resonances. The modes that exist in the cavity will be labeled by n and are the result of the modulated frequency and its associated sidebands; defined as $\omega_n = \omega_0 + n\omega_m$. In general, ω_m , the modulation frequency, and ω_{axial}

$\left(\omega_{axial} = \frac{2\pi c}{p} \right)$ will be very close to one another, but it can be useful to define

the detuning that occurs between the axial resonance spacing and the modulation frequency as $\omega_d = \omega_m - \omega_{axial}$.

In the slowly-varying envelope approximation the cavity equation describing the evaluation of the complex phasors can be written as

$$\frac{d\tilde{E}_n}{dt} + \left[\frac{\gamma_{c,n}}{2} + i(\omega_n - \omega_q) \right] \tilde{E}_n = i \frac{\omega}{2\varepsilon} \tilde{P}_n \quad \text{where } \gamma_{c,n} \text{ is the total cavity decay rate for}$$

the n -th axial mode and \tilde{P}_n is the component of the polarization that matches up in frequency and spatial variation with the n -th cavity mode. \tilde{P}_n can be conveniently represented by a sum of three terms: (i) the linear polarization due to laser medium (ii) the nonlinear polarization due to nonlinear elements and (iii) any polarization that results from the mode locking action. The linear term can be written as $\tilde{P}_n = (\chi_n + i\chi'_n)\varepsilon\tilde{E}_n$. The particulars of the nonlinear situation will dictate how the second term is written. For example, a term resulting from the second harmonic will be proportional to the square of the electric field while the term resulting from self-phase modulation will depend on the cube of the electric field. The modulation polarization term for the cases of amplitude and frequency modulators will be determined separately in the following two paragraphs.

Consider an amplitude modulator with a time varying transmission function,

$$\tilde{t}_m(t) = \text{Exp}\left[-\Delta_m(1 - \text{Cos}[\omega_m t])\right] \approx 1 - \Delta_m + \Delta_m \text{Cos}\omega_m t, \quad (4.5)$$

where, as before, $2\Delta_m$ is the peak to peak variation in transmission. The outcome of an impinging sine wave field in this analysis is represented as:

$$\tilde{t}(t) \times \tilde{E}_n e^{i\omega_n t} \approx (1 - \Delta_m) \tilde{E}_n e^{i\omega_n t} + \frac{\Delta_m \tilde{E}_n}{2} \left[e^{i(\omega_n + \omega_m)t} + e^{i(\omega_n - \omega_m)t} \right]. \quad (4.6)$$

It can be seen by writing the cosine term using Euler's formula, that the modulator attenuates the input wave by a factor of $(1 - \Delta_m)$ and creates two sidebands of half the amplitude at $\omega_n \pm \omega_m$.

In the case of frequency modulation, the transmission function is given by $\tilde{t}_m(t) = \text{Exp}[i\Delta_m \text{Cos}\omega_m t] \approx 1 + i\frac{\Delta_m}{2} + [e^{i\omega_m t} + e^{-i\omega_m t}]$ and once again two sidebands are created at $\omega_n \pm \omega_m$.

Knowing that each sideband will, upon multiple passes acquire their own sidebands, we can write the final cavity coupled equation (and starting point for many theory papers) as:

$$\frac{d\tilde{E}_n}{dt} + \left[\left(\frac{\gamma_{c,n}}{2} - \frac{\omega\chi_n''}{2} \right) + i \left(\omega_n - \omega_q + \frac{\omega\chi_n'}{2} \right) \right] \tilde{E}_n = \left\{ \begin{matrix} 1 \\ i \end{matrix} \right\} \left(\frac{\Delta_m}{2T} \right) [\tilde{E}_{n+1} + \tilde{E}_{n-1}]. \quad (4.7)$$

The left hand side terms include the laser gain, the loss, the detuning, and dispersive effects for each mode. The right hand side contains the mode-coupling by the AM (real term) or FM (imaginary term) to the $n + 1$ and $n - 1$ axial modes.

4.4 Mode Locking with a Saturable Bragg Reflector

A saturable Bragg reflector, the design of which will be discussed with more detail in section 4.4.1, is most notably differentiated from standard (laser) mirrors by having an intensity/fluence dependent reflectivity. This means that incident laser pulses having higher energy fluence/intensity experience a higher reflectivity than those having lower values. This characteristic makes SBRs useful passive mode locking elements [26-30, 32, 33]. Furthermore, bandgap engineering and semiconductor growth techniques allow the quantum wells to be tailored to suit particular wavelengths between 800 and 2400 nm [19] and the change in reflectivity associated with a saturated quantum well transition can be also tuned to accommodate a wide variety of lasers. For instance, 110 fs Ti:sapphire laser at $\lambda \approx 800\text{nm}$ [38], a 220 fs Nd:glass laser at $\lambda \approx 1064\text{nm}$ [39], and a 160 fs Cr:LiSAF laser at $\lambda \approx 800\text{nm}$ [39] have all been mode locked with the assistance of an SBR. A multiple quantum well SBR has been used to mode lock a Nd:YLF at $\lambda \approx 1050\text{nm}$ [34] and Yb:YAG at $\lambda \approx 1030\text{nm}$ [35] oscillators. SBRs are also useful in mode locking microchip lasers as evidenced by a Cr⁴⁺ co-doped Nd:YAG at $\lambda = 1064\text{nm}$, 290 ps laser [36]. The physical design of a generic SBR is described in section 4.4A, while Section 4.4B discusses mode locking with an SBR.

4.4.1 Saturable Bragg Reflector Design

Saturable Bragg reflectors are comprised of one or more quantum well saturable absorbers on top of a Bragg stack that is grown on a substrate as shown in Figure 4.2. Transitions in the quantum well(s), commonly made of InGaAs on GaAs, allow electrons to be promoted from the confined heavy hole/light hole quantum state to the conduction band by the absorption of incoming radiation of the appropriate energy. When approximately half of the carriers are excited, the laser is operating with an energy fluence equal to the saturation fluence of the absorber and the quantum well is more transparent to the incoming radiation – the absorption is partially “bleached”. That is to say, the radiation passes through the quantum well with less attenuation so that overall more of the incident radiation is reflected by the Bragg stack. The Bragg stack consists of alternating layers of high and low indices of refraction (often GaAs/AlAs) each having a thickness of $\lambda/4$ – the standard geometry for a highly reflective dielectric stack. As a result, the reflections from the front and back of each layer all add together in phase and the result is a highly reflective mirror. Of course, the excited carriers have an upperstate lifetime and eventually relax back into their ground state. At this point, the percent of the incident radiation absorbed by the quantum well again increases and the overall reflectivity of the SBR decreases back to its initial value.

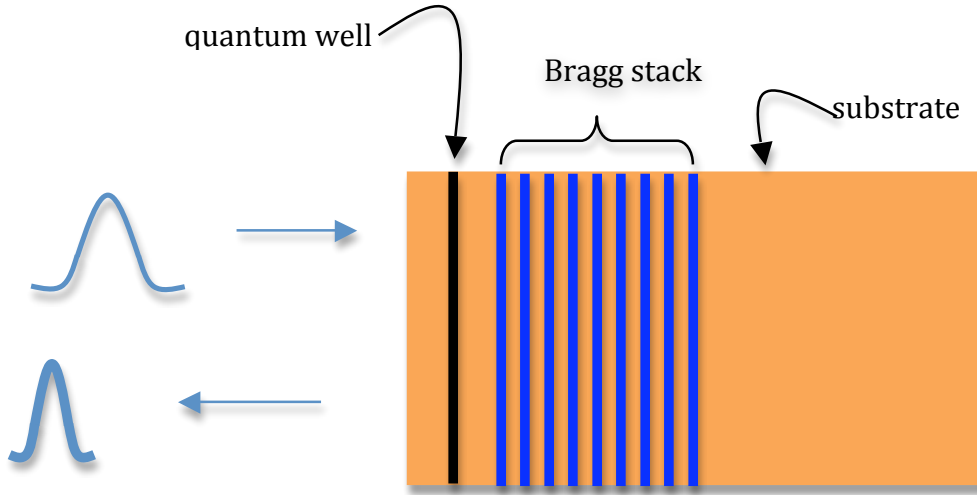


Figure 4.2. Anatomy of a saturable Bragg reflector (SBR). The quantum well saturable absorber is shown in black and the Bragg stack is the alternating blue and gold region.

A SBR is clearly a nonlinear device; in the limit when $\tau_{pulse} \ll \tau_R$, its absorption depends purely on the incoming pulse's time-integrated intensity or pulse fluence, $F_p(t) = \int_{-\infty}^t I(t') dt'$. The absorption of the SBR as a function of time is then given by $\alpha(F) = \frac{\alpha_0}{1 + F/F_{sat}}$ where α_0 is the small signal absorption, F_{sat} is the saturation fluence, a material-dependant parameter with a typical value of $50 \mu\text{J}/\text{cm}^2$ [21]. The resultant change in reflectivity, ΔR , is called the modulation depth and is equal to the small signal absorption minus the non-saturable absorption that results from the background absorption and the

defects in the crystal – the latter are actually required to achieve fast relaxation times [21].

4.4.2 Saturable Bragg Reflector Mode Locking

In the literature, slow saturable absorbers have recovery times, τ_A , that are much slower than the final pulse duration, τ_p , while fast saturable absorbers operate in the regime of $\tau_A \ll \tau_p$ [77, 81, 82]. It has been shown that fast and slow SBRs of the same modulation depth can produce almost equally short pulses as long as the recovery lifetime of the SBR is no more than a factor of ten slower than the pulse width [77]; a result that is not surprising given that all fast absorbers eventually becomes slow if the pulse duration becomes short enough. This thesis is concerned with solid-state lasers which have relatively long upperstate lifetimes ($\tau_{upperstate, NdGdVO_4} \sim 90\mu s$ [82]) and as result no appreciable dynamic gain saturation is taking place. As such, it is acceptable to treat the SBR as a fast absorber (the “fast” element in the cavity) even though the resulting pulse duration is on the order of the recovery time of the absorber [37].

Haus’s master mode locking equation for mode locking with an absorber [81], which is shown below and assumes that linear and nonlinear

changes to the pulse are small for each round trip, describes the mode locking dynamics in a laser cavity:

$$T_R \frac{\partial}{\partial T} A(T, t) = \left(-iD \frac{\partial^2}{\partial t^2} + i\delta |A|^2 \right) A + (g - l + D_{g,f} - q(T, t)A). \quad (4.8)$$

Here, $A(T, t)$ is the slowly varying field envelop of the pulse which evolves slowly over many round trips. As such, the time variable T is used to describe the long-term time variation in the pulse envelope as it moves towards the steady state. The round-trip cavity time is given by T_R while D is the intra-cavity group delay dispersion (also commonly abbreviated as GDD = $-\frac{\lambda}{c} \frac{d^2 n}{d\lambda^2}$), $D_{g,f} = \frac{g}{\Omega_g^2} + \frac{1}{\Omega_f^2}$ is the gain and possible filter dispersion, where g is the saturated gain, Ω_g is the half-width at half-maximum (HWHM) of the gain bandwidth and Ω_f is the half-width at half-maximum (HWHM) of the filter bandwidth. The self phase modulation coefficient is given by ,

$$\delta = \left(\frac{2\pi n_2}{\lambda A_{eff}} \right) L, \text{ where } A_{eff} \text{ is the area of the mode in the crystal of length } L.$$

No analytical solutions are known to this master equation, however if the dissipative terms due to gain and loss are ignored, the master equation reduces to the nonlinear Schrödinger equation which, for negative GDD, has the following soliton solution $A(T, t) = A_0 \text{sech}[x(T, t)] e^{i\theta}$ where x is the retarded

time normalized to the soliton width τ (the full-width half-maximum (FWHM) of the soliton is given by $\tau_{\text{FWHM}} = 1.76 \tau$), and θ is a phase factor [1,3].

Assuming that the gain is saturated to its stationary power, then

$$g(T) = \frac{g_0}{1 + \frac{E_p(T)}{P_L T_R}}, \text{ where } g_0 \text{ is the small signal gain, } P_L \text{ is the saturation power}$$

of the gain medium, $P_L = I_{\text{sat}} A_{\text{eff}} = \frac{\hbar \omega}{\sigma_{\text{em}} \tau_P} A_{\text{eff}}$, and the pulse energy is defined as

$$E_p(T) = \int_{-\infty}^{\infty} |A(T, t)|^2 dt.$$

The response of the saturable absorber on the

instantaneous pulse power each round trip is given, for the case of the fast

$$\text{saturable absorber, as } q(T, t) = \frac{q_0}{1 + \frac{|A(T, t)|^2}{P_A}} \text{ (N.B. this is effectively } \alpha = \frac{\alpha_0}{1 + \frac{I}{I_{\text{sat}}}} \text{)}$$

where q_0 is the non-saturated, saturable loss of the absorber. The response of

the slow saturable absorber with saturation energy E_A , which is assumed to

$$\text{saturate, is given by the relationship } \frac{dq(T, t)}{dt} = -\frac{q - q_0}{\tau_A} - q \frac{|A(T, t)|^2}{E_A}.$$

When the

recovery time of the absorber is much faster than the pulse duration, it is the intensity of the laser beam that drives the absorber dynamic. Once, however,

the laser pulse is formed, it is the energy fluence that generally provides

pulse shortening and stability to the mode locking [37].

The master equation can be written as a set of three rate equations

[47, 82] by assuming the absorber dynamics are by far the fastest dynamics

in the system and that all the changes occurring on each round-trip are small. The coupled rate equations describing the mode locking are then:

$$1. \quad T_R \frac{dP}{dt} = (g - l - \alpha)P \quad (4.9a)$$

$$2. \quad T_R \frac{dg}{dt} = -\frac{g - g_0}{T_L} - \frac{gT_R P}{E_L} \quad (4.9b)$$

$$3. \quad T_R \frac{dq}{dt} = -\frac{q - q_0}{T_A} - \frac{\alpha T_{RP}}{E_A} \quad (4.9c)$$

where P is the laser power, g is the gain per round trip, l is the linear loss per round trip, q is the sum of saturable loss per round trip, q_0 the unsaturated absorber loss per round trip, and g_0 is the small-signal gain per round trip. The parameters T_L and T_A are, respectively, the upper-state lifetime of gain medium and the absorber recovery time normalized to the round trip cavity time, $T_L = \frac{\tau_L}{T_R}$ and $T_A = \frac{\tau_A}{T_R}$. The saturation energies for the gain media and

the absorber are given, respectively, by $E_L = \frac{h\nu A_{eff,L}}{2\sigma_L}$ and $E_A = \frac{h\nu A_{eff,A}}{2\sigma_A}$ where

σ_L and σ_A are the gain and absorption cross-sections in the gain media and absorber, respectively, and the factor of 2 comes from averaging the standing-wave effects in a Fabry-Perot laser cavity [47].

In the limit of a single mode laser running CW, the saturable

absorption term can be written as $q = \frac{q_0}{1 + P/P_A}$ where $P_A = \frac{E_A}{\tau_A}$, the saturation

power of the absorber [47]. Equations 4.5a) and 4.5b) give the criteria for

$$\text{CW mode locking with no Q-switching } -2P \frac{dq}{dP} \bigg|_{CW} < \frac{1 + \frac{P}{E_L/\tau_L}}{T_L} \bigg|_{CW} \text{ where } 1 + \frac{P}{E_L/\tau_L}$$

describes how many times above the lasers gain saturation the laser is operating and E_L/τ_L is the saturation power of the laser. The right hand side of the inequality is the relaxation rate. The left hand side of the inequality is the decay time of a power fluctuation of the laser for fixed gain. As a result, the inequality states that if the gain cannot respond quickly enough to the fluctuation in laser power, the relaxation oscillations will grow into a Q-switched pulse and Q-switched mode locking (QML) results [47]. This of course is an undesirable result for this thesis; CW mode locking with a single pulse in the cavity is the desired result.

Hönninger et al. [16] further simplify and experimentally verify the stability criterion for stable CW mode locking with no QML. They rewrite the pulse loss per cavity round trip as:

$$\alpha_p(E_p) = \alpha_0 \frac{F_{sat,A} A_{eff,A}}{E_p} \left(1 - \exp \left(- \frac{E_p}{F_{sat,A} A_{eff,A}} \right) \right). \quad (4.10)$$

This assumes that (i) the pulse duration of the mode locked pulse is on the order of or shorter than the recovery time of the absorber and (ii) the recovery time of the absorber is shorter than the cavity round trip time ($\tau_p \leq \tau_A \ll T_R$).

These conditions ensure the absorber has fully recovered between pulses and are compatible with the lasers presented in this thesis.

Expression 4.10 can be substituted in to the three coupled mode locking equations 4.9a – 4.9c which are then linearized for small deviations δE_p and δg from the steady state values, \bar{E}_p and \bar{g} . This procedure results in the following stability criterion [16]:

$$E_p \left| \frac{dq_p}{dE_p} \right|_{\bar{E}_p} < \frac{T_R}{\tau_L} \left(1 + \frac{P}{P_{sat,L}} \right) = \frac{T_R}{\tau_L} + \frac{E_p}{E_{sat,L}}. \quad (4.11)$$

Small increases in pulse energy grow exponentially because the absorption of the absorber becomes more and mode bleached. In order to prevent QML, this growth in pulse energy must be bounded by gain saturation.

Since the change in reflectivity of an SBR can, to some extent be custom designed, it becomes useful to write the stability condition for CW mode locking in terms of the change in saturable absorption, ΔR , as a function of the pulse energy. Taking into account that most absorbers have a ΔR of less than 10% and that the laser is operating in optimal regime of 3 to 5

times the fluence saturation [33], $F_{sat,A} = \frac{\hbar\omega}{\sigma_A}$, the change in reflectivity can be

written as $\Delta R_{SBR} = \Delta R_{NS} + \frac{\Delta R_S}{1 + \frac{F_p}{F_{sat,A}}}$ where $F_p = E_p / A_{eff,A}$, where ΔR_S and ΔR_{NS}

are the changes in reflectivity due to the saturable and the nonsaturable absorption, respectively, of the SBR. Additionally, the dependence of the stability criterion on the laser material's upperstate lifetime can be neglected

as long the laser is operating well-above threshold. Under these conditions, the simplified stability criterion is $E_p > \sqrt{E_{sat,L}, E_{sat,A} \Delta R_s}$ [16].

Traditionally, mode locking with saturable absorbers was thought to only be possible when the net gain window is short so that just the pulse is supported and the any other noise sees losses and therefore dies out. In the late-1980's and the early-1990's soliton mode locking became understood [32, 33, 41, 83 84]. In this technique, a balance is struck between negative group delay dispersion (GDD) which tries to pull the pulse apart and self-phase modulation (SPM) which is acting to focus the pulse; thus pulse stability is maintained. Some of these soliton mode locking schemes employ SBRs with a reduced loss window that is considerably longer than that of the pulse [41, 83, 84]. In these cases, the SBR is not starting the mode locking nor is providing much pulse shaping, but it is adding significant stability to the mode locking.

4.5 Mode Locking with a Nonlinear Mirror

Another passive mode locking technique that functions primarily by generating additional spectral components and secondarily with some amplitude modulation was developed by Stankov et al. and published in 1991 [74, 75]. This method uses a 'nonlinear mirror' which is shown in Figure 4.3

and is comprised of a second harmonic generating crystal (SHG) at a certain distance from a dichroic output coupler (DOC). A DOC is partially transmissive for one wavelength (in this case, the fundamental wavelength as will be described in the following paragraph) and 100% reflective at another (in this case, the second harmonic which is also described in the next paragraph). As a similar cascaded $\chi^{(2)}:\chi^{(2)}$ process is used in the dual-passive mode locking scheme presented in Chapter 5, an overview of Stankov's nonlinear mode locking is presented here.

Before the details of nonlinear mirror mode locking are described, it is useful to have a basic understanding of second harmonic generation, also known as frequency doubling. The symmetry of some crystals results in what is known as $\chi^{(2)}$ nonlinearity. When an electromagnetic wave, the fundamental frequency, is incident on a crystal that does not have $\chi^{(2)}$ (or higher) nonlinearities, the valence electrons respond in a linear manner, i.e., the polarization is linear with the incident field ($\vec{P} \propto \vec{E}_i$), and the same fundamental frequency is radiated. If a $\chi^{(2)}$ nonlinearity is present, the electrons can be displaced in such a way that a nonlinear polarization proportional to the product of two electric fields ($\vec{P} \propto \vec{E}_i \vec{E}_j$) occurs and the sum (or difference) of these two frequencies reradiates. In the case of second harmonic generation, both of these electric fields are from the fundamental ($\vec{E}_i = \vec{E}_j$) and as result, the second harmonic (or doubled frequency) is reradiated.

Not surprisingly, the amount of doubled frequency that is generated increases with increasing fundamental intensity. Additionally, generation of the most second harmonic occurs when all the contributions from the two electric fields, $(\vec{E}_i \vec{E}_j)$, add coherently – when the frequencies are phase matched. The phase mismatch between is given by Δkl where l is the length of the nonlinear crystal and $\Delta k = 2\pi \left(2\frac{n_1}{\lambda_1} - \frac{n_2}{\lambda_2} \right) = \frac{4\pi}{\lambda_1} (n_1 - n_2)$, where n_1 is the index of refraction corresponding to the fundamental wavelength λ_1 and n_2 is the index of refraction corresponding to the second harmonic wavelength λ_2 . The phase matched condition is then $\Delta kl = \pm 2m\pi$ where m is an integer that can have values of 0,1,2,... . It is important to note that phase *mismatch* can also occur. In the case of a nonlinear mirror, Δkl is set to $\pm(2m+1)\pi$ where m is again any integer 0,1,2... When n is 0 and $\Delta kl = \pm\pi$, the second harmonic is back converted to the fundamental over the crystal length l while any residual fundamental remains relatively unaffected. For non-zero values of m , the frequency will be forward and back converted several times so the resulting emitted radiation is again the fundamental.

Figure 4.3 shows a schematic of a generic nonlinear mirror. The incoming fundamental radiation (red pulse) with bandwidth $\Delta\omega$ is shown passing through a SHG resulting in frequency doubled radiation (green) and a spectral broadening of $\sqrt{2}$. This occurs because multiplying the two fields in the time domain corresponds to a convolution (and thus a spectral

broadening) in the frequency domain. Some defined percent of the residual fundamental radiation is transmitted out of the dichroic output coupler (DOC) while the remaining fundamental and all of the frequency doubled radiation is reflected back into the laser cavity. After being reflected, the frequency doubled radiation again passes through the SHG (on its return trip). This time it is back converted into the fundamental frequency with a spectral bandwidth that is now $\sqrt{3} \Delta\omega$. Furthermore, these additional spectral bands have been locked together so that mode locking is achieved.

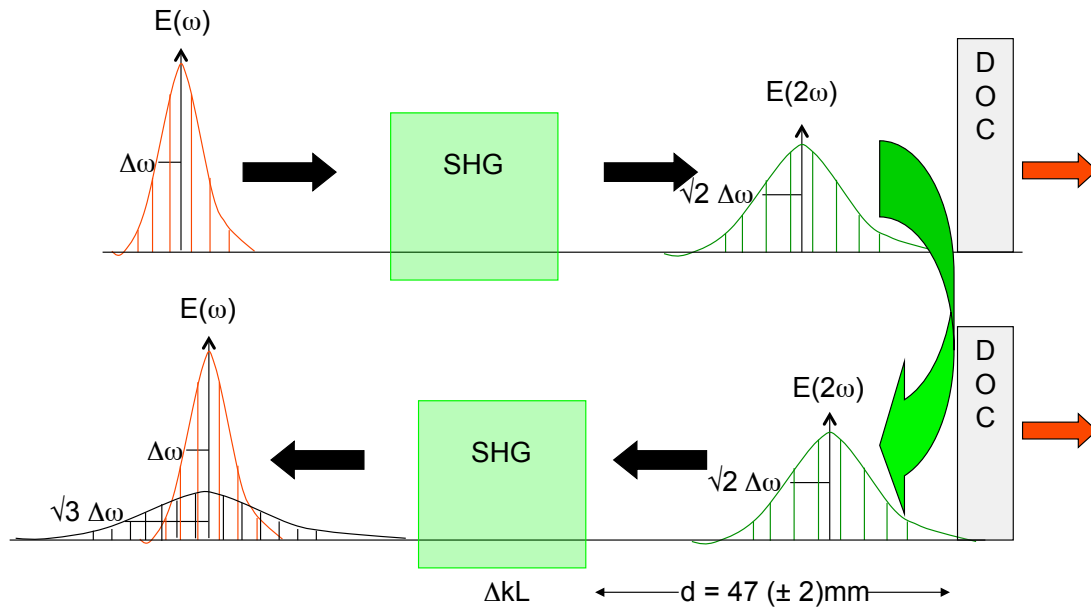


Figure 4.3: This figure shows the electric field and the axial modes of the fundamental frequencies as they propagate through the second harmonic crystal to the dichroic output coupler which transmits some specified percent of the fundamental while the fundamental and all of the doubled frequencies are reflected back through the second harmonic generator.

The higher the intensity of the fundamental, the more efficient the frequency doubling. So, since all of the green is reflected into the cavity, more generated second harmonic radiation then means more energy remains in the cavity (and is back converted to the fundamental). In this way, the DOC is providing amplitude modulation by effectively increasing the reflectivity of the cavity. It should be noted that in order to get efficient back conversion to the fundamental frequency, the distance, d , between the second harmonic and the DOC must be adjusted so the second harmonic acquires a π phase shift with respect to the fundamental which results in a complete phase mismatch and ensures it is efficiently back converted and the residual fundamental. For a nonlinear mirror operating at 1064nm (and a second harmonic of 532nm), d is roughly 3.5cm.

5. NOVEL DUAL-PASSIVE MODE LOCKING

5.1 Introduction

In the previous chapter, it was shown that in order to achieve continuous wave (CW) mode locked operation with a saturable Bragg reflector (SBR) the laser oscillator must have an intracavity pulse energy that exceeds a critical threshold energy E_c [47]. below this critical pulse energy, Q-switched mode locked (QML) operation typically occurs [85]. Q-switching is not only an undesirable end result, but it can damage the SBR [27]. Because E_c is proportional to $\sqrt{F_{L,sat.}A}$ [47, 78], where $F_{L,sat.}$ is the saturation fluence of the gain medium, this requirement poses a mode locking difficulties for lasers that employ large spatial mode areas, A , in the laser gain medium, such as the TLS Nd:GdVO₄ presented in Chapter 3.

This chapter demonstrates that the aforementioned limitation on the design of mode locking can be overcome by the insertion of a phase-mismatched SHG crystal in a laser cavity. The phase locking produced by the SPM-like effect associated with the cascaded $\chi^{(2)}:\chi^{(2)}$ process in the SHG crystal [80] assists (or stabilizes [78, 86]) the mode locking process initiated by the amplitude modulation in the SBR, thereby (i) significantly reducing the CW mode locking threshold pulse energy [86] and (ii) shortening the duration of the generated pulses [87].

The resultant solid-state, dual-passive mode locking technique is an extension of the scheme used by Agnesi *et al.* to stabilize the CW mode locking operation of Nd:BaY₂F₈ [86] – a gain medium with a small stimulated emission cross-section (and hence large $F_{L,sat.}$). Similar CW mode locking schemes employing a combination of amplitude modulation and phase locking via a second-order optical nonlinearity have been demonstrated previously. In particular, G. Cerullo *et al.* [88] achieved CW mode locked operation of a diode-pumped Nd:YAG laser by using the inherent phase-locking (i.e., SPM) of cascaded second order nonlinearities in a LiB₃O₅ (LBO) SHG crystal to also induce spatial loss modulation with an intracavity slit aperture. Earlier, a comparable technique with a phase-mismatched potassium titanyl phosphate (KTP) SHG crystal in an anti-resonant ring was employed by Carruthers and Duling [89] to CW mode locked Nd:YAG. More recently, CW mode locked operation of Nd:GdVO₄ has been attained using defocusing cascaded Kerr lensing in periodically poled KTP [90]. In a complimentary hybrid scheme, R. Wallenstein *et al.* [91] used an acousto-optic (AO) modulator and a phase-mismatched LBO crystal to generate ~10ps pulses from a diode-pumped Nd:YVO₄ laser. Furthermore, it is noted that L.J. Qian *et al.* [92] have exploited the negative nonlinear phase shift generated by a phase-mismatched LBO crystal to achieve soliton mode locking under conditions of normal group

velocity dispersion (GVD) in a semiconductor saturable-absorber-mirror-assisted Kerr-lens ML femtosecond Cr:Forsterite laser.

In this chapter, a detailed experimental study of the performance characteristics of a dual-passive CW ML scheme employing a combination of a SBR and a phase-mismatched SHG crystal is presented. This design is useful for mode locking the large mode area, high-power, TEM₀₀-mode ($M^2 < 1.2$), diode-pumped, Nd:GdVO₄ laser presented in Chapter 3. Particular attention is paid to the role of the phase-mismatch in the SHG. The resulting optimized mode locking technique for our 76MHz laser cavity generates an extremely stable and robust train of 7.6ps pulses with an average power of greater than 6W at 1063nm.

5.2 Dual-Passive Mode Locking

For mode locked operation at a 76MHz repetition rate, the slightly asymmetric 0.5m cavity shown in Figure 5.1 is extended on the short 24cm arm of the auxiliary cavity using two mirrors with radii of curvature R_1 and R_2 and a flat output coupler (OC) arranged for unity ray transformation on a round trip [93]. Values of R_1 and R_2 are chosen so that the reflective intracavity telescope has magnifications $M = R_2/R_1$ of 1.0, 1.5, and 2.0 while keeping the cavity length constant (specifically, the extension length $sR_1 + R_2$

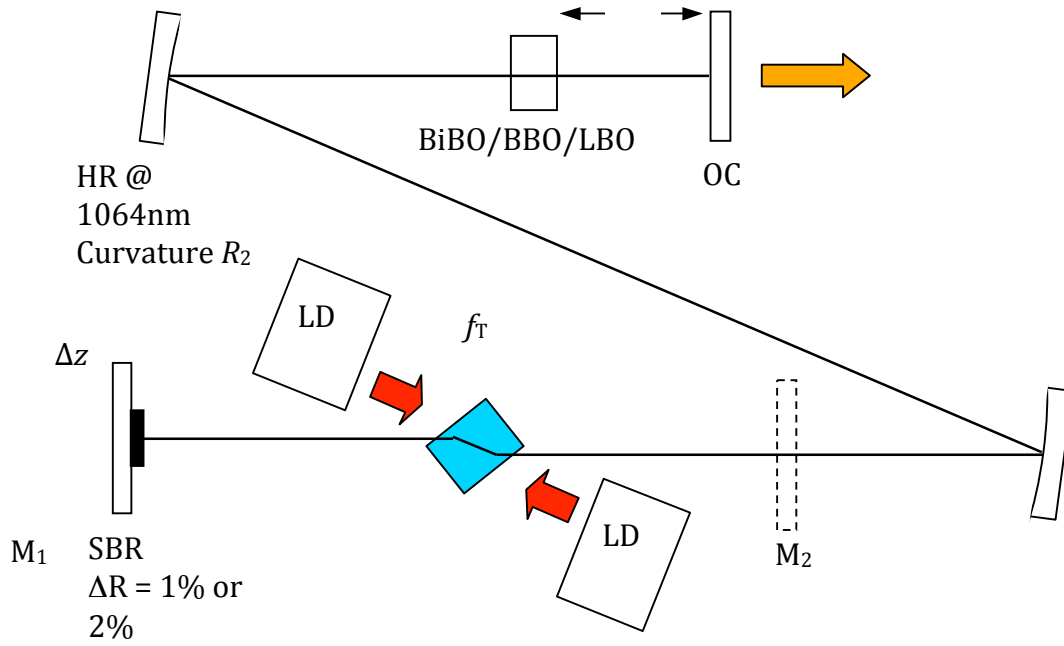


Figure 5.1 Schematic of the extended-cavity, mode-locked, thermal-lens-shaped (focal length f_T), Brewster Nd:GdVO₄ oscillator: LD = 40W laser diode, SBR = saturable Bragg reflector, OC = output coupler, and the Bismuth triborate (BiBO), β -Barium borate (BBO), or Lithium triborate (LBO) second harmonic crystals are positioned a distance d from the OC. The cavity is extended from the plane-plane auxiliary cavity (dashed mirrors M_1 and M_2) on one end using two mirrors with radii of curvature R_1 and R_2 arranged for unity ray transformation on a round trip. The mirror M_1 is replaced by the SBR, which is moved forward by $\Delta z \approx 3\text{cm}$ to match the thermally-induced bowing of the SBR to the intracavity TEM₀₀-mode. (reproduced from 18)

= 1.5m). As a result, the $\sim 400\mu\text{m}$ spot size (half-width $1/e$ of the field) at M_2 is either reproduced or magnified to 0.6mm or 0.8mm, respectively, at the OC. The mirror M_1 terminating the 26cm long arm of the auxiliary cavity is replaced by a half-wave resonant, InGaAs quantum well SBR with a 1% or 2% modulation depth, a saturation fluence of $\sim 70\mu\text{J}/\text{cm}^2$, and a relaxation

time of $\leq 10\text{ps}$ [19]. The spot size of the intracavity TEM_{00} -mode on the SBR varies decreases from about 300 to $200\mu\text{m}$ as the laser output power increases (i.e., the pump-induced thermal focal length f_T decreases). To compensate for thermally-induced bowing and thereby match the radius of curvature of the intracavity mode at high laser output powers (an effect detailed in Chapter 6), the SBR is translated a distance $\Delta z \approx 3\text{cm}$ towards the gain medium, which reduces the cavity length to 1.97m .

In this configuration *without* the SHG crystal and with an optimum 10% OC, the diode-pumped Nd:GdVO₄ laser achieved CW mode locked operation with $15(\pm 1)$ ps pulses only at the highest $\sim 8\text{W}$ output power (limited by the proximity of the edge of the first cavity stability region) and only with the 1% modulation depth SBR. This result, which is of course independent of the telescopic cavity magnification, is consistent with the analysis Kärtner *et al.* [47] which for stable CW mode locked operation with a SBR requires that the intracavity laser pulse energy exceed a critical energy given by

$$E_c = \sqrt{E_A E_L \Delta R_s} \quad (5.1)$$

where ΔR_s is the total amount of saturable losses (i.e., modulation depth) of the SBR, E_A and $E_L = F_{L,sat} A$ are the absorber and laser medium saturation energies, respectively. For Nd:GdVO₄ with an emission cross-section at

1063nm of $7.6 \times 10^{-19} \text{cm}^2$ [6], the 0.64mm^2 mode area in the gain medium [57] implies $E_L \approx 1.6 \text{mJ}$, while $E_A \approx 40 \text{nJ}$ for the smallest $200 \mu\text{m}$ spot size on the SBR. Thus, equation (1) predicts a critical pulse energy of $E_c = 1.05 \mu\text{J}$, which is almost exactly the single intracavity pulse energy for a 76MHz laser resonator producing 8W of average output power with a 10% OC. Moreover, the $\sim 15 \text{ps}$ pulse duration obtained in this cavity configuration is consistent with the analysis of Paschotta and Keller for a slow saturable absorber [42] operating with an incident pulse fluence only slightly above its saturation fluence. Clearly also in agreement with equation (1) is the observation that the 2% modulation depth SBR could not produce CW mode locked operation with a 10% OC.

5.3 Reduction of Mode Locking Threshold

The insertion of a phase-mismatched SHG crystal a distance of $d = 35$ to 55mm from the OC in the $\text{Nd}:\text{GdVO}_4$ laser resonator, allowed TEM_{00} -CW mode locked operation to be achieved at output powers below 3W for intracavity telescope magnifications $M < 1.5$; that is, the CW mode locking threshold was reduced by more than a factor of two by the presence of an intracavity cascaded $\chi^{(2)}:\chi^{(2)}$ process [86].

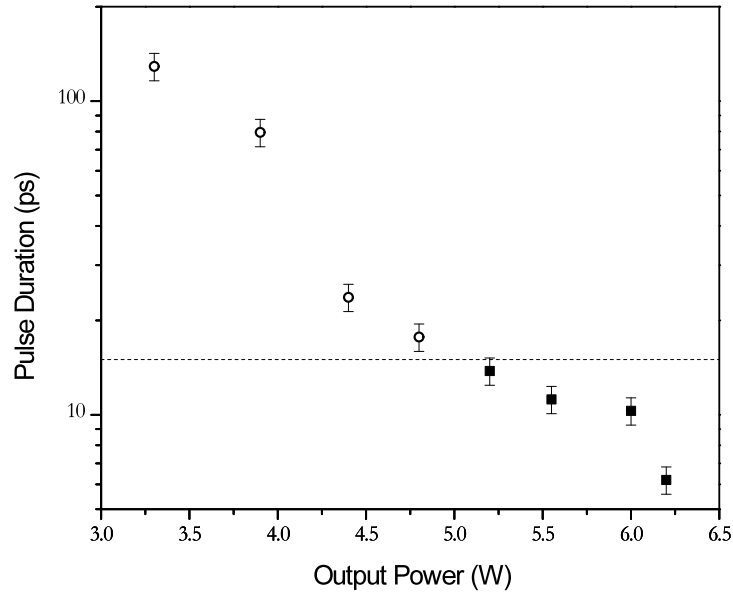


Figure 5.2 Shortest measured pulse duration as a function of the CW mode-locked output power for the TLS Nd:GdVO₄ resonator with $M = 2$, a 1% modulation depth SBR, a 5.0mm BiBO crystal, and a 13% output coupler; $\frac{1}{2}\Delta k.L \approx -\pi$ (open circles) and $\frac{1}{2}\Delta k.L \approx -2\pi$ (filled squares). The horizontal dashed line indicates the 15ps pulse duration obtained at 8W of output power without an intracavity SHG crystal. (reproduced from [18])

The laser performance was investigated for three anti-reflection coated type I SHG crystals: a 5mm Bismuth borate (BiBO; $ee \rightarrow o$) crystal [94] and a 4.9mm β -Barium borate (BBO; $oo \rightarrow e$) crystal, both angled-tuned at room temperature, and a 10mm non-critically phase-matched (NCPM) LBO crystal, phase-matched by temperature tuning. The lowest CW mode locked threshold power was achieved with the BiBO crystal. This is not surprising as it possesses the largest effective second-order nonlinearity (i.e., the product of the crystal length and effective SHG coefficient, $d_{\text{eff}}L$) [51].

However, the most stable long-term (2-3 hour) CW mode locked operation was observed for BBO, which possesses the largest temperature phase-matching bandwidth [95]. Even the $\pm 0.1^\circ\text{C}$ temperature control on the oven enclosing the 10mm NCPM LBO crystal proved inadequate for stable long-term mode locked operation [96, 85].

Figure 5.2 displays the output power dependence of the CW mode locked pulse durations obtained with the BiBO crystal for the largest telescopic resonator magnification ($M = 2$), the 1% modulation depth SBR, and a 13% OC. Under these conditions, equation (1) would predict a CW mode locking threshold output power of over 10W. However, a much lower CW mode locking threshold of only 3.3W, with a pulse duration $\tau \sim 130\text{ps}$, was achieved at a SHG phase-mismatch $\frac{1}{2}\Delta k \cdot l$ around $-\pi$ ($\Delta k = 2k_\omega - k_{2\omega}$, where k_ω and $k_{2\omega}$ are the fundamental and second harmonic wave vectors respectively; Section 5.5 justifies the specified sign of Δk). This experimental result is consistent with the analysis presented in Ref. 78, which for the non-solitonic regime predicts reduced critical laser pulse energy

$$E_c = \sqrt{\frac{P_A \tau \Delta R}{2\tilde{\beta} + \frac{1}{2E_L}}} \quad (5.2a)$$

for the onset of CW mode locked operation, where P_A is the power incident on the SBR and the inverse saturable absorption coefficient for SHG is given by [86]

$$\tilde{\beta} = \frac{4\pi^2 Z_0 (d_{eff} L)^2}{3n^3 \lambda_{\omega}^2 A_{SHG} \tau} . \quad (5.2b)$$

The term ‘inverse saturable absorption coefficient’ correctly implies that this term divides (rather than multiplies) the energy fluence of the laser. It is interesting to note the terms in the numerator of equation 5.2a are descriptive of the absorber while those that result from other cavity elements, namely the gain medium and the SHG crystal, appear in the denominator. The SHG nonlinearity is due to approximately equally strong contributions from the SPM and from the cascaded $\chi^{(2)}:\chi^{(2)}$ process at $\frac{1}{2}\Delta k.L \approx -\pi$ [80, 86]; that is, an effect that primarily affects the *phase* while the SBR process primarily modulates the amplitude of the pulse. As a result, the denominator of the critical energy derived by Schibli et al. [78] should be rewritten as the modulus of i times the inverse saturable absorption coefficient plus one over the inverse of 2 times the laser’s energy fluence, as shown in equation 5.2c.

$$E_c = \sqrt{\frac{P_A \tau \Delta R}{\left| 2i\tilde{\beta} + \frac{1}{2E_L} \right|}} \quad (5.2c)$$

The oscillator presented here employs a 5mm BiBO crystal with $M = 2$, the incident power on the absorber is 25W, and τ , the mode locked pulse duration is 130 ps. The index of refraction is $n \approx 1.6$, $d_{eff} \approx 3\text{pm/V}$ [97, 98], and $\lambda_o = 1063\text{nm}$ (Z_0 is the vacuum impedance). Equation (5.2c) predicts CW mode locking with the second harmonic crystal will first occur at $\sim 0.26 (+/-0.07) \mu\text{J}$ – the $\pm 25\%$ error being due to uncertainties in the pulse duration at the CW mode locking threshold (Figure 2) and the spot size on the SBR. The modified critical energy associated with the theoretical analysis of Schibli *et al.* [78] is therefore consistent with the experimentally determined value for E_c of $0.33\mu\text{J}$ (3.3W output at 76MHz with a 13% OC).

With increasing laser power above the CW mode locked threshold of 3.3W, the output pulse duration is shortened. This is not surprising since both the SBR and phase-mismatched SHG crystal have a stronger mode-locking performance at higher intracavity pulse fluences and intensities. For the fixed configuration of the cavity in Figure 5.2, the pulse duration rapidly drops from $\sim 130\text{ps}$ to below 30ps at an output power of 4.4W. Thereafter, there is a slower decrease in the mode locked pulse duration to $\sim 20\text{ps}$ while the optimum phase-mismatch $\frac{1}{2}\Delta k.L$ remains around $-\pi$ (open circles in Figure 5.2). When the output power reaches $\sim 5\text{W}$, the CW mode locked operation with $\frac{1}{2}\Delta k.L \approx -2\pi$ (the next phase-matching minimum) is more stable (filled squares in Figure 5.2) and produces shorter $\sim 10\text{ps}$ pulse durations at output powers of $\sim 6\text{W}$. Note that the measured pulse duration

above 5W represents a significant pulse shortening [87] over the ~ 15 ps obtained *without* the intracavity SHG crystal at higher output power of 8W. In fact, a pulse nearly twice as short with a duration of 7.6 ps occurs at just over 6W of output power.

A similar CW ML performance trend is also observed for the angle-tuned BBO and temperature-tuned NCPM LBO crystals. For instance, with BBO and a 10% OC, the mode-locking threshold output power at $\frac{1}{2}\Delta k.L \approx -\pi$ is 3W – again consistent with equations (2) since the reduction in $d_{eff}L$ is offset by a higher intracavity power (due to the lower output coupling). At CW mode locking threshold, the pulse durations are again around 100ps, and generally shorter pulse durations are generated as the resonator output coupling is reduced from 15 to 5% (i.e., the intracavity power is increased). However, for the highest CW ML output power, the optimum OC reflectivity is $\sim 90\%$.

5.4 Pulse Shortening

To further investigate the pulse shortening [87] capabilities of this dual-passive mode-locking technique, I varied the beam size in the SHG crystal by operating the CW ML Nd:GdVO₄ laser with different resonator magnifications M while maintaining the same 1.97m cavity length. A reduction in M will decrease the beam area in the SHG crystal, A_{SHG} , which

results in an increase in the strength of the cascaded $\chi^{(2)}:\chi^{(2)}$ process in the SHG crystal.

Figure 5.3 shows four representative second harmonic autocorrelation measurements of the shortest mode locked pulse durations obtained near the maximum $\sim 6\text{W}$ of output power (i.e., at an absorbed diode pump power of 30–35W). The excellent fit of all the data to the autocorrelation of a sech^2 pulse shape (lines in Figure 5.3) is consistent with a passive mode-locking process [42, 47, 78, 81]. All the measurements were performed using a conventional 90% reflective OC at 1063nm, although CW mode locked operation was achieved for flat OCs with transmissivities of up to 20%. Unlike the second harmonic NLM mode-locking technique [85, 96] presented in Chapter 4, a dichroic OC (with high reflectivity for 532nm) is not required. Nonetheless, I found that the best CW ML performance was achieved when the closest face of the SHG crystal is positioned $d = 47(\pm 2)\text{mm}$ from the OC surface. As with the NLM technique, this optimum value of d ensures that any residual green radiation reflected from the OC is not in phase with the first second harmonic generation cycle on the second pass through the crystal. This condition, together with the fact that the shortest pulses were routinely obtained for phase-mismatches of $\frac{1}{2}\Delta k.L \approx m\pi$ ($m = -1, -2, -3 \dots$), clearly minimizes any perturbative influence of reflected green radiation on the cascaded $\chi^{(2)}:\chi^{(2)}$ process – essentially allowing an *independent* nonlinear process to occur on each pass through the SHG crystal.

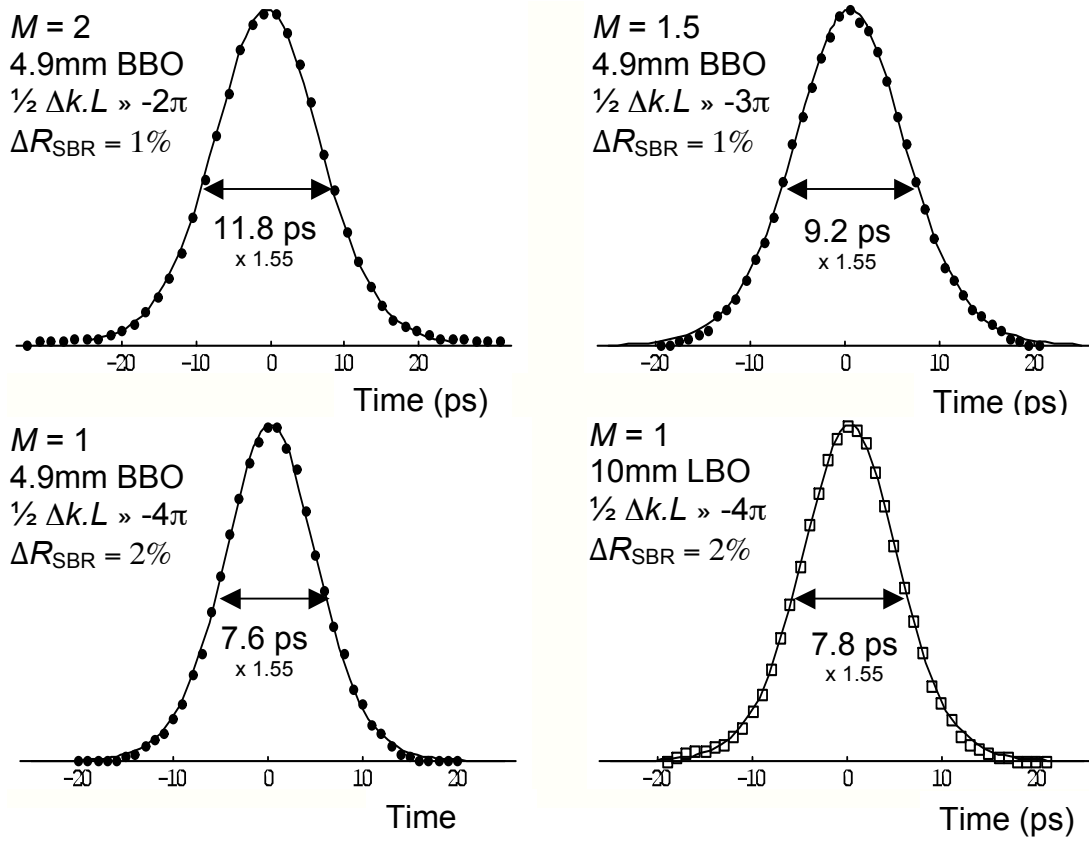


Figure 5.3 Measured second-harmonic autocorrelations (data points) of the shortest pulses produced by the dual-passive mode-locked TLS Nd:GdVO₄ laser under different operation conditions; intracavity telescope magnification (M), β -Barium borate (BBO) and Lithium triborate (LBO) doubling crystals, phase mismatch ($\frac{1}{2}\Delta k.L$), and saturable Bragg reflector modulation depth (ΔR_{SBR}). The data is fit to the autocorrelation function of a sech² pulse (lines). (reproduced from 18)

The data displayed in Figure 5.3 indicate a clear trend: shorter pulse durations are obtained at lower magnifications ($M = R_2/R_1$) of the telescopic cavity, and this is accompanied by a shift of the optimum phase-mismatch of

the second harmonic crystal to larger negative values. This trend is consistent with the interpretation that the second harmonic crystal acts as the phase-locker in the mode-locking process. In the frequency domain [74], the full cyclical SHG conversion processes occurring in one pass through the nonlinear crystal when $\frac{1}{2}\Delta k.L \approx m\pi$ produces a back-converted and correctly phased, fundamental axial-mode spectrum that is about $\sqrt{3}$ times broader than that of the original incident pulse. As the magnification M decreases, thereby decreasing the intracavity laser spot size in the nonlinear crystal positioned near the OC, this phase-locking SPM contribution to the cascaded $\chi^{(2)}:\chi^{(2)}$ process [80] significantly increases in strength; in fact, this effect is proportional to the intensity of the laser pulse squared (I^2). The result is shorter output pulse durations since the bandwidth of the mode locked spectrum is increased. However, if the nonlinear phase-locking mechanism becomes too strong, multiple pulses per round trip are generated in the diode-pumped CW ML Nd:GdVO₄ laser – in agreement with the analysis of Ref. 78. For example, the onset of multi-pulse operation for the initial optimum phase-mismatch at $\frac{1}{2}\Delta k.L \approx -\pi$ occurred at more or less twice the CW mode locked threshold power for all the cavity configurations of Figure 5.3. To offset this effect, the strength of the cascaded $\chi^{(2)}:\chi^{(2)}$ process must be reduced by further detuning the frequency doubling crystal from $\Delta k = 0$. Moreover, I found that for $M = 1$ (Figures 5.3(c) and (d)), when the cavity irradiance in the nonlinear crystal is at least a factor of 4 greater than for $M = 2$, it was

also necessary to employ a 2% modulation-depth SBR (i.e., increase E_A in equations (1) and (2)) to obtain stable mode-locking with a single intracavity pulse. In this $M=1$ case, for both the BBO and LBO crystals, the laser could be mode locked with the 1% modulation-depth SBR from a lower threshold output power of 1.5-2W, but generally exhibited double pulsing per round trip above ~ 4 W of output power.

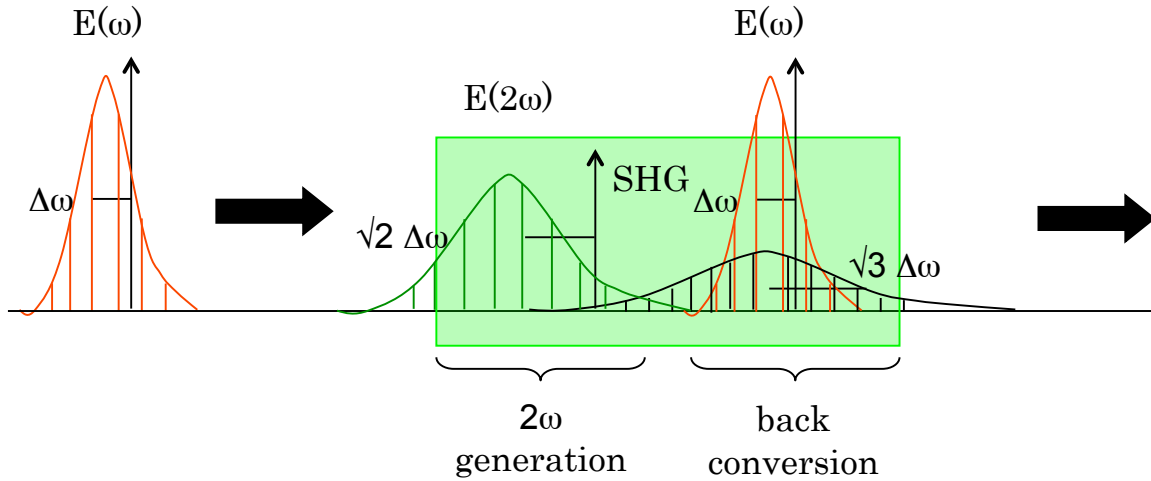


Figure 5.4 This figure shows a pulse with a bandwidth of $\Delta\omega$ as it is forward converted into its second harmonic – and a band width of $\sqrt{2} \Delta\omega$ and back converted to its fundamental and a bandwidth of $\sqrt{3} \Delta\omega$ on a single pass through the second harmonic generating crystal.

The fact that the 4.9mm BBO and 10mm LBO crystals produced similar 7.4ps and 7.6ps output pulse durations for $M=1$ and $\frac{1}{2}\Delta k.L \approx -4\pi$

(Figures 5.3(c) and (d)) is also consistent with the interpretation of the dual-passive (amplitude and phase) mode-locking mechanism. The factor of two difference in the two crystal lengths compensates very nearly for the difference in their second harmonic nonlinear coefficients [95], thus ensuring approximately the same effective nonlinearity (e.g., $d_{eff}L$ in equation (2b)) in the single-pass, four-fold, forward and backward frequency conversion process.

The effects of group velocity mismatch (GVM) are also expected to be very similar since the values for GVM for the frequency doubling of 1063nm radiation are $\sim 85\text{fs/mm}$ for BBO [75, 95] and $40\text{-}50\text{fs/mm}$ for NCPM LBO [95, 97]. Thus in both cases, over the characteristic one-quarter crystal length of the nonlinear interaction $\left(\frac{1}{2}\Delta kL = -4\pi\right)$, the GVM is an insignificant fraction of the generated picosecond CW ML pulse duration. I note that any effects of birefringent beam walk-off are also expected to be negligible due to the relatively large intracavity beam diameter in the SHG crystals.

5.5 Phase Mismatch

To further investigate the role of the SHG phase-mismatch in the dual-passive mode-locking technique, the CW mode locked output pulse duration was measured as a function of the temperature of the 1cm intracavity LBO

crystal under the operational conditions of Figures 5.3(c) and (d); i.e., $M = 1$, $\Delta R_{\text{SBR}} = 2\%$, and a constant 6W output power with a 10% OC. Specifically, a relative measure of the pulse duration was obtained by monitoring an extra-cavity second harmonic signal produced in the small signal limit (conversion efficiency $< 5\%$) by placing the 4.9mm BBO crystal in the unfocused CW mode locked output beam. Figure 5.5 shows the data obtained over the region from $\frac{1}{2}\Delta k.L \approx -6.5\pi$ to $\frac{1}{2}\Delta k.L \approx -3.5\pi$ where the diode-pumped Nd:GdVO₄ laser exhibited stable single-pulse CW mode locked output with the shortest $\sim 10\text{ps}$ pulses. Here, the temperature-dependent Sellmeier equations for LBO reported by Kato [97] together with the observed minima in the single-pass SHG efficiency are used to calibrate Δk to the measured crystal temperature.

The results clearly indicate two important features of the mode-locking scheme. First, the fact that the shortest pulses are produced at LBO crystal temperatures less than the NCPM temperature of 148°C confirms that the required phase-mismatch for efficient short-pulse mode-locking is indeed negative – as indicated for the results obtained with angle-tuned BiBO and BBO intracavity SHG crystals in Sections 5.2 and 5.3. Second, since the laser output power remained constant (to within $\pm 3\%$) and the TEM₀₀ output mode size did not vary (constant diode pump current and hence thermal lensing in the gain medium), the shortest ML pulses (corresponding to the highest external second harmonic power) are clearly generated at $\frac{1}{2}\Delta k.L \approx m\pi$, with the minimum pulse duration obtained when $m \approx -4$.

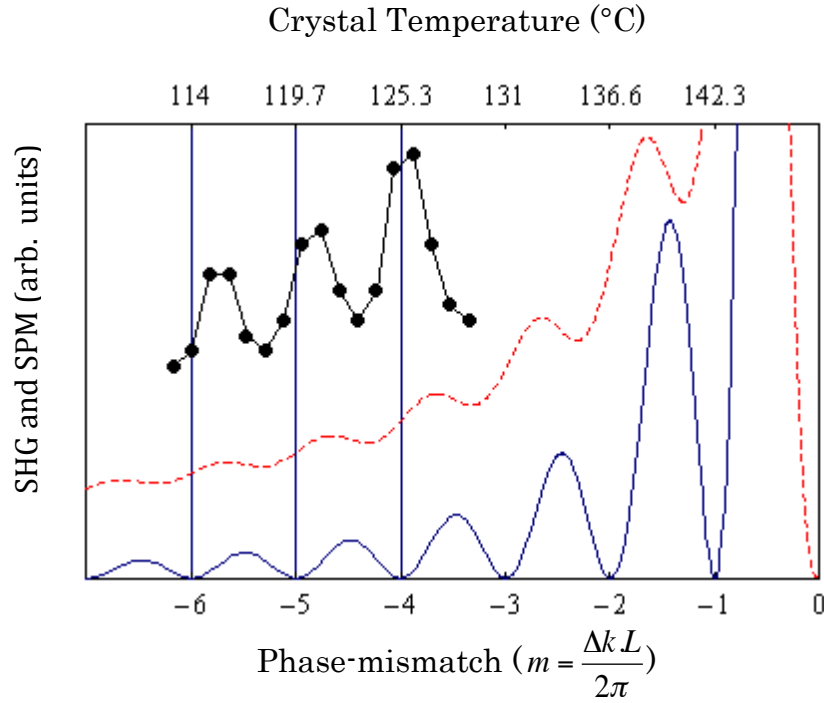


Figure 5.5 Dependence of the extra-cavity second-harmonic generation signal (data points) as a function of phase-mismatch (i.e., crystal temperature) in the region of stable 6W CW ML operation between $\frac{1}{2}\Delta k.L \approx -6.5\pi$ and $\frac{1}{2}\Delta k.L \approx -3.5\pi$ for the 1cm-long NCPM Lithium triborate (LBO) doubling crystal with cavity parameters $M = 1$ and $\Delta R_{\text{SBR}} = 2\%$. Also shown are the SHG (solid line) and SPM (dashed line) contributions for the cascaded $\chi^{(2)};\chi^{(2)}$ process from equation (3). (reproduced from 18)

The requirement that Δk be negative can be understood in terms of the spectral dynamics of the mode-locking process. For laser resonators operating without dispersion compensation (e.g., Fig. 5.1), the long wavelength (red) spectral components of an ultrashort intracavity pulse will precede the short wavelengths (blue) so that the former are preferentially absorbed by a slow saturable absorber [42]. Although the SBRs have relaxation times of the same order as our CW mode locked pulse durations

[19], they are not ‘fast’ [81] and so will still predominantly deplete the red spectral components on the leading edge of the pulse. In order to compensate for the resultant spectral blue-shifting [42] and hence help stabilize the mode-locking process, another intracavity component will need to generate red spectral components mainly on the leading edge of the pulse. For Kerr-like SPM, this requires a positive nonlinear coefficient, which can only be achieved for a negative phase-mismatch in a cascaded $\chi^{(2)}\text{:}\chi^{(2)}$ process [80]. This can be seen from the expression of the instantaneous field amplitude $E_\omega(L)$ after a single pass through the SHG crystal [86]

$$E_\omega(L) \approx \left\{ 1 - \frac{\xi}{2} \text{sinc}^2\left(\frac{\Delta k L}{2}\right) - \frac{i\xi}{2\Delta k L} [1 - \text{sinc}(\Delta k L)]^2 \right\} E_\omega(0) , \quad (3)$$

where $\xi \propto |E_\omega(0)|^2$ is the low-depletion SHG efficiency. Clearly, the effective nonlinear Kerr coefficient for the phase-mismatched SHG process (the imaginary part of equation (3) plotted as a dashed line in Figure 5.5) is positive only for a negative Δk .

Additional supporting evidence for the above interpretation comes from our attempts to mode lock the diode-pumped Nd:GdVO₄ laser at a positive phase-mismatch. Only for narrow ranges of positive Δk is CW mode locking operation possible, and then the pulse duration is typically much greater than 30ps. There is therefore no indication of any pulse shortening due to phase-locking through SPM with a negative effective nonlinear Kerr coefficient: that is, the regime of pure soliton mode-locking with positive

dispersion and negative nonlinear phase shifts [92] was not attained.

Instead, a positive phase-mismatch simply exacerbated the dispersion-generated spectral blue-shift due to reflection from the SBR, thus only allowing mode locked operation with narrow spectral pulse bandwidths.

The fact that inverse saturable absorption due to the nonlinear cascaded $\chi^{(2)}:\chi^{(2)}$ process tends to broaden the mode locked pulse duration [78, 80], by enhancing loss for shorter more intense pulses, explains the observed oscillatory dependence of the pulse duration with Δk in Fig. 5.5. When $\frac{1}{2}\Delta k.L \approx (m+\frac{1}{2})\pi$, residual second harmonic radiation exits the SHG crystal and the resonator (the OC is only weakly reflective to the green), causing loss to the resonator – the resulting inverse saturable absorption loss being proportional to the SHG efficiency. The CW mode locked laser attempts to compensate for this reduction in resonator quality factor Q by operating with a longer pulse duration, which reduces the SHG efficiency (i.e., cavity loss) at a constant output power. On the other hand, when $\frac{1}{2}\Delta k.L \approx m\pi$, the back conversion to the fundamental in the cascaded $\chi^{(2)}:\chi^{(2)}$ process is complete on one pass through the SHG crystal, thereby minimizing cavity loss and allowing CW mode locked operation with a shorter pulse. The same oscillatory behavior was observed by Wallenstein [91] in a hybrid mode locked Nd:YVO₄ laser with an acousto-optic (AO) modulator and a phase-mismatched LBO crystal. In that case, however, the short ~ 10 ps pulses could be generated for both positive and negative Δk (i.e., at $|\frac{1}{2}\Delta k.L| \approx m\pi$,) since an AO modulator

usually operates without an intrinsic spectral dependence to its loss modulation.

It is interesting to note that the very shortest pulses are produced a slightly greater phase-mismatches than $\frac{1}{2}\Delta k.L = m\pi$. This shift towards $\Delta k = 0$ is most pronounced for $m = -6$ (Fig. 5.5), where the larger phase-mismatch has already considerably reduced the strength of the inverse saturable absorption. As a result, the Nd:GdVO₄ laser can tolerate a little residual loss to SHG in favor of an increase in the strength of the phase-locking due to SPM in the cascaded $\chi^{(2)}:\chi^{(2)}$ process. The positive gradient of the imaginary part of equation (3) around $\frac{1}{2}\Delta k.L \approx m\pi$ (dashed line in Fig. 5.5) then ensures a shift towards zero Δk in the optimum phase-mismatch generating the shortest pulses. For $m = -4$, this shift is considerably smaller due to the increase in the strength of the inverse saturable absorption from SHG. I also note that the dependence of the gradient of the imaginary part of equation (3) on Δk around $\frac{1}{2}\Delta k.L \approx m\pi$ could serve to further stabilize the shortest CW ML pulses against the dispersion-generated frequency-dependent reflectivity of the SBR [42]. Since LBO, in common with BBO and BiBO, has positive group velocity dispersion for SHG around 1 μ m, the red spectral components of the pulse will experience a slightly higher effective nonlinear Kerr coefficient than the blue: specifically, for the red spectral components, Δk is less negative (i.e., shifted towards $\Delta k = 0$ in Fig. 5.4). The resulting frequency dependence of the imaginary part of equation (3) may

partially balance the preferential absorption of leading red components of the pulse spectrum by the SBR in the dual-passive CW mode locked scheme.

6. LASER INDUCED THERMAL EFFECTS IN SATURABLE BRAGG REFLECTORS

6.1 Introduction

As a result of the importance of SBRs in mode locking [37, 41, 42, 82], which was discussed in Chapter 4, the optical response of SBRs has been extensively studied [99]. However, little attention has been paid to laser-induced thermal effects in SBRs. In spite of this, there have been reports that thermal bowing of SBRs necessitates a repositioning of this optical element in the laser resonator to ensure that its deformed surface and the wavefront of the oscillating intracavity mode remain closely matched [18, 31]. Cavity stability issues and the optical aberrations caused by thermal deformation of the SBR mirror surface are likely to become more pronounced considering the trend towards designing mode locked oscillators with increased average power.

This chapter presents a semi-analytical evaluation of the thermal deformation of III-V semiconductor-based (i.e., GaAs-based) SBRs induced by the incident laser-beam. Timoshenko's analysis [100] is used to evaluate the thermal deformation from the thermoelastic displacement potential that results from the integration of the steady-state temperature distribution in a

SBR (Section IV). Sections II and III present the derivation of the required temperature profile; finite Hankel and cosine transformations are used to find the solution to the three-dimensional heat equation that results from the heat source of laser pulses incident on the SBR. Prior analyses have used equivalent formalism to evaluate the bowing of dielectric mirrors in laser cavities that occur from the residual absorption [101-103] of the laser intensity. In the case of an SBR, the saturable portion of the heat source due to ΔR_{sat} requires particular attention. In Section V, several results for several different laser spot sizes and SBR dimensions are shown and the apparent trends in both the strength of the thermally-induced lens (bowing) as well as the resultant optical aberrations from a perfect mirror are discussed.

6.2 The Three-Dimensional Heat Equation and Boundary Conditions

The thermal effects in a SBR used for CW mode locking a laser depend upon the SBR's thermal properties as well as the absorbed average laser power (the heat source). For a TEM₀₀-mode laser, the laser pulse's intensity has a spatial dependence of the form $\exp\left[-\frac{2r^2}{w^2}\right]$ where w , the spatial spotsize, is the half-width at 1/e maximum (HWE⁻¹M) of the electric field of the incident intracavity laser beam. Serious diffraction effects of the

laser mode can be avoided by ensuring the $(HWe^{-1}M)$ spotsize is less than four times the mirror width of the SBR. In this limiting case the laser beam intensity at the edge of the SBR falls to $\exp[-8] \approx 3 \times 10^{-4}$ of its peak value. The symmetry of the heat source makes the use a cylindrical coordinate system a logical choice. This results in treating the SBR as a cylinder of radius a rather than a parallelepiped of side $2a$. The use of this approximation does not have large effect on the results and allows for an analytical description of the temperature profile in the SBR through the exploitation of the system's radial symmetry. The orientation of the cylindrical coordinate of the SBR of thickness d and diameter $2a$ is shown in Figure 6.1. Propagation of the Gaussian laser beam is along the z direction and is taken to be centered on the SBR at $(r, z) = (0, 0)$.

This analysis is intended for use with laser oscillators that employ SBRs that have response times much larger than the inverse of the laser's repetition rate. This condition ensures the excited electrons in the conduction band have time to relax to the ground state before the next laser pulse arrives. If this is not the case, this analysis is still valid as long as an 'effective' saturation fluence is used to describe the SBR. For similar reasons, it is assumed that negligible carrier diffusion occurs over the recombination time of the saturable Bragg absorber, $\tau_R \sim 10\text{ps}$ [19]. This is clearly an excellent approximation in the z -direction because the carriers are trapped in the quantum well. This is also a good approximation in the

radial r -direction because the spot size of the beam is much larger than the diffusion length [104] ($w \gg l_{diff} \sim 0.5\mu m$). This analysis also assumes the thermal response of the SBR has reached the quasi steady state case so that the three-dimensional radially-symmetric (time-independent) heat conduction may then be written as

$$\frac{\partial^2 T}{\partial r^2} + \frac{1}{r} \frac{\partial T}{\partial r} + \frac{\partial^2 T}{\partial z^2} = - \frac{\alpha \cdot q(r)}{\kappa_{th}} e^{-\alpha z}, \quad (6.1)$$

where $q(r)$ describes the radial dependence of the heat source and κ_{th} is the thermal conductivity. Of course, in writing equation (6.1), it has been assumed that the z -dependence of the heat source can be approximated by a simple exponential absorption with a single coefficient α . Technically, the heat source should be dependent upon two separate absorption coefficients, one that corresponds to the saturable absorption that occurs in the quantum well(s) and the other to the nonsaturable absorption that occurs in the bulk material (i.e., the reflective Bragg mirror of the SBR). However, approximation of a single absorption coefficient, $\alpha = 10^4 \text{ cm}^{-1}$, is justified since both the Bragg mirror ($\sim 4\mu m$) and quantum well thickness ($\sim 10\text{nm}$) internal to the SBR are very much less than the $\sim 0.5\text{mm}$ thickness of the overall SBR; i.e., the heat source is a surface effect. Furthermore, the value

of α has very little effect on the overall temperature distribution as long as $\alpha d \gg 100$.

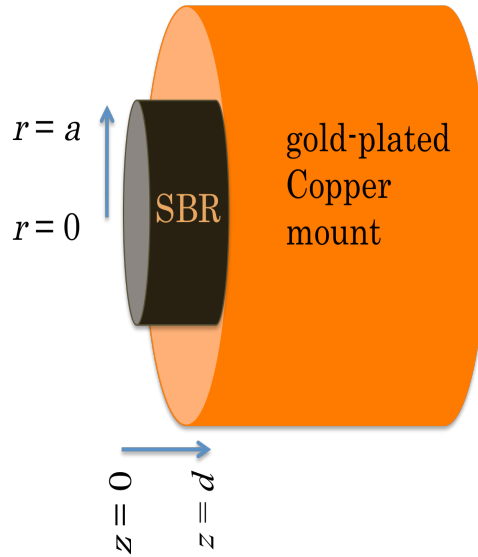


Figure 6.1 shows the idealized cylindrical SBR mounted on a gold-plated copper cooling block.

The standard thermal conduction boundary conditions that describe the heat conduction at the boundaries of the SBR are shown in equations 6.2(a)-2(c). The relative interface heat transfer coefficients, h_{air} and h_{Indium} , mitigate the flow of heat out of the SBR. It is assumed that the interface between the Indium solder (used to attach the SBR to the Cu block) and the Cu block is perfect (i.e., $h_{In-Cu} = 0$), so that the two metallic materials have the same temperature. In order to allow for the evaluation of the temperature of the SBR with respect to its surrounding, the temperature of

both the Copper cooling block and the surrounding air are arbitrarily set to zero.

$$k_{th} \frac{\partial T}{\partial r} \bigg|_{r=a} = h_{air} T(r=a, z) \quad (6.2a)$$

$$k_{th} \frac{\partial T}{\partial z} \bigg|_{z=0} = h_{air} T(r, z=0) \quad (6.2b)$$

$$k_{th} \frac{\partial T}{\partial r} \bigg|_{z=d} = h_{Indium} T(r, z=d) \quad (6.2c)$$

6.3 Heat Per Unit Volume

The heat per volume deposited in the SBR in the radial direction is determined by the fraction of the incident laser pulse that is absorbed (i.e., not reflected) by the SBR. The reflectivity, R_{SBR} , of the SBR is given by

$$R_{SBR} = 1 - \Delta R_{NS} - \frac{\Delta R_S}{1 + \frac{F(r)}{F_S}}, \text{ where } \Delta R_S \text{ and } \Delta R_{NS} \text{ are the saturable and non-}$$

saturable changes in reflectivity [24], respectively. The saturable absorption depends upon the ratio of the fluence of the incident laser pulse to the saturation fluence of the SBR. The pulse fluence is given by

$$F(r) = F_o \exp\left(-\frac{2r^2}{w^2}\right), \text{ where } F_o \text{ is the peak } (r=0) \text{ pulse fluence given by}$$

$$F_o = \int I(t) dt = \frac{2U}{\pi w^2} \text{ and } U \text{ is the pulse energy. The saturation fluence, } F_S, \text{ is}$$

a device specific parameter. The heat source term, $q(r)$, can written as

$$q(r) = R_{rep} F_o \exp\left(-\frac{2r^2}{w^2}\right) \left[\Delta R_{NS} + \frac{\Delta R_s}{1 + \frac{F_o}{F_s} \exp\left(-\frac{2r^2}{w^2}\right)} \right], \quad (3)$$

where R_{rep} is the repetition rate of the laser.

This chapter is concerned with the conditions for generating a single pulse in the laser cavity. As a result, these analyses are primarily calculated for an energy fluence of $3F_s$ because this is the energy fluence regime for which multiple pulse breakup [77] can be avoided. It is also worth noting that since the effect of two-photon absorption (TPA) first becomes appreciable at energy fluences [42] of at least $5F_{sat}$, TPA has not been included in our treatment. It is, in principle, possible to include this effect. An intensity dependent TPA effect, $\left(I_o = \frac{F_o}{\tau_l}\right)$ that varies with laser pulse duration (τ_l) would need to be used. However, if TPA is to be properly treated, the modified analysis must also take into account the anisotropy of TPA in zinc-blend semiconductors [105].

6.4 Temperature

The above approximations allow the three-dimensional heat equation (equation (6.1)) to be solved analytically by performing two subsequent integral transformations: a finite cosine transformation in z followed by a

finite Hankel transformation in r . The definition of the finite cosine transformation of the z -coordinate is

$$\tilde{T} = \int_0^a T \cos(uz + \phi) dz, \quad (6.4)$$

where u is a positive root of the transcendental equation: $u \tan(ud + \phi) = \frac{h_{Indium}}{k_{th}}$

and $u \tan(\phi) = \frac{h_{air}}{k_{th}}$. The inverse transformation is thus

$$T(z) = \sum_l a_l \cos(u_l z + \phi_l) \quad (6.5a)$$

where

$$a_l = \tilde{T}(u_l) \frac{4u_l}{2u_l d - \sin(2\phi_l) + \sin(2(u_l d + \phi))} \cos(u_l z + \phi_l). \quad (6.5b)$$

The finite Hankel transformation is defined as

$$\tilde{T}(p) = \int_0^a T(r) J_0(pr) r dr; \quad (6.6)$$

so that the inverse transformation is

$$T(r, z) = \frac{2}{a^2} \sum_n \frac{\tilde{T}(p_n, z) J_0(p_n r)}{J_0^2(p_n a) + J_1^2(p_n a)}, \quad (6.7)$$

where p_n are the positive roots associated with the boundary condition at $r = a$ (equation 6.2(a)).

The integral transformations of the left hand side of the heat equation (equation (6.1)) are performed using integration by parts. Likewise, the finite cosine transformation of the heat source term on the right hand side is

easily calculated using integration by parts. The finite Hankel transformation of the heat source is more difficult and is detailed in Appendix A. The non-saturable term transforms relatively nicely into a series solution that has two cases: $\frac{pw^2}{4a} < 1$ and $\frac{pw^2}{4a} > 1$. In contrast, a solution to the saturable term is only tractable if the term is first expanded as a series of Gaussians of varying widths. Then, for each laser spot size, a fitting parameter g is chosen to ensure that a low number of Gaussians, each labeled by g and with a specific amplitude β_g , can be used to faithfully represent the actual saturable function:

$$\frac{\Delta R_s}{\mathcal{F} + \exp\left[\frac{2r^2}{w^2}\right]} = \Delta R_s \sum_{g=1}^{g^{final}} \beta_g \exp\left[-\frac{\gamma g r^2}{w^2}\right], \quad (8)$$

where $\mathcal{F} = \frac{F_o}{F_s}$. In each case, this expansion will transform nicely because the

saturable term now has the same form as the non-saturable term.

The resulting analytic solution to the steady-state temperature profile is:

$$\begin{aligned}
T(r,z) = & \frac{2}{a} \sum_{l,n=1}^{\infty} \frac{4u_l \cos(u_l z + \phi_l)}{2u_l d + \sin(2(u_l d + \phi_l)) - \sin(2\phi_l)} \frac{J_0(p_n r)}{J_1^2(p_n a) + J_0^2(p_n a)} \frac{\alpha_a P_0}{(\alpha_a^2 + p_n^2)(\alpha_a^2 + u_l^2)k_{th}} \times \\
& \left(\Delta R_{NS} \frac{w_0^2}{4} \left\{ \begin{aligned} & \exp\left(-\frac{p_n^2 w_0^2}{8}\right) - \exp\left(-\frac{2a^2}{w_0^2}\right) \sum_{m=0}^{\infty} \left(-\frac{p_n w_0^2}{4a}\right)^m J_m(p_n a) & \text{when } \frac{p_n w_0^2}{4a} < 1 \\ & \exp\left(-\frac{2a^2}{w_0^2}\right) \sum_{m=1}^{\infty} \left(\frac{4a}{p_n w_0^2}\right)^m J_m(ap_n) & \text{otherwise} \end{aligned} \right. \right) \times \\
& + \left(\Delta R_s \frac{w_0^2}{4} \left\{ \begin{aligned} & \frac{\beta_g}{g} \exp\left(-\frac{p_n^2 w_0^2}{4\gamma g}\right) - \exp\left(-\frac{\gamma g a^2}{w_0^2}\right) \sum_{m=0}^{\infty} \left(-\frac{p_n w_0^2}{2\gamma a g}\right)^m J_m(ap_n) & \text{when } \frac{w_0^2 p_n}{2a\gamma g} < 1 \\ & \frac{\beta g}{g} \exp\left(-\frac{\gamma g a^2}{w_0^2}\right) \sum_{m=1}^{\infty} \left(\frac{2\gamma g a}{p_n w_0^2}\right)^m J_m(ap_n) & \text{otherwise} \end{aligned} \right. \right) \times \\
& (u_l \sin(u_l d + \phi_l) \exp(-\alpha_a d)) - \alpha_a \cos(u_l d + \phi_l) \exp(-\alpha_a d) + \alpha_a \cos(\phi_l) - u_l \sin(\phi_l)
\end{aligned}$$

Figure 2 depicts two examples of $T(r,z)$ when laser pulses with a peak fluence $F = 3F_{sat}$ and spot sizes of $w = 100\mu\text{m}$ and $w = 1\text{mm}$ are incident on a 2mm-radius SBR with a 400 μm thickness. It is assumed the SBR is the end mirror of a 100MHz repetition rate mode locked laser, and has a saturable absorption of 0.8% with a slightly higher non-saturable absorption of 1.2% [19]. The steady-state temperature profiles were evaluated using standard material parameters and coefficients: 0.9W/(cm².K) for h_{Indium} [106], 10⁻³ W/(cm².K) for h_{air} [38], and $k_{th} = 0.45\text{W}/(\text{cm.K})$ for the thermal conductivity of GaAs [108, 109]. The heat flux, $\frac{d}{dx} \left(\int T(r,z) r dr \right)$, is evaluated at all values of z and is found to be constant which is

characteristic of a steady-state solution. This heat flux check includes conduction out of the SBR-air interface at $r = a$ (equation 2(a)). The boundary conditions of equations 2 have also been verified to hold within a numerical error of less than 1%.

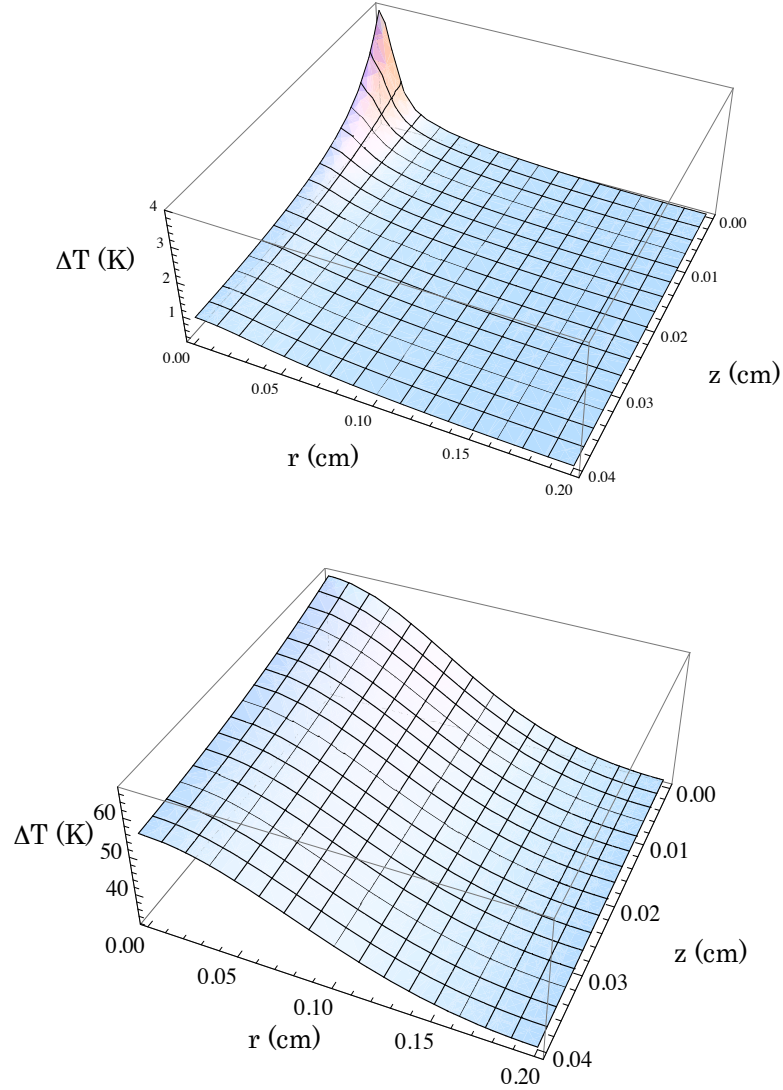


Figure 2. Top figure shows the resulting temperature distribution (K) in a 0.2x.02x0.04cm SBR when the laser spotsize is 100mm. Bottom figure show the resulting temperature distribution (K) in a 0.2x.02x0.04cm SBR when the laser spotsize is 1mm.

A strong radial conduction away from the heat source at $(r,z) = (0,0)$ is expected when $w \ll a$. This trend is clearly shown in Figure 6.2 for the 100 μm laser spot size. This, of course, implies that for $w = 100\mu\text{m}$, $(dT/dz)_{r=0}$ is not a constant. In stark contrast to the 100 μm spot size are the results for the larger 1mm laser spot size. In this case, $w \sim a$ results in near unidirectional heat flow towards the copper heat sink at $z = d$. This is not surprising when it is considered that, for this spot size, heat flow is predominantly towards the largest area and heat transfer coefficient h . Figure 2 also shows the temperature difference between the SBR and its surroundings is a strongly dependent upon the incident laser spot size. This is also not surprising because the temperature profiles were evaluated for the constant incident pulse fluence condition $F = 3F_{sat}$. Therefore, the heat absorbed by the SBR scales as w^2 . This may seem to imply that the peak temperature at $(r,z) = (0,0)$ for $w = 1\text{mm}$ will be 100 times greater than that for $w = 100\mu\text{m}$. The influence of the radial heat conduction when $w \ll a$ of course explains why this is not true; the peak temperature for $w = 1\text{mm}$ is 63K while it is 4K for $w = 100\mu\text{m}$. The details of the overall temperature distribution affect the thermal deformation (i.e., bowing) of the front surface of the SBR because, as will be described in the next section, the temperature distribution is integrated over a Green's

function solution. Consequently the choice of spot size on a given SBR will effect the laser operation through both resonator stability and spherical aberrations [110-112].

6.5 Thermal Deformation

The analytical solution to the steady-state three-dimensional temperature profile is used to calculate the thermoelastic displacement potential, Ψ , as described by Timoshenko [100];

$$\Psi = -\frac{(1+\nu)\alpha_{\text{exp}}}{4\pi(1-\nu)} \iiint T(r,\phi,z) \frac{1}{r'} r dr d\phi dz. \quad (9)$$

In this equation, ν is Poisson's ratio, α_{exp} is the coefficient of thermal expansion, $T(r,\phi,z)$ is the temperature at a point (r,ϕ,z) with volume element $rdrd\phi dz$ and r' is the distance between this point and the point (r',ϕ',z') . The bowing of the SESAM in the z direction is calculated by taking the first

derivative of Ψ in z and evaluating the expression at $z = 0$; i.e., $\left. \frac{\partial \Psi}{\partial z} \right|_{z=0}$. The

use of this thermoelastic potential to find the deformation of the SBR that results from the stress/strain relationships is only legitimate when free-expansion can occur on all of the object's boundaries. This condition clearly holds for three of the four boundaries for an SBR. It is also expected to be reasonable for the back face of the SBR because the solder is very malleability when compared to the rigidity of the GaAs.

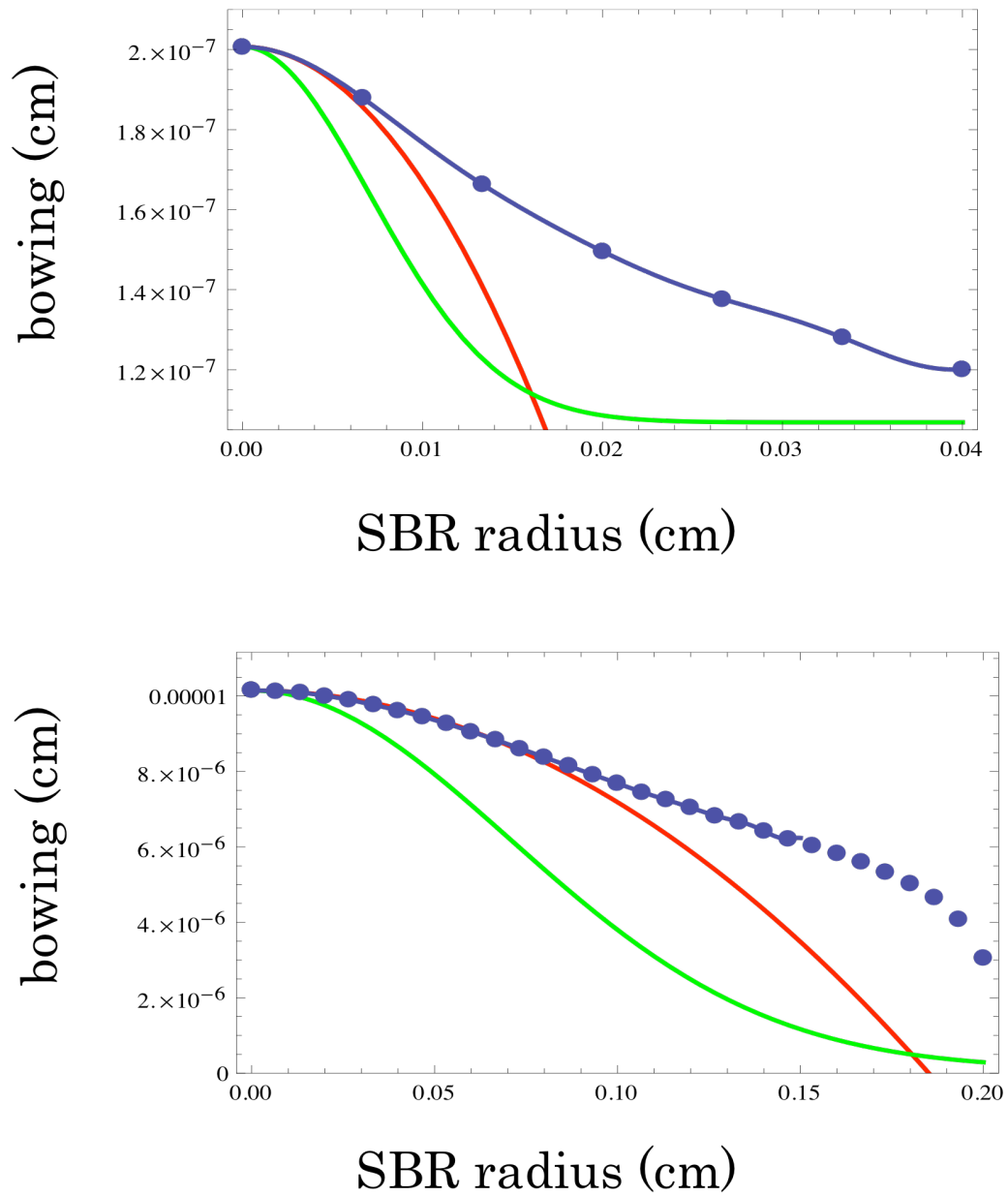


Figure 6.3 Top figure shows the perfect lens or parabolic fit (red line) to the bowing of a 400mm thick SBR (blue data points) that results from a 100 μ m incident laser mode (green line). Bottom figure shows the perfect lens or parabolic fit (red line) to the bowing of a 400 μ m thick SBR (blue data points) that results from a 1mm incident laser mode (green line).

Several assumptions have been made in adopting this approach to find the thermal deformation of the SBR's front surface. The material properties of the quantum well and Bragg mirror stack have been assumed to have similar material properties to the bulk GaAs substrate or to not contribute significantly to the bowing. This assumption is justified by considering that (i) the material properties of the III-IV zincblend semiconductors used to make the SBR (GaAs, AlAs, and InAs) are quite similar -- the relevant material parameters of GaAs and AlAs which form the Bragg mirror stack and hence over 99% of the deposition on the GaAs substrate do not vary by more than 20% [113] --and (ii) together both the quantum well and the Bragg stack only comprise ~1% of the total SBR thickness (albeit at the front surface).

Figure 6.3 shows the calculated front surface deformation, $\Delta z(r)$, near the 100 μ m and 1mm laser spot sizes -- the plots are shown to $r = 5w$ for the 100 μ m case and the full range for the 1mm spotsize. The bowing was calculated from the temperature profiles depicted in Figure 6.2; that is, they have been calculated for a 100MHz laser operating at $F = 3F_{sat}$ using a 4x4x0.4mm SBR. The significant influence on $\Delta z(r)$ of edge effects at $r = a$ are clearly evident for the larger 1mm laser spot size. In all cases, a polynomial expansion of the form $c_n r^{2n}$ ($n = 0, 1, 2 \dots$) is fit to the deformation $\Delta z(r)$. This allows the thermally-induced SBR bowing to be quantified and compared to a

perfect parabolic ($n = 1$) mirror. Figure 6.3 also shows the Gaussian profile of the incident laser field distribution (green line), $\exp[-(r/w)^2]$, and the parabolic contribution (red line) associated with a perfect mirror, $c_0 + c_1 r^2$, to the deformation for the two example cases. Figure 6.3 clearly indicates the radial dependence of the thermally-induced bowing of the SBR deviates from a perfect parabolic mirror (red line) over the spatial laser mode profile (green line). This deviation indicates that optical aberrations in the deformed SBR mirror could perturb the oscillation laser mode.

6.6 Lensing and Aberrations

It is useful to describe the strength of the laser-induced thermal lens in the SBR cavity mirror and its aberrations by comparing their form to those of a spherical mirror of radius R for which

$$\Delta z(r) = \Delta z_0 + \frac{r^2}{2R} + \frac{3r^4}{8R^3} + \dots$$

where Δz_0 is an arbitrary constant. Figure 6.4 shows the magnitudes of $1/R$ and $8c_2 R^3/3$ associated with the SBR's deformation as a function of the laser spot size w . The magnitude of $1/R$ is directly related to the strength of the negative thermally-induced SBR focusing, while $8c_2 R^3/3$ normalizes the aberrations present in the SBR mirror to those that

exist in an equivalent spherical mirror of radius R . All of the data was evaluated for the following conditions: $a = 2\text{mm}$, $d = 400\mu\text{m}$, $F = 3F_{\text{sat}}$ and $R_{\text{rep}} = 100\text{MHz}$. The results are consistent with the perspective that when $w \ll a$ the localized heat source undergoes strong transverse thermal conduction (Figure 6.2) and therefore only a small bowing of the SBR mirror (i.e., a large negative R) results. As w increases, there is, however, a rapid increase in $|1/R|$ that results from the w^2 scaling of the average incident (intracavity) laser power. This power has a maximum possible value, neglecting nonlinear absorption, of $\frac{3}{2}\pi w^2 R_{\text{rep}} F_{\text{sat}} (\Delta R_S + \Delta R_{NS})$. When the spot size is larger than $w \approx 50\mu\text{m}$, the radius of curvature becomes nearly constant at $R = -20(\pm 5)\text{m}$. The minimum value of $|1/R|$ occurs in the vicinity of a $200\mu\text{m}$ laser spot size. This is attributable to the restricted transverse heat conduction as well as the influence of the edge at $r = a$ on the deformation (Figure 6.3).

It is interesting to note that while the defocusing strength of the deformed SBR mirror increases for small w , the aberrations relative to the equivalent spherical mirror decrease. In fact, the quantity $|8c_2 R^3/3|$ falls by three orders of magnitude as the laser spot size increases in value from $10\mu\text{m}$ to 1mm . Even so, that the values of this ratio range from 10^9 and 10^{13} clearly signifies that spherical aberrations in the SBR mirror are not

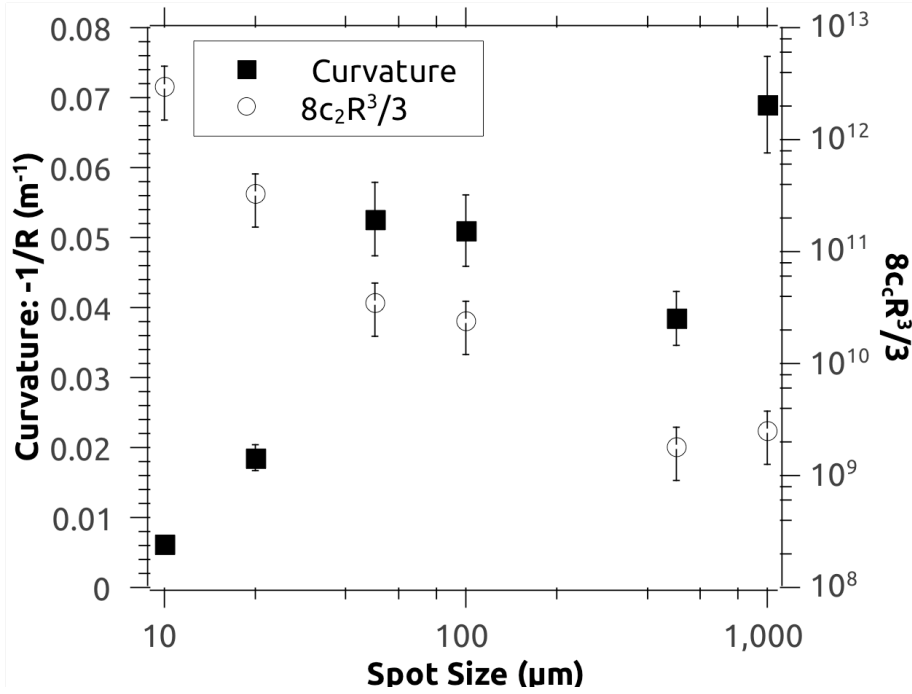


Figure 6.4 shows the magnitude of $1/R$ and the $8c_2R^3/3$ ratio as a function of laser spot size, w .

negligible. In fact, these laser-induced thermal deformation aberrations may dominate the spatial optical aberrations in a passively mode-locked laser resonator. It should be noted that the error in evaluating the $|8c_2R^3/3|$ is substantial. It is possibly greater than 50%. This large error is the result of the $\pm 10\%$ error in extracting a value for R as well as a somewhat larger error in determining the polynomial expansion coefficient c_2 . Consequently, only the strong decreasing trend present in the relative aberration with w should be noted.

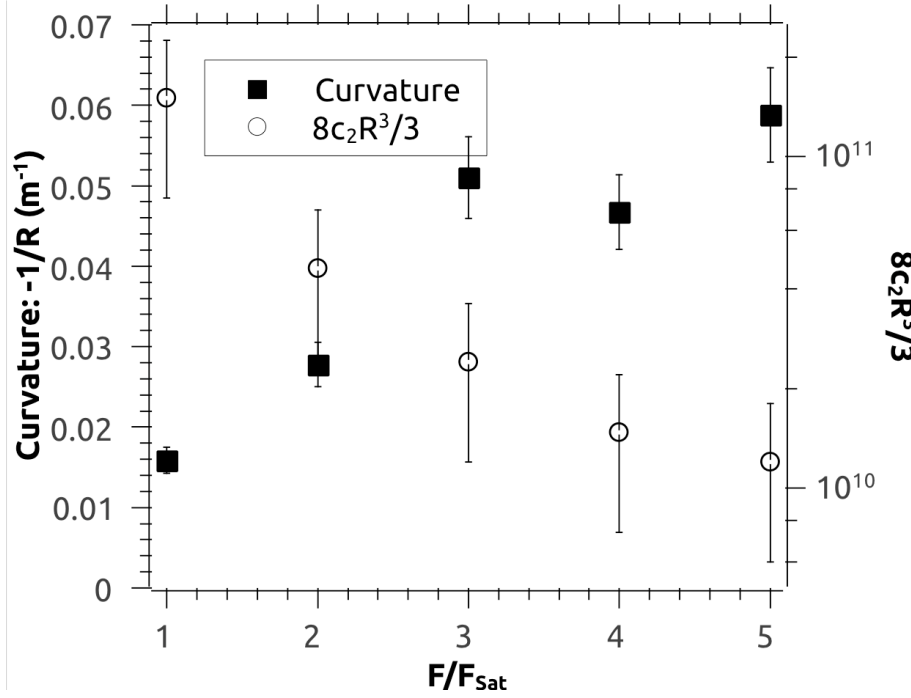


Figure 6.5 shows the variation of the magnitude of $1/R$ with respect to the value of the F/F_{sat} ratio.

It is also worth noting that the thermal deformation, and thus the lensing properties, of the SBR are also a function of the F/F_{sat} ratio. Figure 6.5 shows that the variation of the magnitude of $1/R$ with F/F_{sat} for a 100MHz mode locked laser with $w = 100\mu m$ incident on the $d = 400\mu m$, $a = 2mm$, $\Delta R_s = 0.8\%$, $\Delta R_{NS} = 1.2\%$ SBR. Figure 6.5 indicates the magnitude of $1/R$ slowly saturates above $F/F_{sat} \approx 3$. This result is not surprising because above $F \approx 3F_{sat}$ the saturable component to the absorption is already well saturated. This means that only the constant non-saturable absorption associated with ΔR_{NS} has an appreciable contribution to the heat source term. Of course, the relative strength of the spherical aberrations in the SBR mirror is also

dependent on F/F_{sat} . While this may at first be surprising, given that the value of w is held constant, the dependence occurs simply because the effective width of the heat source is changing – it is a function of F/F_{sat} . Another effect evident in Figure 6.5 is that as the incident laser pulse fluence increases from F_{sat} to $5F_{sat}$ the value of $|8c_2R^3/3|$ decreases by nearly an order of magnitude.

The bowing of the SBR for the mode locked laser presented in Chapter 5 was also investigated. In this case, the recombination time of the SBR, $\tau_R \sim 10\text{ps}$ [19], is of the same order as pulse duration (10 – 20ps). This makes utilizing the analysis of the bowing of the SBR presented in this chapter somewhat problematic because F_{sat} , a device specific parameter assumes the pulse duration is significantly less than the recombination time ($\tau_p < \tau_R$) of the SBR. An effective F/F_{sat} value can be calculated for this case (60W of intracavity power, a repetition rate of 60MHz, and a spotsize of $350\mu\text{m}$) and doing so gives a value of 6. However, the mode locking is clearly behaving as if the oscillator is operating near the ‘optimum’ F/F_{sat} value of 3. It is therefore a reasonable approximation to say the saturable absorption in this particular case has been effectively doubled; i.e., because the oscillator is operating in the regime where $\tau_R \approx \tau_p$, some of the excited electrons in the quantum well of the SBR will recombine with holes during the laser pulse duration and can then be re-excited. An

analysis of the bowing of the SBR for the laser system presented in Chapter 5 using this approximation results in a radius of curvature of $R = -6\text{m}$. This result is 25% off of the expected value of $R = -4.5\text{m}$ (calculated by knowing the SBR was moved in 3cm from the position of the flat mirror). Given that there is an estimated 10% error in extracting the value of R and that this mode locked oscillator is operating in a regime where the effective value of F_{sat} is not known, this is a reasonable result.

The SBR substrate thickness d [19] is another parameter that can be varied. Figure 6.6(a) shows the dependence of $|1/R|$ as a function of d for three different laser spot sizes ($w = 10\mu\text{m}$, $100\mu\text{m}$, and 1mm). These results are for the canonical SBR with $a = 2\text{mm}$, $\Delta R_s = 0.8\%$, and $\Delta R_{NS} = 1.2\%$ SBR, for $F = 3F_{sat}$. The results clearly indicate that the role played by substrate thickness in determining the thermal focal strength of the SBR is only very minor. In contrast, the role played the incident laser spot size is considerably greater (as shown in Figure 4). The thickness of the SBR does however appear to have a significant influence on the optical aberrations of the saturable reflector. The relative quartic aberration coefficient, $|8c_2R^3/3|$, is shown in Figure 6.6(b) for the same set of cases presented in Figure 6.6(a). It is interesting to note that for the smallest $10\mu\text{m}$ laser spot

size (circles), the optical aberrations are evidently independent of d .

This result is expected because the rapid transverse heat conduction

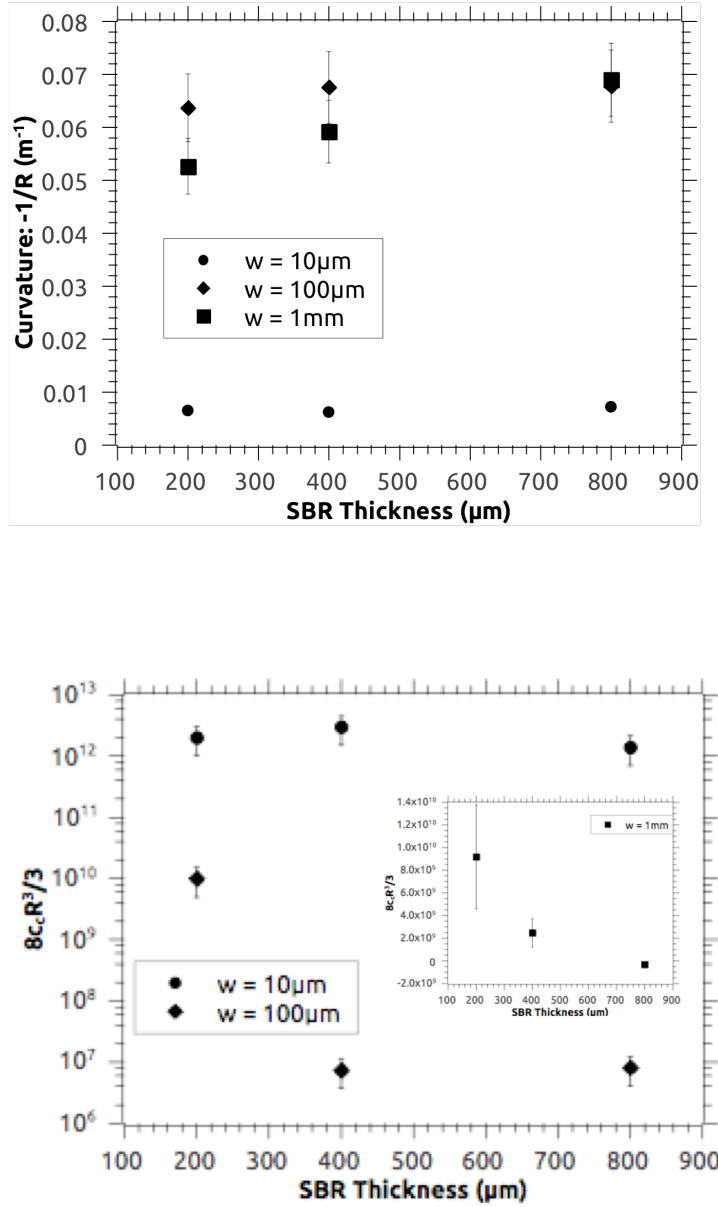


Figure 6.6(b) shows the relative quartic aberration coefficient, $|8c_2R^3/3|$ as a function of SBR thickness for three different spot sizes. Note the value for $w = 1\text{mm}$, $d = 800\mu\text{m}$ is negative.

results in the temperature $T(r = 0, z)$ dropping very close to that of the Cu cooling block within $100\mu\text{m}$. This $100\mu\text{m}$ distance is less than all the considered values of d . In contrast, for the $100\mu\text{m}$ laser spot size, the optical aberrations of the SBR mirror dramatically increase for substrate thicknesses less than $400\mu\text{m}$. Again, the cause can be traced to the variation of $T(r = 0, z)$. In this case, the temperature undergoes a 90% drop from the peak temperature $T(0, 0)$ in the first $200\mu\text{m}$ of the SBR (see Figure 2). As a result, the effect of the back surface is not strongly decoupled for $d = 200\mu\text{m}$. For the case of the largest 1mm laser spot size, the trends in $|8c_2R^3/3|$ with respect to thickness, d are different from those of the two smaller incident laser spot sizes. This is very likely due to the influence of the outside edge of the SBR (at $r = a$) on the deformation. Interestingly, these simulations indicate that the relative spherical aberration changes sign for $d = 800\mu\text{m}$. This suggests it may be possible to engineer a SBR that has near zero quartic spherical aberration. However, it is beyond the scope of this particular analysis to do a thorough investigation aimed at optimizing the conditions such as the spot size to SBR thickness (w/d) and spot size to SBR radius (w/a) ratios, to minimize the optical aberrations in an operational SBR.

7. HIGH-RESOLUTION, LOW-ABERRATION SPECTROGRAPH

7.1 Introduction

In the early years of laser technology, laser pulse characterization was accomplished by calculating the time bandwidth product, $\Delta\nu\Delta t$. In this old method, the spectral components of the pulse, $\Delta\nu$, are measured independently from the pulse duration by a spectrometer. Measuring the pulse duration of a laser can be difficult because the pulses are often shorter in time duration than the fastest available photodiodes. In these instances, the laser pulse is often used to measure itself by performing an autocorrelation (Figure 7.1), as is employed in Chapter 5. In this technique, a pulse is split into two separate pulses using a beam splitter, sent down different paths and recombined in a second harmonic crystal or other nonlinear material. One of the pulses is then scanned in time across the other pulse by changing the path length it travels. When the two pulses are overlapped in time, a signal is generated. The strength of generated signal is proportional to the amount of pulse overlap and is measured by a photodiode; the highest second-harmonic intensity is then generated when the peaks of the pulses are aligned.

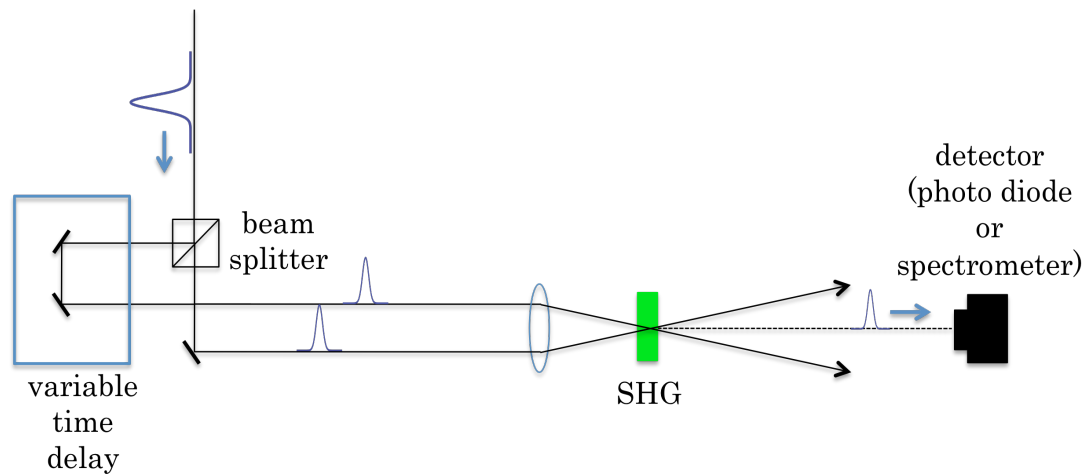


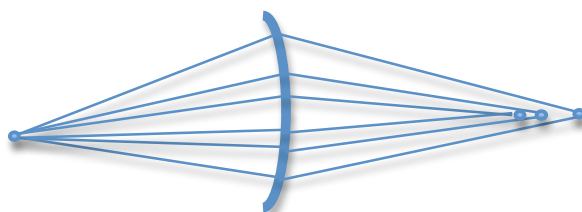
Figure 7.1 shows the optical layout for an autocorrelator which uses a spherical lens for the focusing element and a photo diode as the detector. Replacing the spherical lens with a cylindrical lens and the photo diode with a spectrometer results in the ability to make FROG measurements.

More recently, the preferred method of laser characterization is to perform a frequency resolved optical gating (FROG) measurement [115]. A FROG measurement, which can be thought of as spectrally resolved autocorrelation measurements, gives both phase and electric field information about the laser pulse, whereas autocorrelations wash out the phase information and show only an intensity profile. The additional phase information contained in a FROG measurement is acquired using a spectrometer for each piece of the time scan; i.e., the light from the SHG is collected directly into a spectrometer where the spectral components of each time slice of the pulse are revealed. A recursive algorithm is then used to translate the many spectra into a reconstruction of the pulse's electric field (amplitude and phase).

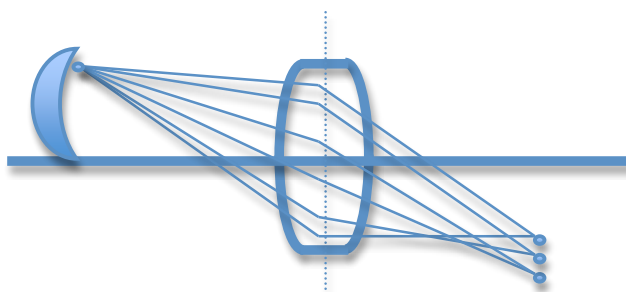
The most challenging aspect of building a FROG for use with picosecond pulses is obtaining a spectrometer capable of resolving the time details of a pulse that has a transform limited bandwidth of $\sim 0.1\text{nm}$ over the aberration-free detection area suitable for a CCD camera. A literature search found a proposed design by Gil and Simon [130] capable of this level of resolution and aberration-free performance. To my knowledge, I am the first to build and characterize this spectrometer design. Section 7.2 describes the optical aberrations that affect spectrometer design and performance. Section 7.3 describes the design of the spectrometer presented in this thesis and also gives a brief overview of the other common spectrometer designs. The alignment processes and characterization of the spectrometer is presented in section 7.4 while section 7.5 shows the spectrum obtained from $\sim 10\text{ ps}$ Nd:GdVO₄ and Nd: YAG lasers.

7.2 Aberrations

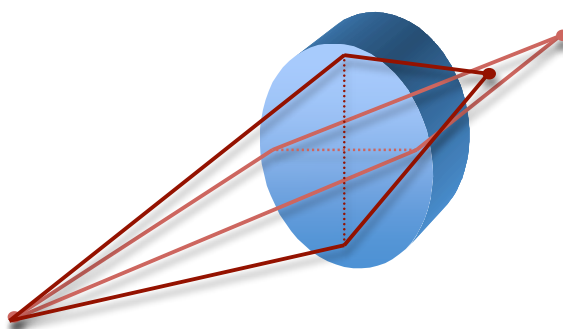
The quality of the spectrograph's image will be effected by the Seidel aberrations which include spherical aberration, coma, astigmatism, field curvature, and distortion [134]. Spherical aberrations result from the radial variation of the focal length of optic. That is, the rays further out 'see' a different focal length than those at the center of the optic (Figure 7.2 top). In



Spherical aberration



Comatic aberration



Astigmatism

Figure 7.2 Graphical representations of spherical aberration (top), coma (middle), and astigmatism (bottom).

spherical aberration all of the focal lengths lie on the optical axis. Parabolic optics are considered to be ‘perfect’ and do not induce spherical aberrations.

Their use, however, can result in other aberrations. The transverse equivalent of spherical aberration is comatic aberration, or coma; i.e., the non-central rays are focused to different tangential positions at the focal plane, as shown in Figure 7.2 (middle). As a result, a circular object whose image experiences large amounts of coma will appear conical in shape. A common method for compensating for coma is to use two, symmetric off-axis elements set up so that coma added by one element is subtracted by the other. Astigmatism is another aberration and describes the phenomenon that occurs when the focal point for the orthogonal tangential and the sagittal planes differ (Figure 7.2 bottom). Astigmatism often results from optical elements that are at a non-normal angle to the incoming rays. Petzval field curvature occurs when the image ‘plane’ is not actually a plane, but rather a curved surface [134]. The image from any optical system will have inherent aberrations, however misalignment of optical elements will exacerbate these. As a result, the realization of the imaging potential of any spectrograph requires precise alignment of the mirrors and gratings.

Several plane-grating spectrograph designs are worth mentioning. The Czerny-Turner [119, 120] is perhaps the most common spectrograph design and is shown at the top of Figure 7.3. The two-mirror (collimating and camera), symmetrical Czerny-Turner design is geometrically identical to the single spherical mirror Ebert spectrometer [121], shown as the middle diagram of Figure 7.3. This design was first proposed in 1889 and successfully re-introduced by Fastie in 1952 [122, 123]. The latter spectrometer became a primary spectral diagnostic in space

exploration due to its simple and rugged single-mirror design [124]. Both of these Z-configuration spectrometers compensate for off-axis comatic aberration [125, 126], but suffer from astigmatism and spherical aberration due to the use of off-axis spherical optics. Spherical aberration can be removed by employing parabolic focusing optics – such as in the parabolic Ebert design [121, 123, 124]. However, in contrast to their spherical-mirror counterparts, the comatic aberration adds in parabolized Z-configuration spectrometers. This realization led to the development of *U*-configuration designs with off-axis parabolic mirrors, the Hill [127] and Chupp-Grantz [128] monochromators (shown in Figure 7.3 bottom), in which the reversal of the angular direction of reflection from the camera mirror cancels coma. Unfortunately, these latter two high-quality planar monochromator designs may still not be suitable for use as high-resolution spectrometers that employ precision plane gratings and today's large-area, state-of-the-art CCD detectors. The primary cause for concern is the cylindrical deformation of the image plane resulting from the fact that the image distortion due to the tilted grating in the dispersion plane adds to the residual Petzval field curvature [129] in the tangential plane of the off-axis parabolic mirror. The latter field curvature is stronger than that in the sagittal plane since the off-axis distance is in the tangential plane.

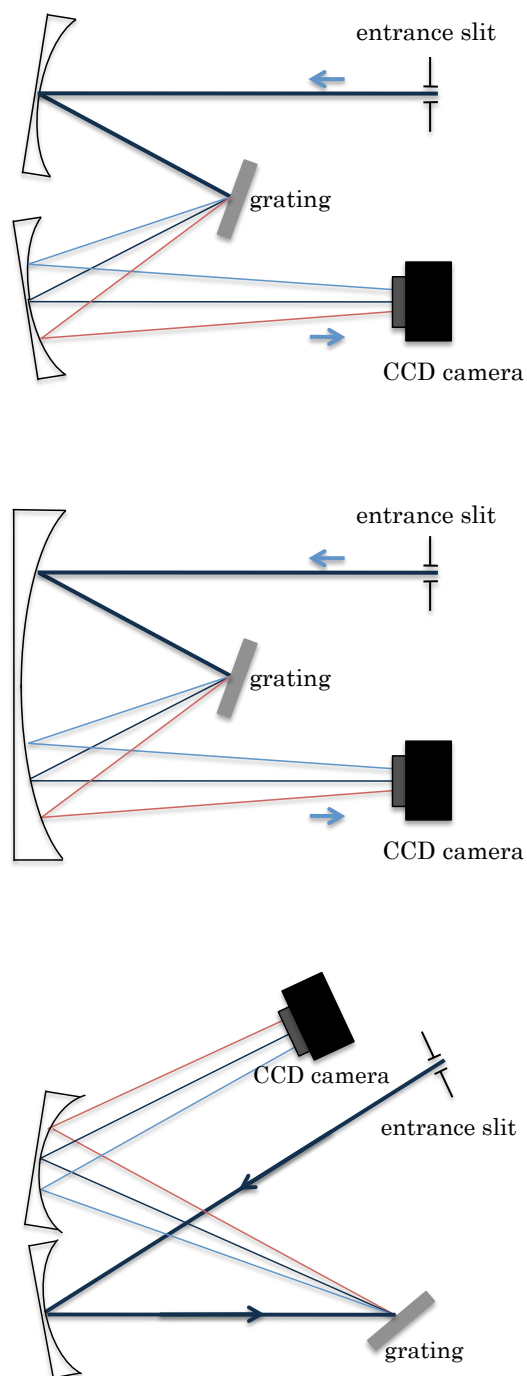


Figure 7.3 Graphical representations of a Czerny-Turner spectrometer (top), an Ebert spectrometer (middle), and a Hill spectrometer (bottom). Both the Czerny-Turner and the Ebert have a z-shaped configuration (the entrance and exit slits are on opposite sides of the grating) while the Hill has a u-shaped configuration (the entrance and exit slits are on the same side of the grating).

7.3 Spectrograph Design

The aberration-corrected, flat-field, plane-grating spectrometer presented here was first proposed by Gil and Simon [130] in 1983. While most common spectrograph designs are planar [119-128], the most distinctive feature of this plane-grating spectrograph, shown in Figure 7.4, is that the grating does not lie in the plane which is defined by the entrance slit, the exit slit, and the centers of the two off-axis parabolic focusing mirrors. Instead, the grating is positioned out of the plane. It is located above the common focal point (O) of the two focusing mirrors in the unfocused or collimated portion of their optical arrangement; the vertical displacement of the grating is perpendicular to the dispersion plane of the grating. The incident light is transmitted in through the entrance slit (S) and onto the collimating mirror (P1) -- all of which are in the horizontal plane. The light is then directed upward, out of the plane, and onto the grating located at the focus of the collimating mirror. The reflection grating then disperses the light back down that same angled plane onto the second off-axis parabolic mirror (the camera mirror (P2)) which of course focuses the light and also redirects it back into the original horizontal plane and onto the CCD camera. The off-axis parabolic collimating and camera mirrors used in this design eliminate spherical aberrations [127, 128, 130]. As a result only astigmatism, coma, and field-curvature can contribute to the aberrations in the resulting image.

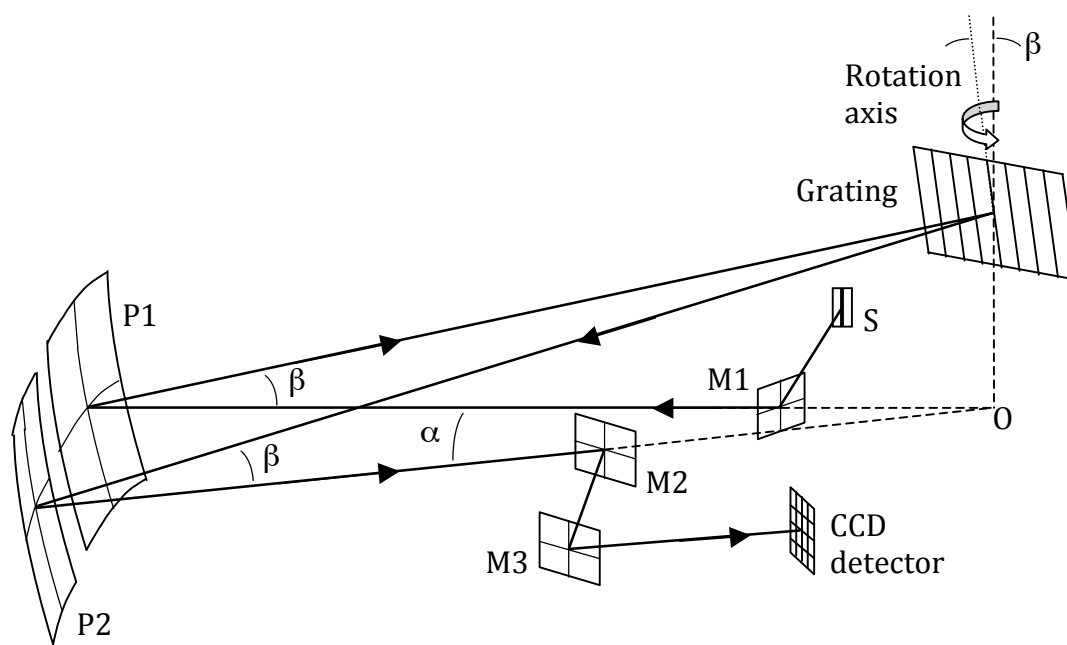


Figure 7.4 shows a diagram of the spectrometer. *S* labels the entrance slit to the spectrometer. *P1* and *P2* are the off-axis collimating and camera mirrors. *M1*, *M2*, and *M3* are flat mirrors used to direct the laser beam. The grating is out of the plane defined by the other optical elements.

In principle, the grating position may be at any arbitrary distance from the collimating and camera mirrors in the collimated light path. However, the $f2ff$ (or $4f$ total distance) optical arrangement shown in Figure 7.4 which places the entrance slit and CCD imaging camera at the foci of the two off-axis parabolic mirrors and the grating at the other common ‘focal plane’ of

these off-axis parabolic reflectors is utilized because Gil and Simon [130] showed that this arrangement has the least image aberration. Indeed, the plate analysis of Gil and Simon [125, 126, 130-133] for our spectrograph employing $f = 40$ inch (1016 mm) mirrors predicts a field curvature which deviates from a perfect flat field (over a central 13x13 mm image area centered on the optical axis) by less than 3 nm. This impressive theoretical result shown in Figure 7.5a was calculated for a visible wavelength of 579 nm (yellow) light and a long 15 mm entrance slit length. This result indicates that figure of the optics used in the spectrograph and the alignment of optical elements will solely determine the quality of the image of the entrance slit. In fact, the dominant aberration, Petzval field curvature, will contribute less than a $\sim \lambda/100$ piston error (relative to a perfect flat image) in the visible over the 13.3 x 13.3 mm active area of the CCD camera; in this case, a high quantum efficiency, high resolution, detector with a back-thinned Marconi array of 1024 x 1024, 13 μ m-square pixels (Finger Lakes Instrumentation, model MaxCam CM2-1).

In theory, the use of longer slit lengths will significantly increase the piston error in the image plane. This is because longer slits introduce more off-axis rays. However, even when the calculations are evaluated for a long 7 cm slit length, the plate analysis of Gil and Simon [130] still predicts an extremely small deviation (less than 40 nm) from a perfect flat field for the 13x13 mm CCD image area. As expected, for slit lengths smaller than the

13.3 mm CCD dimension, the analysis of Gil and Simon [130] indicates that the field curvature orthogonal to the grating dispersion plane is further reduced; in fact, the spectrometer produces almost perfect 1:1 images of such slit.

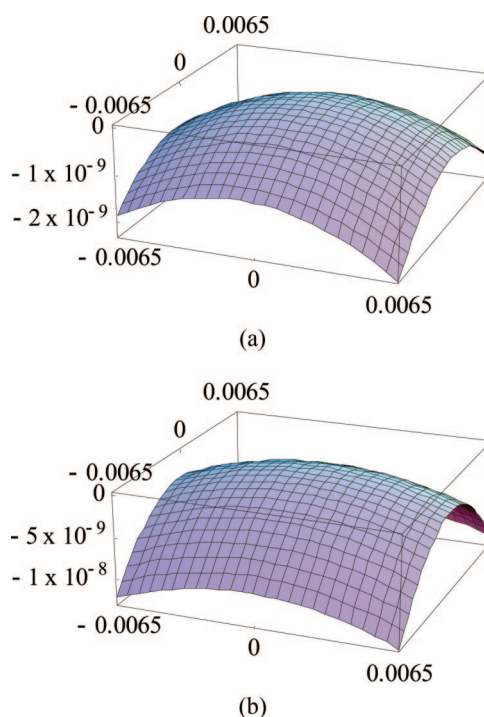


Figure 7.5 (a) shows theoretical wavefront piston error over the central 13mm x 13mm portion of the image plane of the $f/10$ ($f=1016$ mm) spectrograph. This figure was calculated using $\lambda = 579$ nm for a 15 mm entrance slit. Figure 7.5 (b) shows an equivalent calculation for $f/5$ ($f= 508$ mm). The units of all axes are meters.

Figure 7.5b shows the predicted distortion over the same 13 mm x 13 mm image area for an equivalent $f/5$ spectrometer also with a 15 mm

entrance slit at 579 nm; i.e for a spectrometer with the angles α and β doubled (Figure 7.4), as is necessary to assure an $f/5$ numerical aperture for $f = 508$ mm. This theoretical result shows the maximum piston error, which is primarily due to residual field curvature [130], increases to approximately 12 nm. The factor of 4 increase in field curvature is concentrated in the dispersion plane of the grating. In the plane orthogonal to the grating dispersion, the maximum piston error is approximately the same as that for the $f/10$ spectrometer.

It is interesting to note that the data in Figure 7.5 indicate that the image-plane performance of the $f/10$ spectrometer based on the design by Gil and Simon [130] is somewhat superior to an equivalent $f/5$ instrument. In practice however, it would be difficult to position the CCD camera with sufficient accuracy (~ 1 nm) to determine the difference. The availability and cost of suitable optics are actually more important design criteria. Of course, to investigate the time-frequency characteristics of picosecond laser pulses [2], it is necessary for accurate spectral pulse diagnostics to disperse the ~ 0.1 nm spectral over at least 100 of the $13\text{ }\mu\text{m}$ pixels. In order to improve the signal-to-noise, the spectra should be measured in the first-order. To attain these requirements, an off-axis parabolic mirror with focal length of greater than 0.5m and a typical 1000 – 3000 lines/mm groove density grating must be used. Furthermore, the minimization of aberrations such as coma requires the collimating and camera mirrors be identical. To achieve this, the off-axis

parabolic mirrors were cut from a single uncoated, 8-inch-diameter, $f/5$, axial parabolic mirror (Edmund Industrial Optics, model E32-073-000). This optic was first cut by CVI Laser Corporation in half across its diameter. Next, the 2 inch ends of each semicircle were removed, resulting in two roughly square 4x4 inch $f/10$ off-axis parabolic mirrors that are nearly identical. A protective silver coating with a $>90\%$ reflectivity for the visible and near infrared was then applied by CVI Laser Corporation to the $\lambda/8$ (at 632 nm) polished surfaces. The ~ 30 mm thickness of the original optic ensures that the cutting process did not significantly affect the optics' surface figure.

To assist in accurately aligning the spectrograph, the two parabolic reflectors are each mounted on a precision tilt and rotation stage (Newport Corporation, model 37). As shown in Figure 7.4, the centers of the optics are separated by about 15 cm in the horizontal plane. As a result, the angle α between the central rays from the entrance slit and to the CCD camera is 4.2° . The angle subtended between the incident and reflected rays on the grating is also this same angle, α . Three pick-off mirrors with protective silver coatings (Newport Corporation) are used to separate the incident and detected radiation at the common focal point and to allow the grating to be easily positioned. One 1-inch-diameter mirror directs the incident light from the entrance slit onto the collimating mirror, while two 2-inch diameter mirrors direct the spectrally-dispersed radiation onto the CCD camera. To assist in accurately positioning the CCD camera at the focal plane of the

spectrograph, a precision tilt and rotation stage (Newport Corporation, model 36) is also employed. It is particularly important to be able to rotate the 1k×1k image area about the central incident ray. This allows one axis of the CCD array to be accurately aligned with spectral dispersion from the plane grating.

The choice of grating is of course determined by the required spectral resolution and wavelength range of interest. For use in frequency-resolved optical gating (FROG) techniques [2] for picosecond pulses in the near IR and visible a rectangular 50x100mm, high-modulation, plane holographic grating that has a groove spacing of 1500 lines/mm and a protected silver coating was selected. This grating (Spectra-Physics, Richardson Grating Laboratory, catalog no. 53114BK06-239-H from master 5338) is mounted on a rotation stage (Newport Corporation, model 481-A) such that the rotation axis of the grating is both perpendicular to the dispersion plane containing the collimated incident and reflected rays and in the plane of the grating: i.e., the grating rotation axis is at $\beta \approx 2.8^\circ$ to the vertical (Figure 7.4).

This aberration-corrected, flat-field, $f/10$ spectrograph fits nicely on a 1x4 ft. breadboard (Newport Corporation, model RG-14-2) and is encased in a light-tight enclosure. Additionally, two light baffles are employed. The first ~30cm long baffle is placed between the off-axis parabolic mirrors to stop optical cross-talk between the collimating and camera sides of the spectrograph. The second is an appropriately sized rectangular baffle that

restricts the view of the CCD camera to the image directly focused by the parabolic camera mirror (P2). Three different precision, Cu-Be entrance slits from National Aperture, Inc. were obtained. The first slit has a length of 15mm and is 25 μ m wide. The second slit has a length of 3mm and is 5 μ m wide. While the third slit has a length of 3mm and is 10 μ m wide. Each slit is mounted in a rotation stage (New Focus, model 9401) which allows the slits to be aligned exactly vertically. Additionally, this mount allows the planar imaging performance of the spectrograph to be optimized in zero order (by replacing the grating with an equivalent mirror) over an entire 15mm-diameter entrance-slit plane.

7.4 Alignment and Performance

The essentially aberration-free performance of this spectrometer is critically dependent on the accuracy with which the optical elements are aligned. Of particular importance is the alignment the two off-axis parabolas such that their foci are exactly coincident on the grating. This was accomplished with the use of a slit, a He-Ne alignment laser, and a silvered mirror (identical in size to the grating) positioned in the grating mount. The following steps were taken:

1. First the collimating mirror (P1) is positioned a distance f from the entrance slit (S). The positioning is correct when the diffraction pattern from slit is collimated.

2. Next the grating must be placed a distance f from the collimating mirror. This is done by replacing grating with a plane mirror of the same dimensions. The image is then retro-reflected back to the slit in order to verify 1:1. The positioning is correct when then reflected image is an exact replica of the slit.

3. The camera mirror (P2) also needs to be exactly a distance f from the grating. This is accomplished by rotating the plane mirror that is serving as the placeholder for the grating onto the camera mirror. The slit diffraction pattern on this mirror should be an exact replica (at the same height and of the same dimensions) as that on the collimating mirror (P1). The reflection off this mirror (P2) and towards the CCD camera should be at the same height as the height as the slit/P1 path (i.e., the angles β are the same).

4. A plane mirror is placed at the position of the CCD camera to reflect the light back through the spectrograph. This positioning of this mirror is correct when the reflected light reflects back through the optical again produces an exact replica of the slit.

5. Finally, the grating and the CCD camera replace the alignment mirrors.

After the spectrometer was aligned, its performance was investigated using Hg, Ar, and Kr spectral lamps. With the 15mm long, 25 mm wide entrance slit, measurement of the well-known yellow Hg doublet (576.960 and 579.066nm; $\Delta\lambda = 2.106\text{nm}$), shown in Figure 7.6, resulted in an image plane doublet separation of 277 13 μm pixels. This corresponds to a spectral dispersion of $7.60(\pm 0.02) \times 10^{-3}\text{nm}$ per 13 μm pixel with the 1500 lines/mm grating. This value is consistent with the expected value of $0.59\text{nm}/\mu\text{m}$.

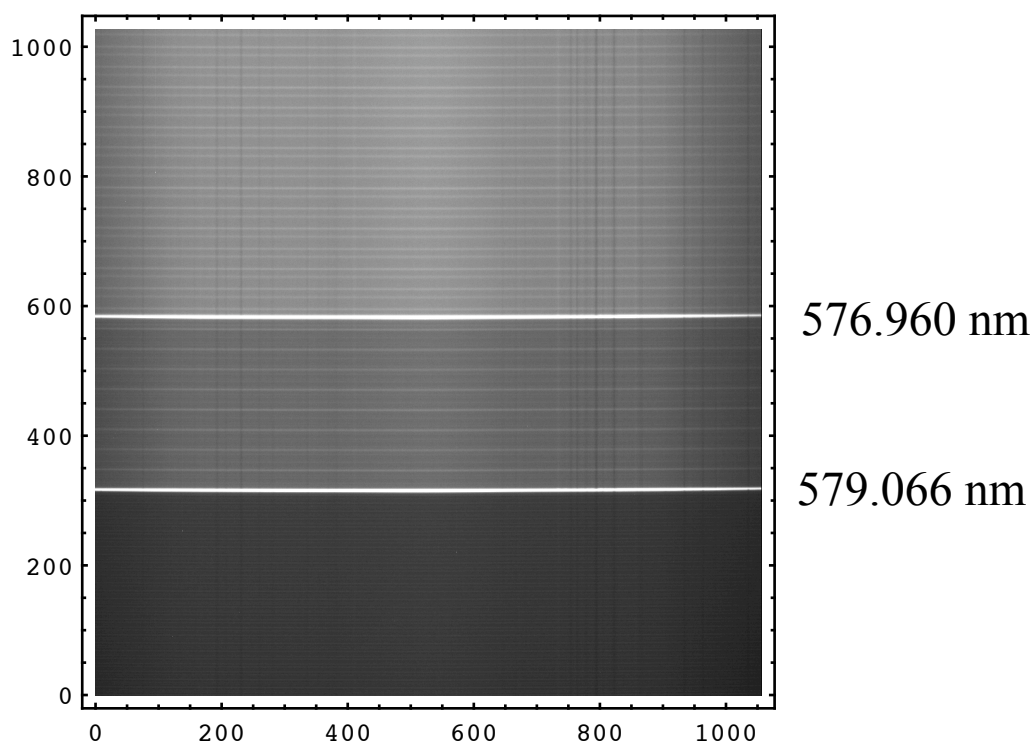


Figure 7.6 shows the raw Hg doublet CCD image.

The spectral lines also display almost insignificant curvature, or smile error, over the entire 13.3 mm x 13.3 mm image plane as measured by the flat CCD camera -- indicating near-perfect flat-field imaging. Figure 7.7 shows the background-subtracted lineouts of the Hg 579.07nm spectral line integrated, in the direction perpendicular to the spectral dispersion, over five sections of 50 pixels across the 1024 pixel wide CCD camera. The Gaussian fits made to the integrated lineouts reveal that the spectrograph has ~1 pixel of smile error across the entire 1024 pixel image field. The imaged spectral line is approximately three 13 μ m pixels wide; that is, it has a FWHM of approximately 1.5 x the 25 μ m entrance slit width. This means the curvature error is significantly less than the width of the line image. A smaller curvature error is expected for shorter wavelengths since a contribution to this aberration is the difference in path length between the ends of the tilted, near Littrow grating which is reduced as the wavelength decreases. Upon investigation, the blue 434.75nm Hg spectral line exhibits equivalent smile error to that presented in Fig 7.7; that is, a wavelength difference in the curvature error of the two spectral lines could not be determined.

The spectral keystone error, or variation of the image width in the dispersion direction, was also investigated: there is no observable variation in the spectral line width across the ~8nm spectral width that corresponds to the one dimension of the 1024 pixel CCD camera. The first-order image

widths of the Hg 434.75nm, Hg 579.07nm, and Kr 760.15nm spectral lines were all 3 to 4 pixels at FWHM for the 25 mm entrance width. To further investigate this error, the entrance slit was turned horizontal (rather than its normal vertical position), and the entire image was observed to have the same ~ 3 pixel image width. This result in conjunction with that for the smile error are consistent with the theoretical aberration analysis which predicts

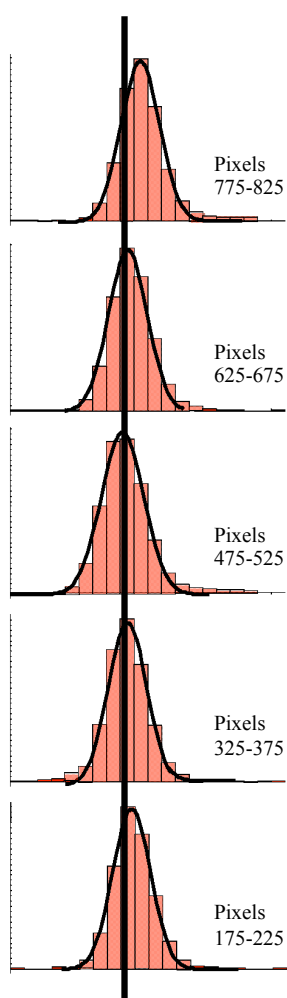


Figure 7.7 Evaluation of the smile error of the $f/10$ spectrograph using correctly registered background-subtracted lineouts of the Hg 579.07 nm spectral line integrated over five sections of 50 pixels across the 1024 pixel wide CCD image.

that any aberrations present cannot be resolved with this CCD camera's 13 μm pixel size. The $\sim 60\%$ broadening of the 25 μm entrance slit to an $\sim 40 \mu\text{m}$ image must be caused by finite $f/10$ aperture of the spectrometer (the mirrors and gratings are all finite in size and thus function as apertures), errors in the surface figure of the optics and their surface roughness, and possibly optical alignment error.

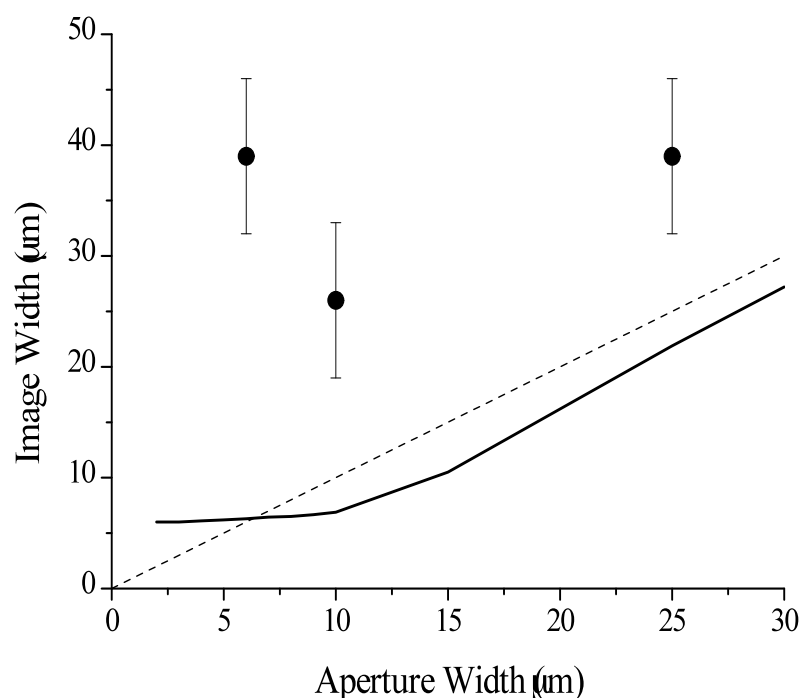


Figure 7.8 Measured FWHM image widths of the first-order 579.07 nm Hg spectral line as function of the entrance slit width a . The FWHM image width variation predicted by a diffraction analysis with perfect optics is plotted as the solid curve. The dashed line indicates perfect 1:1 imaging.

The finite numerical aperture of the spectrograph and imperfections in its optical elements are expected to determine the optimum slit width at any given wavelength. Figure 7.8 plots the FWHM image widths of the $\lambda = 579.07\text{nm}$ yellow Hg line as recorded by the CCD camera for the 5, 10, and $25\mu\text{m}$ entrance slit widths. Clearly a slit width of $10\mu\text{m}$ is optimal for this spectral region. Included on Figure 7.8 as a solid line is the expected diffraction limited FWHM image width. These theoretical line widths are obtained using a Fourier diffraction analysis of the spectrometer's optical system. It is notable that the theoretical image width is less than the entrance slit for apertures greater than $7\mu\text{m}$. This is likely due to determining the customary FWHM rather than correctly evaluating the image width from the spatial variance. A comparison of the measured image widths with the theoretical values of all of the finite apertures clearly demonstrates the influence of errors in the polish, surface figure, and possibly the alignment of the optics. The most dramatic difference occurs for entrance slits less than $10\mu\text{m}$ where the measured image width increases rapidly; in contrast to the diffraction theory results, but consistent with analyses of spectrographs with residual optical errors [125-133].

The optimum entrance slit size of $a = 10\mu\text{m}$ corresponds to the case corresponding to when the acceptance aperture of the optical system is just able to capture the entire central peak of the sinc^2 pattern generated by the slit. That is, it corresponds to the condition when $a = 2\lambda(f/\#)$, where $f/\#$ is the

f /number of the spectrometer. For slits smaller in width, more of the off-axis figure error is collected and transmitted to the image, leading to a broadened real image. The larger slits have a diffraction pattern that is more concentrated near the optical axis and therefore accumulate less off-axis figure error resulting in a measured image width much closer to the theoretical value. This means for a spectrum centered at $\sim 1\mu\text{m}$ (500nm) the ideal entrance slit will be about $20\mu\text{m}$ ($10\mu\text{m}$). However, this analysis ignores the quality of the polish on the optical elements. For reflections off a total of 6 reflections (two parabolic mirrors, three pick-off mirrors, and a grating) all having a $\lambda/8$ to $\lambda/10$ polish at 633 nm, an rms phase distortion of $\lambda/2$ will be generated in the blue whereas the same optics at $1\mu\text{m}$ will produce about half of this error. For the longer wavelengths, diffraction and aperturing effects should be the dominant contribution to image broadening. Convolution of a phase distortion of $20 - 30\mu\text{m}$ with the diffraction limited widths (shown by the solid line in Figure 7.8) is consistent with the observed image widths for both the 10 and 25 mm slits. Of course, optical alignment error will also broaden the image.

Finally, the resolving power of this plane-grating spectrometer was tested by measuring the seven violet spectrum lines of Ar(I) at approximately 420 nm using the 10 mm slit width. Figure 7.9 displays this first order diffraction data obtained using a 1500 lines/mm grating. The ~ 2 pixel slit image width allows for the clear resolution of the Ar doublet at 419.07 nm

and 419.10 nm ($\Delta\lambda = 0.03$ nm) with a separation of ~ 4 pixels. This implies a resolving power, $\lambda/\Delta\lambda$, of $2.5(\pm 0.5) \times 10^4$ in the visible (0.015 nm for the 2 pixel image width). This measurement is taken near the short wavelength limit of the spectrometer – the protected silver coatings are only 70% reflective (at normal incidence) at 420nm.

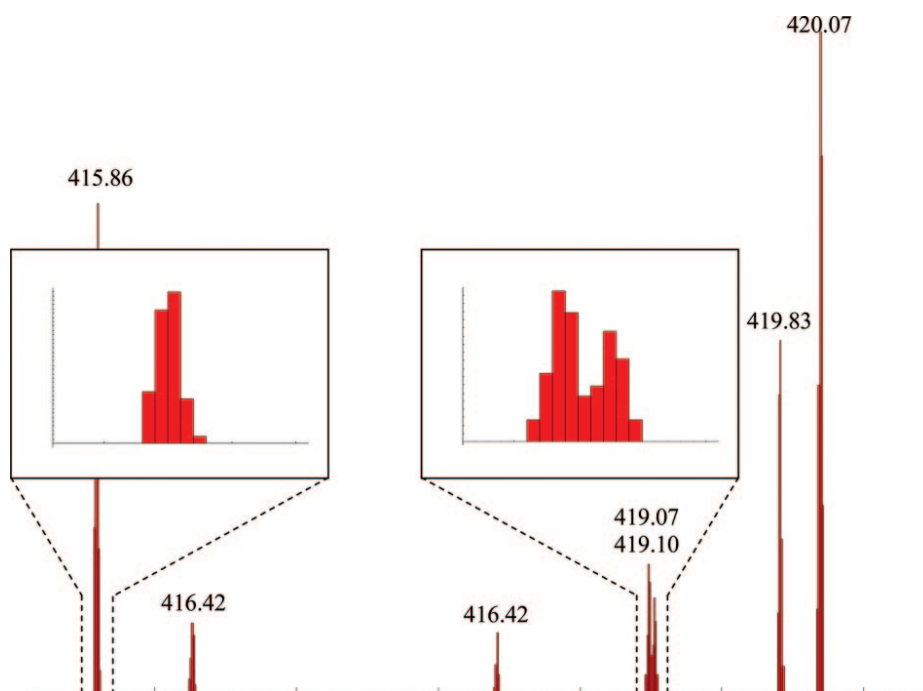


Figure 7.9 Ar(I) emission spectrum between 415 and 429 nm in first order. The weak doublet lines at 419.07 and 419.10 nm are clearly resolved owing to the ~ 2 pixel image width (see inset for the 415.86 nm line) of the 10 μm entrance slit.

7.5 Picosecond Laser Spectrum

This high-resolution spectrometer with great image quality was constructed to resolve picosecond laser pulses. Figure 7.10 shows the spectrum from the Nd:GdVO₄ (blue) oscillator at 1062.9nm as well as spectrum from a Nd:YAG (red) amplifier at 1064.2nm. These two emission lines are well documented and can be used to find the resolution in the near IR to be 0.0059nm per 13 μ m pixel. It is interesting to note that the Nd:YAG spectrum was taken just above threshold and that as a result, not all of the lasing near 1061nm has been suppressed.

The FWHM of the Nd:YAG spectral line shown in figure 7.10 is 17 pixels or 0.1nm wide. It measures slightly larger than 15 pixels or 0.085nm spectral width of Nd:GdVO₄. Although the laser bandwidths of Nd:YAG and Nd:GdVO₄ are generally comparable, the measured difference in spectral bandwidths in this case is not surprising -- the Nd:GdVO₄ laser is mode locked while the Nd:YAG laser is not.

Having measured the spectrum and pulse duration of the passively mode locked Nd:GdVO₄ laser, the time bandwidth product can be calculated and compared to that of the transform limited laser pulse duration, which for passively mode locked pulses us $\Delta\nu\Delta t \geq 0.32$. In the case of the Nd:GdVO₄ 0.085nm spectrum, the bandwidth limited pulse has a duration of 13ps. At this point it is prudent to point out that while one of the autocorrelations

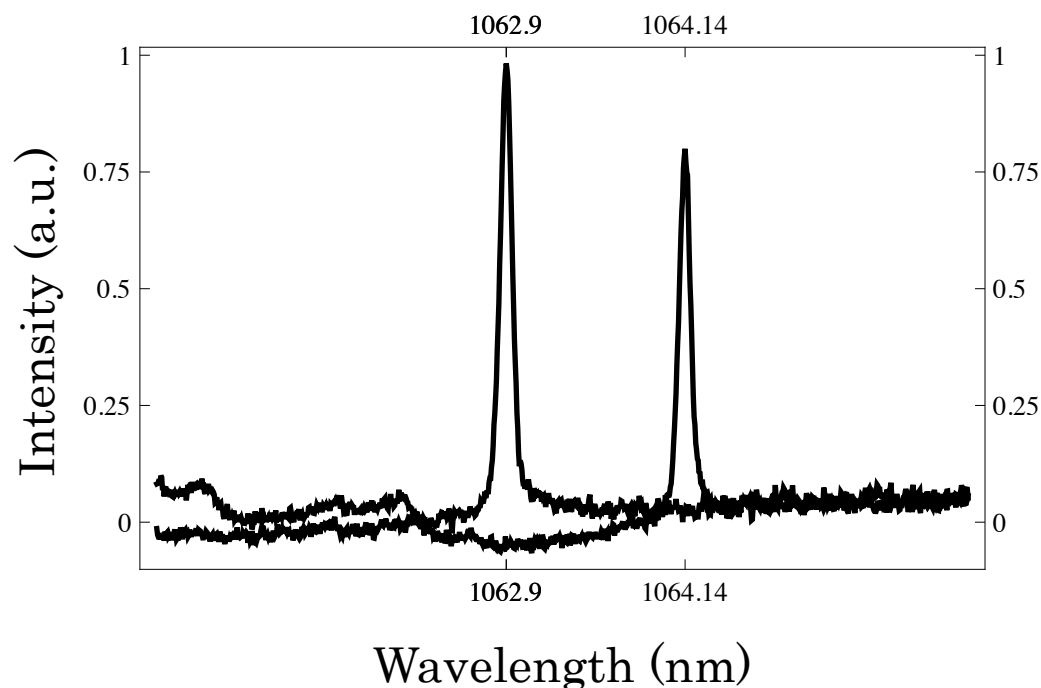


Figure 7.10 shows the 0.09nm FWHM spectrum from the 13 ps Nd:GdVO₄ oscillator at 1062.9nm and the 0.09 nm FWHM spectrum from the unseeded Nd:YAG amplifier at 1064.14nm.

shown in Chapter 5 (Figure 5.3) has a pulse duration of 7.6ps – shorter than is allowed by the above transform limited calculation -- the spectrum shown here was taken from a slightly different laser cavity which had been extended in length to 2.5m to increase the pulse energy. Furthermore, the mode locking, in this case, was optimized for stable operation, not for shortest pulse duration. Additionally, it should be noted the optical properties of this spectrograph are likely good enough that a grating with more lines per mm can be used to stretch the spectrum across more pixels.

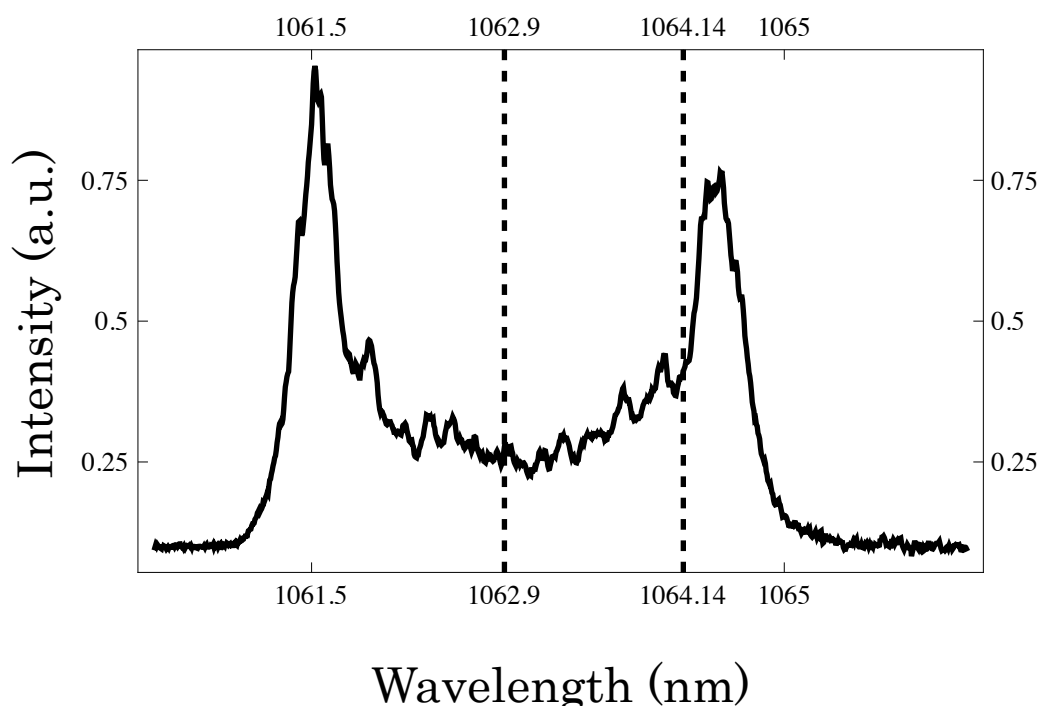


Figure 7.11 shows the broadened spectrum after 0.25W from the Nd:GdVO₄ traverses 60m of single mode optical fiber. The dashed lines indicate the lasing wavelengths of Nd:GdVO₄ (1062.9nm) and Nd:YAG (1064.14nm)

For a specific end-use, it may be desirable to use a regenerative amplifier to achieve pulse energies that are many orders of magnitude (10^4 - 10^6) greater than those of the laser oscillator. In this case, Nd:YAG is often the preferred amplifier material for ps $1\mu\text{m}$ laser pulses because it has a longer upper state life time than Nd:GdVO₄ ($\tau_{\text{Nd:YAG}} = 230\mu\text{s}$, $\tau_{\text{Nd:GdVO}_4} = 95\mu\text{s}$) and thus has a higher energy storage. Figure 7.10 clearly shows emission cross-sections of these two laser crystals do not overlap; thus, without adjusting for this, one cannot be used to seed an amplifier using the other

gain media. One typical solution to this problem of bandwidth matching is to broaden the output of the Nd:GdVO₄ laser by utilizing the nonlinear, SPM effects (described in section 2.5) in single mode fiber. Figure 7.11 shows the spectrum when just 0.25W (at 60MHz) from the 13ps Nd:GdVO₄ is broadened in 60m of single mode, fused silica fiber. The dashed vertical lines indicate the central wavelengths of Nd:YAG and Nd:GdVO₄. Figure 7.11 has the characteristic shape for SPM in a fiber [137] with a linear chirp over the central ~3nm region. This means shorter pulses (~300fs) may be generated using a fiber-grating compressor [138, 139].

8. SUMMARY

8.1 Introduction

This thesis describes the development, construction, and characterization of a high-average power ($\sim 6\text{W}$), $\text{Nd}:\text{GdVO}_4$ laser oscillator that is mode locked using a novel dual-passive mode locking technique to obtain $< 10\text{ps}$ pulse duration. Additionally, the construction and characterization of a high-resolution spectrometer capable of resolving the spectrum of bandwidth limited 10ps laser pulses is described. This laser system can either be used directly or, if desirable, it can be parametrically converted to generate a wide range of frequencies which may be useful for some ultrafast laser spectroscopy experiments. Furthermore, the output power and pulse energy can be amplified making this oscillator useful for some high pulse energy application; e.g., micromachining.

8.2 Laser Oscillator

In Chapter 3 a thermal-lens-shaped, $\text{Nd}:\text{GdVO}_4$ laser oscillator using a Brewster-cut slab laser crystal geometry was presented. The astigmatism introduced by lasing at Brewster's angle to the thermal lens, as well as by other off-axis optical elements, was essentially eliminated by manipulating the shape of

the diode laser pump beam— a technique called thermal-lens-shaping. Integral to this method is a one dimensional heat conduction perpendicular to the direction of laser propagation. This allows the thermal lens generated in the gain media to be easily understood through a simple model and therefore manipulated so that it has an overall stigmatic effect on the intracavity laser beam, resulting in a circular TEM₀₀-mode output beam. The laser cavity, which produced >6W, TEM₀₀-mode output with an $M^2 < 1.2$, can also be readily extended using a telescopic arrangement; for example, to a total length of 2.0m to increase the output pulse energy to increase the possible intracavity pulse energy for mode locking.

8.3 Mode Locking the Oscillator

Chapter 5 describes the simple, dual-passive mode locking technique developed to lower the CW ML threshold as well as to increase the mode locking stability. In this method, an SBR provides the amplitude modulation while a phase mismatched SHG does phase locking. This scheme results in a CW ML critical energy that is more than a factor of two lower than when only an SBR is used; a result that is in good agreement with the theoretical work. Furthermore, it is shown the phase mismatched SHG provides pulse shortening by generating the ‘red’ spectral components that were on the leading edge of the pulse and thereby preferentially absorbed by the SBR. Pulses as short as 7.6ps were generated using

an SBR with $\Delta R = 2\%$ and a 4.9mm BBO crystal operated with a phase mismatch of $\frac{1}{2}\Delta kL = -4\pi$. An investigation into different SHG crystals showed that a large temperature bandwidth is advantageous for stable mode locking. Finally, because the amplitude modulation and the phase locking must be balanced, it was shown that the larger the phase mismatch required to generate the necessary bandwidth for optimal compression, the larger the required modulation depth, ΔR .

8.4 Thermal Effects in the Saturable Bragg Reflector

In order to investigate the observed thermal bowing of SBRs which necessitates a repositioning of this optical element in the laser resonator, an analytical solution to the three-dimension heat equation that results when a laser pulse is incident on an SBR was presented in Chapter 6. The analysis takes into account both the saturable and non-saturable absorption characteristics intrinsic in an SBR. The resulting temperature distributions were shown for two laser spot sizes, $w = 100\mu\text{m}$ and $w = 1\text{mm}$. The strong radial heat conduction for $w = 100\mu\text{m}$ was contrasted with the case for $w = 1\text{mm}$ in which the heat conduction was primarily towards the heat sink (z direction). The thermally induced deformation of the SBR was determined and fit to a polynomial so the properties of the SBR could be easily compared to the focal length of a perfect, parabolic mirror as well as to the aberrations

inherent in a spherical mirror. Investigating the focal length as function of spot size resulted in the discovery that the radius of curvature for incident laser spot sizes larger than $w = 50\mu\text{m}$ were relatively constant. This effect was attributed to the edge effects of the SBR and to the restricted transverse heat conduction for the large spot sizes. In contrast, the spherical aberrations, while considerable for all cases, fell quickly with increasing spot sizes. The effect of F/F_{sat} on deformation resulted in little change as this ratio increases above 3. This of course, is because the saturable absorption is already well saturated for $F/F_{sat} = 3$. Changing the substrate thickness, d , only had a minor role in the resulting radius of curvature. It did however, have a large effect in contributing to the spherical aberration for incident laser spot sizes of $w > 100\mu\text{m}$. Primarily, the $200\mu\text{m}$ thick substrate was shown to have considerable more spherical aberrations than those inherent in the $400\mu\text{m}$ and $800\mu\text{m}$ substrates.

8.5 Spectrometer

A high-resolution, low-aberration spectrograph capable of resolving ps laser pulses was built and characterized. The flat-flat, plane grating, z-configuration spectrometer is most spectacularly differentiated from other designs by its two-dimensional design; i.e., the grating is vertically displaced

from its plane of dispersion. This has the effect distributing the field curvature and coma in two-dimensions, which was shown to significantly limit the aberrations in the image plane. Furthermore, spherical aberration was eliminated by use of parabolic collimating and camera mirrors while minimizing astigmatism by keeping optical elements, other than the grating, at only small angles of deviation from the angle at which they were designed to operate.

The Hg doublet (76.960 and 579.066nm) was resolved to give a resolution of $6.84(\pm 0.02) \times 10^{-3}$ nm per 13 μ m pixel with 1500 lines/mm grating while the $\lambda/\Delta\lambda$ resolution at the UV end of the visible spectrum was shown to be $2.5(\pm 0.5) \times 10^4$. The smile error was shown to be one 13 μ m pixel over the entire 13.3 x 13.3 mm image plane. No variation of the image width in the direction of dispersion was detectable over the entire image area. Finally spectrum for both Nd:GdVO₄ and Nd:YAG lasers were shown.

A. APPENDIX

A.1 Finite Cosine Transformation of the z-Coordinate

The finite cosine transformation of the z-coordinate is defined as

$$\tilde{T}(u) = \int_0^d T(z) \cos(uz + \phi) dz$$

where u is a positive root of the transcendental equation:

$$u \tan(ud + \phi) = \frac{h_{air}}{k_{th}} = H \quad \text{and} \quad u \tan(\phi) = \frac{h_{air}}{k_{th}} = H_f.$$

The inverse transformation is defined as

$$T(r, z) = \sum_u a_u \cos(uz + \phi).$$

The coefficients a_u are found by performing a cosine transformation of both sides of the equation:

$$\begin{aligned} \tilde{T}(u) &= \int_0^d \sum_u a_u \cos(uz + \phi) \cdot \cos(uz + \phi) \cdot dz \\ &= \sum_u a_u \int_0^d \cos^2 uz (uz + \phi) \cdot dz \\ &= \sum_u a_u \frac{2ud + \sin(2(ud + \phi)) - \sin(2\phi)}{4u} \\ a_u &= \frac{4u \tilde{T}(r, u)}{2ud + \sin(2(ud + \phi)) - \sin(2\phi)}. \end{aligned}$$

And the full definition of the inverse transformation becomes

$$T(r, z) = \sum_u \frac{4u \tilde{T}(r, u) \cos(uz + \phi)}{2ud + \sin(2(ud + \phi)) - \sin(2\phi)}.$$

A.2 Finite Cosine Transformation of $\frac{\partial^2 T}{\partial r^2} + \frac{1}{r} \frac{\partial T}{\partial r} + \frac{\partial^2 T}{\partial z^2}$

$$\int_0^d \left(\frac{1}{r} \frac{\partial}{\partial r} r \frac{\partial T}{\partial r} + \frac{\partial^2 T}{\partial z^2} \right) \cos(uz + \phi) dz = \frac{1}{r} \frac{\partial}{\partial r} r \frac{\partial \tilde{T}}{\partial r} + \int_0^d \frac{\partial^2 T}{\partial z^2} \cos(uz + \phi) dz$$

$$w = \cos(uz + \phi) \quad dv = \frac{\partial^2 T}{\partial z^2}$$

$$dw = -u \sin(uz + \phi) \quad du = \frac{\partial T}{\partial z}$$

$$= \cos(uz + \phi) \frac{\partial T}{\partial z} \Big|_0^d + u \int_0^d \frac{\partial T}{\partial z} \sin(uz + \phi) dz$$

$$w = \sin(uz + \phi) \quad dv = \frac{\partial T}{\partial z}$$

$$dw = u \cos(uz + \phi) \quad v = T$$

$$\begin{aligned} &= \left(\frac{\partial T}{\partial z} \cos(uz + \phi) + uT \sin(uz + \phi) \right) \Big|_0^d - u^2 \int_0^d T \cos(uz + \phi) dz \\ &= \left(\frac{\partial T}{\partial z} \cos(uz + \phi) + uT \sin(uz + \phi) \right) \Big|_0^d - u^2 \tilde{T} \\ &= \cos(ud + \phi) \left(\frac{\partial T(z=d)}{\partial z} + T(z=d)u \sin(ud + \phi) \right) - \cos(\phi) \left(\frac{\partial T(z=0)}{\partial z} + T(z=0)u \sin(\phi) \right) - u^2 \tilde{T} \\ &= -H \cos^2(ud + \phi) + H_f \cos^2(\phi) + \frac{u^2}{H} \sin^2(ud + \phi) - \frac{u^2}{H_f} \sin^2(\phi) - u^2 \tilde{T} \\ &= u \tan(ud + \phi) \cos^2(ud + \phi) - u \tan(\phi) \cos^2 \phi + \frac{u^2 \sin(ud + \phi)}{u \tan(ud + \phi)} + \frac{u^2 \sin(2\phi)}{u \tan(\phi)} \\ &= -u^2 \tilde{T} \end{aligned}$$

Thus, $\int_0^d \frac{\partial^2 T}{\partial z^2} \cos(uz) dz$ transforms to $-u^2 \tilde{T}$.

A.3 Finite Cosine Transformation of $\frac{\alpha}{\kappa_{th}} Q(r) \exp(-\alpha z)$

$$\text{where } Q(r) = P_o \exp\left(-\frac{2r^2}{w^2}\right) \left\{ \Delta R_{NS} + \frac{\Delta R_s}{1 + \frac{F}{F_s} \exp\left(-\frac{2r^2}{w^2}\right)} \right\}$$

The only portion of the right-hand side that is effect by the transformation is the final exponential which is trivial to transformed using integration by parts. The result is:

$$\frac{\alpha P_o}{k_{th}} \frac{1}{\alpha^2 + u^2} \left(u \sin(ud + \phi) \exp(-\alpha d) - \alpha \cos(ud + \phi) \exp(-\alpha d) - \alpha \right) - u \sin(\phi) + \alpha \cos(\phi)$$

A.4 Finite Hankel Transformation of the r-Coordinate

The definition of the finite Hankel Transformation is:

$$\tilde{T}(p) = \int_0^a T(r) J_o(pr) r dr$$

where, p is a positive root of the transcendental equation:

$$-k_{ih} J_1(pa) = h_{air} J_0(pa).$$

The coefficients a_p are found by performing a Hankel transformation of both sides of the equation:

$$T(r, u) = \sum_p a_p J_o(pr)$$

$$a_p = \frac{2}{a^2} \frac{\tilde{T}(pu)}{J_1^2(pa) + J_o^2(pa)}.$$

The complete inverse transformation is defined to be

$$T(r, u) = \frac{2}{a^2} \sum_p \frac{\tilde{T}(p, u) J_o(pr)}{J_q^2(pa) + J_o^2(pa)}.$$

A.5 Finite Cosine Transformation of $\frac{1}{r} \frac{\partial}{\partial r} \left(r \frac{\partial}{\partial r} T(r, u) \right) - u^2 T(r, u)$

$$\int_0^a \frac{1}{r} \frac{\partial}{\partial r} \left(r \frac{\partial T}{\partial r} \right) r J_o(pr) dr - u^2 \int_0^a T(r, u) r J_o(pr) dr = \int_0^a \frac{1}{r} \frac{\partial}{\partial r} \left(r \frac{\partial T}{\partial r} \right) r J_o(pr) dr - u^2 \tilde{T}$$

Substitute $pr \rightarrow \eta$ and therefore, $r \rightarrow \frac{\eta}{p}$ and $dr \rightarrow \frac{1}{p} d\eta$

$$\int_0^{pa} p \frac{\partial}{\partial \eta} \left(\frac{\eta}{p} p \frac{\partial}{\partial \eta} T\left(\frac{\eta}{p}\right) \right) J_o(\eta) \frac{1}{p} d\eta = \int_0^{pa} \frac{\partial}{\partial \eta} \left(\eta \frac{\partial}{\partial \eta} T\left(\frac{\eta}{p}\right) \right) J_o(\eta) d\eta$$

integrate by parts

$$\begin{aligned} u &= J_o(\eta) & dv &= \frac{\partial}{\partial \eta} \left(\eta \frac{\partial T}{\partial \eta} \right) \\ du &= J_o' = -J_1(\eta) & v &= \eta \frac{\partial T}{\partial \eta} \end{aligned}$$

The surface term is 0 leaving:

$$\int_0^{pa} \eta \frac{\partial T}{\partial \eta} J_1(\eta) d\eta$$

integrating by parts once more:

$$\begin{aligned} u &= \eta J_1 & dv &= \frac{\partial T}{\partial \eta} \\ du &= \eta J_o & v &= T \end{aligned}$$

again, the boundary term goes to zero leaving $-p^2 \tilde{T}(p, u)$.

$$\text{Thus, } \frac{1}{r} \frac{\partial}{\partial r} \left(r \frac{\partial}{\partial r} T(r, u) \right) - u^2 T(r, u) = -(u^2 + p^2) \tilde{T}(p, u).$$

A.6 Hankel Transformation of $\beta_g \exp\left(-\frac{\gamma g r^2}{w^2}\right)$

$$\int_0^a r J_o(pr) \exp\left(-\frac{\gamma g r^2}{w^2}\right) dr$$

A switch of variables turns out to be useful. Let $pr \rightarrow \eta$ which implies that

$$r \rightarrow \frac{\eta}{p} \text{ and } dr \rightarrow \frac{1}{p} d\eta.$$

$$\frac{1}{p^2} \int_0^{pa} J_o(\eta) \eta \exp\left(-\frac{\gamma g \eta^2}{w^2 p^2}\right) d\eta$$

Case 1: $\frac{2\gamma g a}{pw} < 1$

$$\begin{aligned} u &= J_o(\eta) & dv &= \eta \exp\left(-\frac{\gamma g \eta^2}{w^2 p^2}\right) \\ du &= J_o' = -J_1(\eta) & v &= -\frac{w^2 p^2}{2\gamma g} \exp\left(-\frac{\gamma g \eta^2}{w^2 p^2}\right) \end{aligned}$$

$$= \frac{1}{p^2} \left[-\frac{w^2 p^2}{2\gamma g} \exp\left(-\frac{\gamma g \eta^2}{w^2 p^2}\right) J_o(\eta) \right]_0^{pa} - \frac{w^2 p^2}{2\gamma g} \int_0^{pa} J_1(\eta) \exp\left(-\frac{\gamma g \eta^2}{w^2 p^2}\right) d\eta$$

$$\begin{aligned} u &= \frac{J_1(\eta)}{\eta} & dv &= \eta \exp\left(-\frac{\gamma g \eta^2}{w^2 p^2}\right) \\ du &= \frac{J_2(\eta)}{\eta} & v &= -\frac{w^2 p^2}{2\gamma g} \exp\left(-\frac{\gamma g \eta^2}{w^2 p^2}\right) \end{aligned}$$

$$= \frac{1}{p^2} \left\{ \left[\frac{w^2 p^2}{\gamma g} \exp\left(-\frac{\gamma g \eta^2}{p^2 w^2}\right) J_o(\eta) \right]_0^{pa} + \frac{w^2 p^2}{\gamma g} \left(\left[\frac{w^2 p^2}{2\gamma g} \exp\left(-\frac{\gamma g \eta^2}{p^2 w^2}\right) \frac{J_1(\eta)}{\eta} \right]_0^{pa} + \frac{w^2 p^2}{\gamma g} \int_0^{pa} \frac{J_2}{\eta^2} \eta \exp\left(-\frac{\gamma g \eta^2}{w^2 p^2}\right) d\eta \right) \right\}$$

Clearly, this results in a series solution. The following limit will be useful in writing the solution:

$$\begin{aligned} \lim_{x \rightarrow 0} \frac{J_1(x)}{x} &= \frac{1}{2} \\ \lim_{x \rightarrow 0} \frac{J_2(x)}{x^2} &= \frac{1}{8} \\ \lim_{x \rightarrow 0} \frac{J_3(x)}{x^3} &= \frac{1}{48} \\ \lim_{x \rightarrow 0} \frac{J_n(x)}{x^n} &= \frac{1}{2^n n!} \\ \lim_{x \rightarrow 0} \frac{x^n}{n!} &= \exp(x) \end{aligned}$$

And the transformation becomes:

$$\begin{aligned} & \frac{1}{p^2} \left[\sum_{m=0}^{\infty} \left(\frac{w^2 p^2}{2\gamma g} \right)^{m+1} (-1)^m \lim_{pa \rightarrow 0} \frac{J_m(pa)}{(pa)^m} + \sum_{m=0}^{\infty} \left(-\frac{w^2 p^2}{2\gamma g} \right)^{m+1} \exp\left(-\frac{\gamma g a^2}{w^2}\right) \frac{J_m(ap)}{(ap)^m} \right] \\ & \frac{1}{p^2} \left[\sum_{m=0}^{\infty} \left(\frac{w^2 p^2}{2\gamma g} \right) \left(\frac{w^2 p^2}{2\gamma g} \right)^m (-1)^m \frac{1}{2^m m!} + \sum_{m=0}^{\infty} \left(-\frac{w^2 p^2}{2\gamma g} \right) \left(-\frac{w^2 p^2}{2\gamma g} \right)^m \exp\left(-\frac{\gamma g a^2}{w^2}\right) \frac{J_m(ap)}{(ap)^m} \right] \\ & \frac{w^2}{2\gamma g} \left[\sum_{m=0}^{\infty} \left(\frac{w^2 p^2}{4\gamma g} \right)^m (-1)^m \frac{1}{m!} + \sum_{m=0}^{\infty} \left(-\frac{w^2 p^2}{2\gamma g} \right)^m \exp\left(-\frac{\gamma g a^2}{w^2}\right) \frac{J_m(ap)}{(ap)^m} \right] \\ & \frac{w^2}{2\gamma g} \left[\sum_{m=0}^{\infty} \left(\frac{-w^2 p^2}{4\gamma g} \right)^m \frac{1}{n!} + \sum_{m=0}^{\infty} \left(-\frac{w^2 p^2}{2\gamma g} \right)^m \exp\left(-\frac{\gamma g a^2}{w^2}\right) \frac{J_m(ap)}{(ap)^m} \right] \end{aligned}$$

And thus, the result for case 1 is:

$$\frac{w^2}{2\gamma g} \left[\exp\left(-\frac{w^2 p^2}{4\gamma g}\right) - \sum_{m=0}^{\infty} \left(-\frac{w^2 p}{2\gamma g a}\right)^m \exp\left(-\frac{\gamma g a^2}{w^2}\right) J_m(ap) \right]$$

Case 2: $\frac{2\gamma g a}{pw} > 1$

$$u = \exp\left(-\frac{\gamma g \eta^2}{w^2 p^2}\right) \quad dv = \eta J_o(\eta)$$

$$du = -\frac{2\gamma g \eta}{p^2 w^2} \exp\left(-\frac{\gamma g \eta^2}{w^2 p^2}\right) \quad v = \eta J_1(\eta)$$

$$= \frac{1}{p^2} \left[-\eta \exp\left(-\frac{\gamma g \eta^2}{w^2 p^2}\right) J_1(\eta) \right]_0^{pa} + \frac{2\gamma g}{w^2 p^2} \int_0^{pa} \eta^2 J_1(\eta) \exp\left(-\frac{\gamma g \eta^2}{w^2 p^2}\right) d\eta$$

$$u = \exp\left(-\frac{\gamma g \eta^2}{w^2 p^2}\right) \quad dv = \eta J_o(\eta)$$

$$du = -\frac{2\gamma g \eta}{p^2 w^2} \exp\left(-\frac{\gamma g \eta^2}{w^2 p^2}\right) \quad v = \eta J_1(\eta)$$

$$= \frac{1}{p^2} \left[-\eta \exp\left(-\frac{\gamma g \eta^2}{w^2 p^2}\right) J_1(\eta) \right]_0^{pa} + \frac{2\gamma g}{w^2 p^2} \left[\eta^2 \exp\left(-\frac{\gamma g \eta^2}{p^2 w^2}\right) J_2(\eta) \right]_0^{pa} + \frac{2\gamma g}{w^2 p^2} \int_0^{pa} \eta^3 J_2(\eta) \exp\left(-\frac{\gamma g \eta^2}{p^2 w^2}\right) d\eta$$

again, a series solution results:

$$\frac{1}{p^2} \sum_{m=0}^{\infty} \left(\frac{2\gamma g}{p^2 w^2} \right)^m (pa)^{m+1} J_{m+1} \exp\left(-\frac{\gamma g a^2}{w^2}\right)$$

$$\left(\frac{p^2 w^2}{2\gamma g}\right) \left(\frac{2\gamma g}{p^2 w^2}\right) \frac{1}{p^2} \sum_{m=0}^{\infty} \left(\frac{2\gamma g}{p^2 w^2}\right)^m (pa)^{m+1} J_{m+1} \exp\left(-\frac{\gamma g a^2}{w^2}\right)$$

$$\frac{w^2}{2\gamma g} \sum_{m=0}^{\infty} \left(\frac{2\gamma g}{p^2 w^2}\right)^{m+1} (pa)^{m+1} J_{m+1} \exp\left(-\frac{\gamma g a^2}{w^2}\right)$$

And thus, the result for case 2 is:

$$\frac{w^2}{2\gamma g} \sum_{m=1}^{\infty} \left(\frac{2\gamma g a}{p w^2}\right)^m J_m(ap) \exp\left(-\frac{\gamma g a^2}{w^2}\right)$$

B. APPENDIX

B.1 Permission to use figures

Permission to reprint figures from dissertation

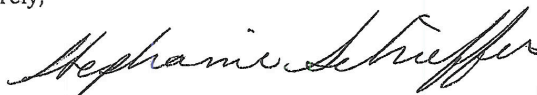
August 11, 2011

Nathan Rimington
20 Point West Blvd
Saint Charles
Mo 63301

I am writing to request permission to use the Figure 4 and Figure 18 from your dissertation *Thermal Lens Shaping for Stigmatic Brewster-Cut Diode-Pumped Solid-State Lasers*, 2004. These figures will appear as originally published. Unless you request otherwise, I will use the conventional style of the Graduate College at the University of Illinois at Chicago as acknowledgement.

A copy of this letter is included for your records. Thank you for your kind consideration of this request.

Sincerely,



Stephanie Schieffer
Physics Department
845 W. Taylor St. M/C 273
Chicago, IL 60607-7059

The above request is approved.

Approved by: Nathan W. Rizk Date: 12 Aug 2011

Gmail - dissertation

8/9/11 5:51 PM



Stephanie Schieffer <stephschief@gmail.com>

dissertation

2 messages

Stephanie Schieffer <stephschief@gmail.com>

Tue, Aug 9, 2011 at 9:43 AM

To: copyright@osa.org

Hello,

I am writing to confirm that the OSA Copyright Transfer Agreement allows me to use figures that I have published in Applied Optics and Optics Express in my dissertation.

thank you for your help,
Stephanie Schieffer

Bembia, Hannah <hbembia@osa.org>

Tue, Aug 9, 2011 at 3:43 PM

To: Stephanie Schieffer <stephschief@gmail.com>

Dear Ms. Schieffer,

Thank you for contacting the Optical Society.

Because you are the author of the source papers you wish to reproduce, OSA considers your requested use of its copyrighted materials to be permissible within the author rights granted in the Copyright Transfer Agreement submitted by the requester on acceptance for publication of his/her manuscript. It is requested that a complete citation of the original material be included in any publication.

This permission assumes that the figures were not reprinted from another source when used in the original papers.

Please let me know if you have any questions.

Sincerely,

Hannah

<https://mail.google.com/mail/?ui=2&ik=0f90a6113a&view=pt&search=inbox&th=131aeffa24554a3b>

Page 1 of 2

Gmail - dissertation

8/9/11 5:51 PM

Hannah Bembia

August 9, 2011

Authorized Agent, The Optical Society

From: Stephanie Schieffer [mailto:stephschief@gmail.com]

Sent: Tuesday, August 09, 2011 10:44 AM

To: Copyright

Subject: dissertation

[Quoted text hidden]

CITED LITERATURE

1. Perry, M., and Stuart, B.: Ultrashort Pulse Laser Machining of Metals and Alloys. U.S. 6,621,040 (Cl. 219/121.67; 219/121.72), Appl. 08/859,020 May 1997; 12 pp, 16 Sept 2003.
2. Engel, E.S., Calhoun, T.R., Read, E.L., Ahn, T.-K., Cheng, Y.-C., Blankenship, R.E., and Fleming, G.R.: Evidence for wavelike energy transfer through quantum coherence in photosynthetic systems, *Nature* 446: 782-786, 2007.
3. Prall, B.S., Parkinson, D.Y., and Fleming, G.R.: Probing correlated spectral motion: Two color photon echo study of Nile blue, *J. Chem. Phys.* 123: 054515(1-3), 2005.
4. Smith, R.J. Light, R.A., Sharples, S.D., Johnston, S.D., Pitter, M.C., and Somekh, M.G.: Multichannel, time-resolved picosecond laser ultrasound imaging and spectroscopy with custom complementary metal-oxide-semiconductor detector, *Rev. Sci. Instrum.* 81: 024901(1-7), 2010.
5. Li, X., Zhang, C.N., Bocora, and Cundiff, S.T.: Many-body interaction in semiconductors probed by optical two-dimensional Fourier transform spectroscopy, *Phys Rev Lett.* 96: 057406/1-4, 2006.
6. Smirl, A.L., Stevens, M.J., Chen, X., and Buccadusca, O.: Heavy-Hole and light-hole oscillations in the coherent emission from quantum wells: Evidence for exciton-exciton correlations, *Phys Rev B* 60: 8267-8275, 1999.
7. Sutherland, R.L., *Handbook of Nonlinear Optics*, 2nd edition, Dekker, New York, 2003.
8. Danielius, R. Piskarskas, A., Stabinis, A., Banfi, G.P., Di Trapani, and Righini, R.: Traveling-wave parametric generation of widely tunable, highly coherent femtosecond light pulses, *J. Opt. Soc. Am. B* 10: 2222-2232 1993.
9. Seifert, F., Petrov, V., and Noack, F.: Sub-100fs optical Ti:Sapphire regenerative amplifier system, *Opt. Lett.* 19: 837-839, 1994.
10. Chung, J. and Siegman, A.E.: Singly resonant continuous-wave mode-locked KTiOPO₄ optical parametric oscillator pumped by a Nd:YAG laser, *J. Opt. Soc. Am. B* 10: 2201-2210, 1993.

11. Khaydarov, J. D. V., Andrews, J. H., and Singer, K. D.: Pulse-compression mechanism in a synchronously pumped optical parametric oscillator, *J. Opt. Soc. Am. B* 12: 2199-2208, 1995.
12. Umbrasas, A., Diels, J.-C., Jacob, J., and Piskarskas, A.: Parametric oscillation and compression in KTP crystals, *Opt. Lett.* 19: 1753-1755, 1994.
13. Rauscher, C., Roth, T., Laenen, R. , and Laubereau, A.: Tunable femtosecond-pulse generation by an optical parametric oscillator in the saturation regime, *Opt. Lett.* 20, 2003-2005, 1995.
14. Lefort, L., Puech, K., Butterworth, S. D., Svirko, Y. P., and Hanna, D.C.: Generation of femtosecond pulses from order-of magnitude pulse compression in a synchronously pumped optical parametric oscillator based on periodically poled lithium niobate, *Opt. Lett.* 24: 28-30, 1999.
15. Kurti, R. S., and Singer, K.D.: Pulse compression in a silver gallium sulfide midinfrared, synchronously pumped optical parametric oscillator, *J. Opt. Soc. Am. B* 22, 2157-2163, 2005.
16. Hönninger, C., Paschotta, R., Morier-Genoud, F., Moser, M., and Keller, U: *Q*-switching stability limits of continuous-wave passive mode locking, *J. Opt. Soc. Am. B* 16 46-56, (1999).
17. Koechner W.: *Solid-State Laser Engineering*, 4th edition, Springer-Verlag, Berlin, 1996.
18. Schieffer, S.L., Brajkovic, D., Cornea, A.I., and Schroeder, W.A.: Low-threshold, dual-passive mode locking of a large mode area Nd:GdVO₄ laser, *Optics Express* 14: 6694-6704, 2006.
19. BATOP optoelectronics, <http://batop.de/>
20. Bowlan, P., and Trebino, R.: Complete single-shot measurement of arbitrary nanosecond laser pulses in time, *Optics Express* 19, 1367-1377 (2011)
21. Trebino, R.: *Frequency Resolved Optical Gating: The Measurement of Ultrashort Laser Pulses*, Kluwer Academic Publishers, Boston, 2002.
22. Kane, D.J., and Trebino, R.: Single-shot measurement of the intensity and phase of an arbitrary ultrashort pulse by using frequency-resolved optical gating, *Opt. Lett.* 18: 823-825, 1993.

23. Trebino, R. and Kane, D.J.: Using phase retrieval to measure the intensity and phase of ultrashort pulses: frequency resolved optical gating, *J. Opt. Soc. Am. A* 10: 1101-1111, 1993.
24. Fuchs, H., Woll, D., Ulm, T., L'Huillier, J.A.: High resolution FROG system for the characterization of ps laser pulses, *Appl. Phys. B* 88: 393-396, 2007.
25. Gil, M.A. , and Simon, J.M.: New plane grating monochromator with off-axis parabolical mirrors, *Appl. Opt.* 22: 152-158, 1969.
26. Innerhofer, E., Südmeyer, T., Brunner, F., Häring, R., Aschwanden, A., Paschotta, R., Hönninger, C., Kumkar, M., and Keller, U.: 60-W average power in 810-fs pulses from a thin-disk Yb:YAG laser, *Opt. Lett.* 28, 367-369, 2003.
27. Burns, D., Hetterich, M., Ferguson, A. I., Bente, E., Dawson, M. D., I. Davis, J., and Bland, S.W.: High-average-power (>20W) Nd:YVO₄ lasers mode locked by strain-compensated saturable Bragg reflectors, *J. Opt. Soc. Am. B* 17: 919-926, 2000.
28. Chen, Y.F., Tsai, S.W., Lan, Y.P., Wang, S.C., and Huang, K.F.: Diode-end-pumped passively mode-locked high-power Nd:YVO₄ laser with a relaxed saturable Bragg reflector, *Opt. Lett.* 26: 199-201, 2001.
29. Spühler, G.J., Südmeyer, T., Paschotta, R., Moser, M., Weingarten, K.J., and Keller, U.: Passively mode-locked high-power Nd:YAG lasers with multiple laser heads, *Appl. Phys. B* 71: 19-25, 2000.
30. He, J.-L., Lee, C.-K., Huang, J.Y.J., Wang, S.-C., Pan, C.-L., and Huang, K.-F.: Diode-pumped passively mode-locked multiwatt Nd:GdVO₄ laser with a saturable Bragg reflector, *Appl. Opt.* 42: 5496-5499, 2003.
31. Berger, J.A., Greco, M.J., and Schroeder, W. A.: High-power femtosecond, thermal-lens-shaped Yb:KGW oscillator, *Optics Express* 16: 8629-8640, 2008.
32. Mollenauer, L.F., and Stohlen., R. H.: Soliton Laser, *Opt. Lett.* 9: 13-15, 1984.
33. Mitschke, F.M. and Mollenauer, L.F.: Ultrashort pulses from the soliton laser, *Opt. Lett.*, 12: 407-409, 1987.

34. Brovelli, L.R., Lanker, M., Keller, U., Goossen, K.W., Walker, and Cunningham, J.A.: An antiresonant Fabry-Perot quantum well modulator to actively mode-lock and synchronize solid state lasers, *Electron. Lett.* 31: 381-382, 1996.
35. Henionm S.R., and Schultz, P.A.: Yb:YAG laser: Mode-locking and high-power operation, in CLEO 1992, p. 540 paper CThQ2
36. Wang, P., Zhou, S. -H., Lee, K.K., and Chen, Y.C.: Picosecond laser pulse generation in a monolithic self-Q-switched solid-state laser, *Opt. Comm.* 114: 439-441, 1995.
37. Keller, U., Weingarten, K.J., Kärtner, F., Kopf, D., Braun, B., Jung, I.D., Fluck, R., Hönninger, C., Matuschek, N., and Aus der Au, J.: Semiconductor Saturable Absorber Mirrors (SESAM's) for Femtosecond to Nanosecond Pulse Generation in Solid-State Lasers, *IEEE J. of Sel. Top. in Quant. Electron.* 2: 435-453, 1996.
38. Ramaswamy-paye, and M., Fujimoto, J.G.: Compact dispersion – compensating geometry for Kerr-lens mode-locked femtosecond lasers, *Opt. Lett.* 19: 1768-1758, 1989.
39. Kopf, D., Spühler, G.J., Weingarten, K.J., and Keller, U.: Mode-locked laser cavities with a single prism for dispersion compensation, *Applied Optics* 35: 912-915, 1996.
40. Kopf, D. Zhang, G., Fluck, R., Moser, and M., Keller, U.: All-in-one dispersion compensating saturable absorber mirror for compact femtosecond laser sources, *Opt. Lett.* 21: 486-488, 1996.
41. Kärtner, F.X. Jung, I.D., and Keller, U.: Soliton Mode-Locking with Saturable Absorbers” *IEEE J. of Sel. Topics in Quant. Electron.* 2: 540-556, 1996.
42. Paschotta, R., and Keller, U.: Passive mode locking with slow saturable absorbers, *Appl. Phys. B* 83: 653-662, 2001.
43. Keller, U., Miller, D.A.B., Boyd, G.D., Chiu, T.H., Ferguson, J.F., and Asom, M.T.: Solid-state low-loss intracavity saturable absorber for Nd:YLF lasers: An antiresonant semiconductor Fabry-Perot saturable absorber, *Opt. Lett.* 17: 505-507, 1992.
44. Keller, U., Chiu, T.H., and Ferguson, J.F.: Self-starting femtosecond mode-locked Nd:glass laser using intracavity saturable absorbers, *Opt. Lett.* 18: 1077-1079, 1993.
45. Keller, U: Ultrafast all-solid-state laser technology, *Appl. Phys. B* 58 347-363, 1994.

46. Brovelli, L.R., Keller, U., and Chiu, T.H.: Design and operation of anti-resonant Fabry-Perot saturable semiconductor absorbers for mode-locked solid-state lasers, *J. Opt. Soc. Amer. B.* 12: 311-322, 1995.
47. Kärtner, F.X., Brovelli, L.R., Kopf, D., Kamp, M., Calasso, I., and Keller, U.: Control of solid-state laser dynamics by semiconductor devices, *Opt. Eng.* 34: 2024-2036, 1995.
48. Silverberg, Y., Smith, P.W., Miller, D.A.B., Tell, B., Gossard, A.C., and Wiegmann, W.: Fast nonlinear optical response from proton-bombarded multiple quantum well structures, *Appl. Phys. Lett.* 46: 701-703, 1985.
49. Gopinath, J.T., Thoen, E.R., Koontz, E.M., Grein, M.E., Kolodziejski, L.A., and Ippen, E.P.: Recovery dynamics in proton-bombarded semiconductor saturable absorber mirrors, *Appl. Phys. Lett.* 78: 3409-3411, 2001.
50. Faubert, D., and Chin S.L.: Subnanosecond pulse generation from a passively mode-locked ruby laser, *Applied Optics* 15: 2347-2348, 1979.
51. Koechner, W.: *Solid-State Laser Engineering*, 4th edition, Springer-Verlag, Berlin, 1996.
52. Siegman A.E.: *Lasers*, University Science Books, Sausalito, CA, 1986.
53. Shen, Y.R.: *The Principles of Nonlinear Optics*, Wiley, New Jersey, 1984.
54. Boyd, R.W.: *Nonlinear optics*, Second edition, Academic press, New York, 2003.
55. Ma, Y., Zhang, Y., Yu, X., Li, X., Chen, F., Yan, R.: Doubly Q-switched GdVO₄/Nd:GdVO₄ laser with AO modulator and Cr⁴⁺:YAG saturable absorber under direct 879nm diode pumping to the emitting level, *Opt. Comm.* 284: 2569-2572 2011.
56. Su, J., Zhang, Q., Yin, S., Guo, C.: Growth and spectral properties of Nd:GdVO₄ laser crystal, *Physica B: Condensed Matter* 403: 3002-3008 2008.
57. Rimington, N.W., Schieffer, S.L., Schroeder, W.A.: Thermal lens shaping in Brewster gain media: A high-power, diode-pumped Nd:GdVO₄ laser, *Opt. Express* 12: 1426-1436, 2004.

58. <http://www.articsilver.com/>
59. Mehendale, M., Nelson T.R., Omenetto, F.G., and Schroeder, W.A.: Thermal eddects in laser pumped Kerr-lens modelocked Ti-sapphire lasers, *Opt. Commun.* 135: 150-159, 1997.
60. Zhang, H., Liu, J., Wang, J., Wang, C., Zhu, L., Shao, Z., Meng, X., Hu, X., Jiang, M., and Chow, Y.T.: Characterization of the laser crystal Nd:GdVO₄, *J. Opt. Soc. Am. B* 19:18-27, 2002.
61. Jensen, T., Ostroumov, V.G., Meyn, J. -P., Huber, G., Zagumennyi, I.A., Shcherbakov: Spectroscopic characterization and laser performance of diode-pumped Nd:GdVO₄, *Appl. Phys. B* 58: 373-379, 1994.
62. Paschotta, R., Aus der Au, J., Spühler, G.J., Morier-Gonoud, F., Hövel, R., Moser, M., Erhard, S., Karszewski, M., Giesen, A., Keller, U.: Diode-pumped passively mode-locked laser with high average power, *Appl. Phys. B* 70: S25-S31, 2000.
63. Koechner, W. : Absorbed Pump Power, Thermal Profile and Stresses in a cw Pumped Nd:YAG Crystal, *Applied Optics* 9: 1429-1434, 1970.
64. Clarkson, W.A. Thermal effects and their mitigation in end-pumped solid-state lasers, *Appl. Phys.* 34: 2381-2395, 2001.
65. Xu, L., Tempea, G., Poppe, A., Lenzer, M., Spielmann, Ch., Krausz, F., Stingl, A., Ferencz, K.: High-power sub-10-fs Ti:sapphire oscillators, *Appl. Phys. B* 65: 151-159, 1997.
66. Fu, Q., Seier, F., Gayen, S.K., Alfano: High-average-power kilohertz-repetition-rate sub-100-fs Ti:sapphire amplifier system, *Opt. Lett.* 22: 712-714, 1997.
67. Rimington, N.: Thermal lens shaping for stigmatic Brewster-cut diode-pumped solid-state lasers, University of Illinois at Chicago, Illinois, 2004.
68. <http://www.as.northropgrumman.com/businessventures/ceolaser/index.html>
69. Yang, J., Liu, J., He, J.: A compact Q-switched and mode-locked diode-pumped Nd:GdVO₄ laser with Cr⁴⁺:YAG, *Laser Physics* 14: 1137-1141, 2005.

70. Zhang, S., Wu, E., Pan, H., Zeng, H.: Passive mode locking in a diode-pumped Nd:GdVO₄ laser with a semiconductor saturable absorber mirror, *IEEE J of Quant Electron* 40: 505-508, 2004.
71. Yan Y., Zhang Z.L., Sha P.F., Cui L., Li R.N., Lin X., Zhang H.J., He J.L., Xin J.G.: A high beam quality laser-diode end-pumped Nd:GdVO₄ slab laser, *Laser Physics* 20: 1284-1287, 2010.
72. Heng-Li Z., Huiai-Jin Z., Dai-Yun L., Ji-Yang W., Peng S., Rüdiger H., Xia-Min J., Keming D.: Diode stack end-pumped Nd:GdVO₄ continuous wave slab laser, *Chinese Physical Lett* 22: 2276-2277, 2005.
73. Cui L., Zhang H., Li J., Raof A., Yang Y., Xu L., Sha P., Fang L., Zhang H., He J., Yin J.: High-power continuous-wave Nd:GdVO₄ slab laser pumped directly into the ⁴F_{3/2} emitting level, *Optics Communications* 284: 341-343, 2011.
74. Stankov, K.A., Tzolov, V.P., and Mirkov, M.G.: Frequency-domain analysis of the mode-locking process in a laser with a second-harmonic nonlinear mirror, *Opt. Lett.* 16: 639-641, 1991.
75. Stankov, K.A., Tzolov, V.P., and Mirkov, M.G.: Frequency-doubling mode locker: the influence of group-velocity mismatch, *Opt. Lett.* 16: 1119-1121, 1991.
76. Chen, Y.F., Tsai, S.W., and Wang, S.C.: High-power diode-pumped nonlinear mirror mode-locked Nd:YVO₄ laser with periodically-poled KTP, *Appl. Phys. B* 72: 395-397, 2001.
77. Kärtner, F.X., Aus der Au, J., Keller, U.: Mode-Locking with Slow and Fast Saturable Absorbers – What's the Difference?, *IEEE J. of Sel. Top. in Quant. Electron.* 4: 159-168, 1998.
78. Schibli, T.R., Thoen, E.R., Kärtner, F.X., and Ippen, E.P.: Suppression of Q-switched mode-locking and break-up into multiple pulses by inverse saturable absorption, *Appl. Phys. B* 70: S41-S49, 2000.
79. Haus, H.A., Fjimoto, J.G., Ippen, E.P.: Analytic Theory of Additive Pulse and Kerr Lens Mode Locking, *IEEE J. of Quant. Electron.* 28: 2086-2096, 1992.

80. DeSalvo, R., Hagan, D.J., Sheik-Bahae, M., Stegeman, G., and VanStryland, E.W.: self-focusing and self-defocusing by cascaded second-order effects in KTP, *Optics Letters* 17: 28-30, 1992.
81. Haus, H.A.: Theory of modelocking with a fast saturable absorber, *J. Appl. Phys.* 46: 3049-3058, 1975.
82. Haus, H.: Mode-Locking of Lasers, *IEEE J. of Sel. Quantum Eletron.* 6: 1173-1185, 2000.
83. Kärtner, F.X., Keller, U.: Stabilization of soliton-like pulses with slow saturable absorbers, *Opt. Lett.*, 20: 16-18, 1995.
84. Jung, I.D., Kärtner, F.X., Brovelli, L.R., Kamp, M., Keller, U.: Experimental verification of soliton modelocking using only a slow saturable absorber, *Opt. Lett* 9: 156-158, 1984.
85. Danailov, M.B., Cerullo, G., Magni, V., Segala, D., and De Silvestri, S.: Nonlinear mirror mode locking of a cw Nd:YLF laser, *Opt. Lett.* 19: 792-794, 1994.
86. Agnesi, A., Guandalini, A., Tomaselli, A., Sani, E., Tnocelli, A., and Tonelli, M.: Diode-pumped passively mode-locked and passively stabilized Nd³⁺:BaY₂F₈ laser, *Opt. Lett.* 29: 1638-1640, 2004.
87. Chekhlov, O. V., and Zaporozhchenko, V. A.: Mapping of the second-harmonic nonlinear mirror characteristics for laser mode-locking and pulse shortening, *J. Opt. Soc. Am. B* 15: 210-215, 1998.
88. Cerullo, G., De Silvestri, S., Monguzzi, A., Segala, D., and Magni, V.: Self-starting mode locking of a cw Nd:YAG laser using cascaded second-order nonlinearities, *Opt. Lett.* 20: 746-748, 1995.
89. Carruthers, T. F., and Duling, I.N.: Passive laser mode locking with an antiresonant nonlinear mirror, *Opt. Lett.* 15: 804-806, 1990.

90. Holmgren, S. J., Pasiskevicius, V., and Laurel, F.: Generation of 2.8ps pulses by mode-locking a Nd:GdVO₄ laser with defocusing cascaded Kerr lensing in periodically poled KTP laser with defocusing cascaded Kerr lensing in periodically poled KTP, *Optics Express* 13: 5270-5278, 2005.
91. R.Wallenstein, U.K. Patent Application GB 2 336 938 A (3/11/1999):A device for the generation of coherent radiation.
92. Qian, L.J., Liu, X., and Wise, F.W.: Femtosecond Kerr-lens mode locking with negative nonlinear phase shifts, *Opt. Lett.* 24, 166-168, 1999.
93. S.H. Cho, S.H., Bouma, B.E., Ippen, E.P., and Fujimoto, J.G.: Low-repetition-rate high-peak-power Kerr-lens mode-locked Ti:Al₂O₃ laser with a multiple-pass cavity, *Opt. Lett.* 24: 417-419, 1999.
94. Weitz, M., Reuter, S., Knappe, R., Wallenstein, R., and Henrich, B.: Passive mode-locked 21 W femtosecond Yb:YAG laser with 124 MHz repetition-rate, *Technical Digest of Conference on Lasers and Electro-Optics* (Optical Society of America, Washington, DC, 2004), paper CTuCC.
95. Dmitriev, V.G., Gurzadyan, G.G., and Nikogosyan, D.N.: *Handbook of Nonlinear Optical Crystals*, Springer Series in Optical Sciences, vol. 64, 3rd edition, Springer-Verlag, New York, 1999.
96. Cerullo, G., Danailov, M.B., De Silvestri, S., Laporta, P., Gegala, D., and Taccheo, S.: A diode-pumped nonlinear mirror mode-locked Nd:YAG laser, *Appl. Phys. Lett.* 65: 2392-2394, 1994.
97. Kato, K.: Temperature-tuned 90° phase-matching properties of LiB₃O₅, *IEEE J. Quantum Electron.* 30: 2950-2952, 1994.

98. Ghotbi, M. and Ebrahim-Zadeh, M.: Optical second harmonic generation properties of BiB_3O_6 , *Opt. Express* 12: 6002-6019, 2004.
99. Van Stryland, E.W., Vanherzeele, H., Woodall, M.A., Soileau, M.J., Smirl, A. L., Guha, S., and Boggess T.F.: Two photon absorption, nonlinear refraction, and optical limiting in semiconductors, *Opt. Eng.* 24: 613-623, 1985.
100. Timoshenko, S. and Goodier, J.N., *Theory of Elasticity*, McGraw-Hill Book Company Inc., New York, 1951.
101. Peng, Y., Cheng, Z., Zhang, T., Qui, J.: Temperature distributions and thermal deformations of mirror substrates in laser resonators, *Applied Optics*, 40: 4824-4830, 2001.
102. Fang, J., Zhang, S.: Modeling for laser-induced surface thermal lens in semiconductors, *Appl. Phys. B* 67: 633-639, 1998.
103. Peng, Y., Cheng, Z., Zhang, Y., Qiu, J.: Laser-induced temperature distributions and thermal deformations in sapphire, silicon, and calcium fluoride substrates at 1.315 μm , *Opt. Eng.* 40: 2822-2829, 2001.
104. Zarem, H.A., Sercel, P.C., Lebens, J.A., Eng, L.E., Yariv, A., Vahala, K.J.: Direct determination of the ambipolar diffusion length in GaAs/AlGaAs heterostructures by cathode luminescence, *Applied Phys. Lett.* 55: 1647-1649, 1989.
105. Dvorak, M.D., Schroeder, W.A., Andersen, D.R., Smirl, A.L., and Wherrett, B.S.: Measurement of the anisotropy of two-photon absorption coefficients in zincblende semiconductors, *IEEE Journal of Quantum Electronics* QE-30: 256-268, 1994.
106. Chénais, S., Forget, S., Druon, F., Balembois, F., Georges P.: Direct and absolute temperature mapping and heat transfer measurements in diode-end-pumped Yb:YAG, *Appl. Phys. B* 79: 221-224, 2004.
107. <http://engineeringtoolbox.com/>
108. Capinski, W.S., Maris, H.J., Ruf, T., Cardona, M., Ploog, K., and Katzer, D.S.: Thermal-conductivity measurements of GaAs/AlAs superlattices using a picosecond pump-and-probe technique, *Physical Review B* 59: 8105-8113, 1999.

109. Yu, X.Y., Chen, G., Verma, A., Smith, J.S.: Temperature dependence of thermophysical properties of GaAs/AlAs periodic structure, *Applied Physics Letters* 67: 3554-3556, 1995.
110. Volodchenko, K.V., Hurdoglyan M.S., Kim, C., and Kim, G.U.: Observation and investigation of off-axis modes in a high-power Nd:YAG laser, *Applied Optics* 43: 4768-4773, 2004.
111. A.E. Siegman: Analysis of laser beam quality degradation cause by quartic phase aberrations, *Applied Optics* 32: 5893-5901, 1993.
112. Makki, S. and Leger, J.: Solid-State Laser Resonators with Diffractive Optic Thermal Aberration Correction, *IEEE Journal of Quantum Electronics* 35: 1075-1085, 1999.
113. Sadao, A.: GaAs, AlAs, and $\text{Al}_x\text{Ga}_{1-x}\text{As}$: Material parameters for use in research and device applications, *J. Appl. Phys.* 58: R1-R29, 1985.
114. Davidsen, A.F., Hartwig, G., Fastie, W.G.: Ultraviolet spectrum of Quasi-stellar object 3C273, *Nature* 26: 203-206, 1977.
115. DeLong, K. W., Trebino, R., and Kane, D.J.: Comparison of ultrashort-pulse frequency-resolved-optical-gating traces for three common beam geometries, *J. Opt. Soc. Am. B* 11: 1595-1608, 1994.
116. Model 1 CX 406 AQ, 3.125 μm pixel size, 3.98Mpixel (2312x1720) CCD from Sony,
www.sony.net/Products/SCHP/cx_news/vol16/pdf/icx238.pdf.
117. 2.25 μm pixel pitch, 4Mpixel CMOS CCD from Matsushita Electric Industrial Co, Ltd (Panasonic),
http://neasia.nikkeibp.com/nea/200402/conele_288148.html.
118. Morrissey, Q.R., Waltham, N.R., Turchetta, R., French, M.J., Bagnall, D.M., and Al-Hashimi B.M.: Design of a 3 μm pixel linear CMOS sensor for earth observation, *Nucl. Inst. & Meth. Phys. Res. A* 512: 350-357, 2003.
119. Czerny, M. and Turner, A.F.: Über den Astigmatismus bei Spiegelspektrometern, *Z. Phys.* 61: 792 (1930).
120. Gill, M., Simon, J.M. , and Fantino, A.N.: Czerny-Turner spectrograph with a wide spectral range, *Appl. Opt.* 27: 4069-4072 (1988).

121. Ebert, H.: Zwei formen von Spectrographen, *Wiedemann's Annalen* 38: 489, 1889.
122. Fastie, W.G.: Small plane grating monochromator, *J. Opt. Soc. Am.* 42: 641-647, 1952.
123. Fastie, W.G.: Image forming properties of the Ebert spectrometer, *J. Opt. Soc. Am.* 42: 647-651, 1952.
124. Fastie, W.G.: Ebert spectrometer reflections, *Physics Today*, January: 37-43, 1991.
125. Gil, M.A. and Simon, J.M.: Aberrations in plane grating spectrometers, *Optica Acta* 30: 777-806, 1983.
126. Simon, J.M., Gil, M.A., and Fantino, A.N.: Use of plate diagram method in the evaluation of monochromators and spectrographs, *Appl. Opt.* 27: 4062-4068, 1988.
127. Hill, R.A.: A new plane grating monochromator with off-axis paraboloids and curved slits, *Appl. Opt.* 8: 575-581, 1969.
128. Chupp, V.L. and Grantz, P.C.: Coma canceling monochromator with no slit mismatch, *Appl. Opt.* 8: 925-925, 1969.
129. E. Hecht, *Optics*, Addison Wesley, San Francisco, 2002.
130. Gil, M.A. and Simon, J.M.: New plane grating monochromator with off-axis parabolical mirrors, *Appl. Opt.* 22: 152-158, 1983.
131. Simon, J.M., and Gil, M.A.: Distortion and split-image curvature calculated by the plate diagram analysis in monochromators with off-axis mirrors, *Optica Acta* 25: 381-394, 1978.
132. Gill, M.A. and Simon, J.M.: Calculation of field curvature by the plate method for off-axis systems, *Optica Acta* 30: 65-71, 1983.
133. Gil, M.A., and Simon, J.M.: Aberrations in off-axis spectrometers, *Optica Acta* 30: 1287-1301, 1983.
134. [<http://www.quadibloc.com/science/opt0505.htm>, wikipedia]

- 135. Grischkowsky, G., and Balant, A.C.: Optical pulse compression based on enhanced frequency chirping, *Appl. Phys. Lett.* 41: 1-3, 1982.
- 136. Eggleton, B.J., Lenz, G., Slusher, R.E., Litchinitser, N.M.: Compression of optical pulses spectrally broadened by self-phase modulation with a fiber Bragg grating in transmission, *Applied Optics* 37: 7055-7061, 1998.
- 137. Treacy, E.B.: Optical pulse compression with diffraction gratings, *IEEE J. of Quantum Electron.* QE-5: 454-458, 1969.
- 138. Schieffer, S.L. Rimington, N.W., Nayyar, V.P., and Schroeder, W.A.: High-resolution, flat-field, plane-grating, *f*/10 spectrograph with off-axis parabolic mirrors, *Applied Optics* 46: 3095-3101, 2007.

Name: **Stephanie Schieffer**

Education:

University of Illinois at Chicago
PhD. in Physics August 2011
M.S. in Physics, 2008
B.S. in Physics, 2004, Departmental Honors

University of Redlands, CA
B.A. Environmental Studies and German, 1994

Publications:

S.L. Schieffer, J.A. Berger, B.L. Rickman, V.P. Nayyar, W. A. Schroeder, “Thermal effects in saturable Bragg reflectors”, in submission JOSA B.

S.L. Schieffer, N.W. Rimington, V.P. Nayyar, W. A. Schroeder, “High-resolution, flat-field, plane-grating, $f/10$ spectrograph with off-axis parabolic mirrors”, Applied Optics, **46**, 3095-3101 (2007).

S.L. Schieffer, D. Brajkovic, A.I. Cornea, W.A. Schroeder, “Low-threshold, dual-passive mode locking of a large mode area Nd:GdVO₄ laser”, Optics Express. **14**, 6694-6704 (2006).

N.W. Rimington, S.L. Schieffer, W.A. Schroeder, B.K. Brickeen, “Thermal lens shaping in Brewster gain media: A high-power, diode pumped Nd:GdVO₄ laser”, Optics Express. **12**, 1426-1436 (2004).

S.L. Schieffer, D. Brajkovic, A.I. Cornea, W.A. Schroeder, “Dual-passive mode-locking of a high-power, TEM₀₀-mode, thermal-lens-shaped Nd:GdVO₄ laser”, Trends in Optics and Photonics (TOPS). Manuscript ID: 60647 (2005).

Presentations:

Air Force Research Lab, Kirtland Air Force Base,
Albuquerque, NM June 2011
“A high-power, TEM₀₀-mode, CW mode locked, ~10ps Nd:GdVO₄ laser oscillator”

JILA NIST-CU, Boulder, August, 2010
 “Building a mode locked laser”.

Conference on Lasers and Electro-Optics (CLEO),
 Baltimore, May, 2005
S. L. Schieffer, D. Brajkovic, A. I. Cornea, W. Andreas Schroeder
 “Dual-passive mode-locking of a high-power, TEM₀₀-mode,
 Nd:GdVO₄ laser”
 Paper No. CnTI7.

Advanced Solid State Photonics (ASSP), Vienna Austria,
 February 2005
S. L. Schieffer, D. Brajkovic, A. I. Cornea, W. Andreas Schroeder.
 “Stable Dual-Passive Mode-Locking of a 7W, Thermal-Lens-
 Shaped Nd:GdVO₄ Laser” Presentation no. WB8.

Conference on Lasers and Electro-Optics (CLEO), San
 Francisco, May, 2004
 N.W. Rimington, S.L. Schieffer, W.A. Schroeder, B.K. Brickeen.
 “A high-power, TEM₀₀-mode, diode-pumped, Brewster-cut
 Nd:GdVO₄ laser”
 Paper No. CThJJ1.

Awards & Activities:

**Graduate Assistance in Areas of National Need
 (GAANN) Fellowship**, 2009-2011
 Tuition, stipend, travel expenses for conferences, and a computer.

Outstanding TA, Spring 2007
 Cash award for outstanding TAs as evaluated by students.

James S. Kouvel Fellowship, 2007-2008
 Annual cash award for a student in excellent academic standing in
 the physics department and who has passed the preliminary exam.

Girl Scouts of America, 2004-2006
 Assisted Women in Optical Society of America (WOSA) in the
 development and writing of an optics badge.

European Union Grant, February 2005
 US – Vienna round trip plane ticket, 4 days room and board,
 conference, and short course fees.

Motorola Women in Science and Engineering Travel**Grant**, April, 2005

Partial support for travel to the Conference on Lasers and Electro-Optics (CLEO), Baltimore, May, 2005.

Society of Physics Students (SPS), President, 2003-2004**Sivananthan Undergraduate Research Fellowship**, May

2003

Inter-departmental fellowship for summer research project.

Citizenship:

USA